Quantitative Laboratory Modelling of Host Rock Deformation due to the Intrusion of Magma

Frank Guldstrand

THESIS

for the degree of

Philosophiae Doctor

Faculty of Mathematics and Natural Sciences

University of Oslo

September 2018

Author:
Frank Bo Buster Guldstrand
f.b.b.guldstrand@geo.uio.no

Supervisors:
Main Supervisor: Dr Olivier Galland, Senior Researcher, Physics of Geological Processes, NJORD
Secondary Supervisor: Dr Alban Souche, Post-doctoral Researcher, Physics of Geological Processes, NJORD

Series of dissertations submitted to the
Faculty of Mathematics and Natural Sciences, University of Oslo
No. 2017

ISSN 1501-7710

Cover: Hanne Baadsgaard Utigard.
Print production: Reprosentralen, University of Oslo.

PREFACE AND ACKNOWLEDGEMENTS

I first came to PGP in 2013. Fanny, *min kjæreste* as Norwegians say, had been hired as a research assistant over the summer through her supervisor at Uppsala University, and they needed a second person for the job. So I tagged along. We were excited to work in the Physics of Geological Processes (PGP) lab and it was a fantastically warm summer, just as it is now, when I am writing my PhD Thesis. Meeting Olivier and experiencing the cross-disciplinary approach by PGP inspired me to change several of the courses in my MSc curriculum. Two years later I presented my MSc thesis, partly on data we produced during our stay in Oslo. So in the summer of 2015 I applied for a PhD with the PGP-group and Olivier Galland. During my time at PGP many things have changed and PGP is now part of the NJORD centre, a cross-disciplinary research centre directly under the Faculty of Mathematics and Natural Science. I've had my ups and downs during the 3 years of my PhD. Inspiring field trips to the magmatic complexes of the basin in Neuquén, Argentina to understand what my research was about. Crazy conferences in Copenhagen, Portland and Montpellier (well, a bit outside Montpellier) full of interesting discussion and criticism. And many, many days in the lab in Oslo and also Le Mans, where I had a 3 months research stay. This chapter of my life is approaching its end and I would like to thank some of the people who helped me along the way.

Olivier, I would like to thank you for introducing me to this environment and all the help along the way. Our countless discussions have usually left me exhausted immediately afterwards but full of energy and motivation after a nights sleep. The time you have dedicated to me and your other PhD students is inspiring.

Alban, you always have time for scientific discussions at great depth and your eye for detail is impressive. I have greatly appreciated your input and support. Now at the end of this PhD, you have not only helped teach me how to do science but also how to brew beer.

The volcano group within PGP have been invaluable. Firstly, I firmly believe that some of the best scientific work comes through people working together on a project. In this sense, the volcano group have been very supportive and encouraging. However, our group have also been my largest critics and have pushed me to produce good work and to hone my arguments. I want to say thanks to Tobias, Håvard, Øystein, Ben and Ole your company at work and outside has made all the difference.

PGP, PoreLab (both now part of NJORD) and CCSE are all on the fourth floor in the west wing of the physics building. Our large lunch group is not always easy to gather but it is a great environment to work in. I have been happy to be part of such an inclusive and caring group.

I want to thank my family for all of their support. My Mom, Dad and Sister have always listened and helped me. Dad, you put in a lot of work when we moved here, thank you for that. Mom, your experience in the academic world helped me a lot.

Fanny, without you I probably would never have dared to move to Oslo and pursue a PhD. You support me when I doubt my abilities and give me the kick I need when I am being lazy or scared. We are a team and it means so much to me. I love you!

Finally, I want to thank the Norwegian Research Council for funding my PhD through a FRINATEK grant and promoting free research. The result of more than 3 years of work will be presented in this thesis. It is written in an attempt to make it accessible such that, hopefully, novice geoscientists will understand. I sincerely hope the reader will enjoy reading this thesis and get some sense of wonder for the problem of how magma ascends through the Earth's crust and erupts.

……

Frank Guldstrand

Oslo June 2018

SUMMARY

Volcanic eruptions are the result of magma having intruded, ascended toward the surface and finally breached the surface. Geoscientists have long been discussing the nature of magmatic intrusions and their emplacement mechanisms. Observing the subsurface intrusion process remains inaccessible, but in exhumed and extinct volcanic plumbing systems it is possible to observe snapshots of the intrusion geometries and their emplacement mechanism. These field studies show that a large part of the subsurface system of magma intrusions comprise sheet intrusions in various configurations. The vertical ascent of magma is commonly attributed to sub-vertical dykes, i.e. intrusions of sheet geometry.

Detailed field observations show that the propagation of sheet intrusions can be accommodated by various failure mechanisms and small-scale deformations around the intrusion tip. These range from sharp tipped intrusions that appear to fail in a tensile mode to blunt-tipped intrusions where the host rock deforms by substantial plastic deformation and shear failure ahead of the intrusion. Yet common models of sheet intrusion propagation, such as the linear elastic tensile fracture, only account for the first emplacement mechanism and rarely consider the second. This second mode of emplacement implies a forceful intrusion of the magma that deforms the host by pushing the rock ahead of it, and has been referred to as a viscous indenter type model. This mechanism, relating to ***how the host rock deforms, in small scale, to accommodate intruding magma,*** remains poorly studied and is the first motivation of my thesis.

The movement of magma in the subsurface causes the Earth's surface to deform. This large-scale deformation can be studied through the use of geodetic monitoring techniques and has revealed characteristic patterns of magma-induced surface deformation. The surface deformation is commonly fitted with static elastic models, the physical assumptions of which remain to be validated. ***How large-scale surface deformation reflects the subsurface processes*** have yet to be properly studied, and is the second motivation of this thesis.

My thesis explores the forceful intrusion of viscous magma in the shallow crust through the use of quantitative laboratory modelling. I present the application of the open-source photogrammetric software suite MicMac in studying large and small-scale deformation in laboratory models. I proceed to explore the nature of magma emplacement in the case of viscous magma intruding into a fine-grained Mohr-Coulomb cohesive host representative of the shallow crust. This model of large-scale deformation shows, amongst other, that vertical sheet intrusions, under these conditions, exhibit uplift that is not

predicted by established geodetic models. Furthermore, I identify characteristic dynamic patterns of surface deformation associated with cone sheets and dykes. The nature of these patterns also reveals that it is possible to forecast the eruption location through a purely geometrical relationship without having to invoke mechanical modelling of the subsurface intrusion. Finally, I study the small-scale surface deformation associated with intrusions into model crusts of varying cohesion. These final experiments show how the model crust is a controlling parameter on the emplacement mechanics resulting in finger intrusions for weak crusts to vertical sheet intrusions for stronger crusts.

In conclusion, the work done for this thesis lays the groundwork for a discussion on ***under which conditions a propagating fracture filled with a viscous magma can best be described by a Linear Elastic Fracture Mechanic model or a Viscous Indenter model?*** The work uses simplified models to show the need to account for the geological scenario when assessing magma intrusion and the associated deformation.

TABLE OF CONTENTS

1. INTRODUCTION AND AIM

The cone-shaped surficial expression constructed by successive eruptions of magma having risen through the Earth's crust is what comes to mind when mentioning volcanoes. However, the nature of the volcano is not limited to its surface expression but is also linked to, and controlled by, conduits and storages of magma at various levels within the crust. The occurrence of volcanism and the associated magmatic activity is a fundamental process in the generation of new crust on Earth. When magma does breach the surface, the impacts of large volcanic events have the potential to cause significant effects on civilizations (e.g. Grattan, 2006), climate (e.g. Briffa et al., 1998) and life on Earth (e.g. Kamo et al., 2003). However, volcanism can also contribute with beneficial effects, such as geothermal energy and fertile volcanic soils (De la Cruz-Reyna and Siebe, 1997). The intrusion and emplacement of magma is also of interest for natural resources. The magma itself may crystallize to form an ore deposit or act as the main agent in an enrichment process of the surrounding crust (e.g. Li et al., 2005). Magma intruding into organic-rich hosts may favour the formation of hydrocarbons, and in some cases magmatic intrusions themselves act as the reservoirs (e.g. Farrimond et al., 1996). There is a growing interest for the system of conduits and reservoirs beneath the Volcanoes often referred to as the Volcanic Plumbing System (VPS) (Tibaldi, 2014). Naturally, the hazardous aspect of volcanoes promotes the study and understanding of the VPS to mitigate hazards, forecast and possibly predict volcanic eruptions.

There are many processes acting within the VPS including chemical, thermal and mechanical interactions between magma and the crust that hosts it. Regarding propagation and emplacement, the majority of models comprise mechanical models. These models currently account for mainly elastic deformation and tensile opening or completely cohesionless shear failure (Schmiedel et al., 2017a). Observations from exhumed extinct VPS show that intrusions exhibit deformation supporting both models. However, the intrusion geometries and their associated models do not always match. In fact, dykes in nature, commonly explained by an elastic and tensile model, display substantial plastic deformation and shear failure of the surrounding host rock closely associated to the intrusion and the tip. Therefore the first aim of this work was to explore (1) *how the host rock deforms, in small scale, to accommodate intruding magma.*

Magmatic activity also induces far-field large-scale deformation in volcanically active regions in nature, which can be monitored and measured. This surface deformation can be analyzed using simplified elastic models according to which fits the observed deformation the best. As observed from

exhumed volcanic systems in nature, the inner deformation of the system show that the elastic models only comprise one end-member of the intrusion process. Furthermore, since these fitting models are static they do not account for the dynamic nature of the process. It is currently not possible to validate whether these models accurately represent what is happening in the subsurface even though they may produce a good fit to the observed data. The second objective of the work performed during this thesis will attempt to address *(2) how large-scale surface deformation reflects the subsurface processes.*

In its entirety, this thesis will attempt to demonstrate these statements and address this discrepancy of our current models of intrusion emplacement and the observations of exhumed intrusions as well as provide dynamic laboratory models of intrusions and their associated surface deformation. It will provide the basis for a discussion to address the third and final objective of this thesis describing *(3) under which conditions a propagating fracture filled with a viscous fluid can best be described by a Linear Elastic Fracture Mechanic model or a Viscous Indenter Model and If both models apply how the transition between the two could appear?*

To address the first aim, it is important to consider deformation of the host associated with the intrusion tip. This will be tackled through using a 2D experimental setup where the propagating crack tip is clearly visible and where the deformation can be monitored. The second aim addresses the large-scale deformation induced by magmatic intrusions, particularly if the emplacement mechanism differs from that of common models. This is addressed using a 3D-experimental setup to quantify and characterize the surface deformation of mainly vertical sheet intrusions, i.e. dykes, and cone sheets. Integrating the results from the 2D and 3D experimental results will allow for a larger understanding of the models of propagation and lead to a discussion on the validity of various models in different geologic settings.

2. THE VOLCANIC PLUMBING SYSTEM

The VPS is the system of magma conduits and reservoirs leading from the source of magma to the surface where it erupts. These conduits and chambers form a network of connected intrusions of varying geometries (Fig. 1). Very generally speaking the VPS allows for magma to flow and stall at various depths in the upper brittle crust. The stalling may lead to the formation of long-lived reservoirs of magma, in which pressure may build up, eventually leading to the initiation of a new intrusion or eruption. The VPS is a complex system and its dynamics will depend on the viscosity and pressure coupled with the mechanical feedback of the host rock in which it is emplaced (Galland et al., 2018b). VPS dynamics are likely more complex than the sum of its parts, but understanding the possible emplacement of its individual parts may still convey understanding to the greater picture. To do this, a brief review of the intrusion geometries that can be observed associated with the plumbing systems of volcanoes will be presented. The volcanological terminology is extensive and can at times be confusing as the names can infer geometries, emplacement mechanics and genesis. As such, I will attempt to use simplified general terminology to describe intrusion geometries in such a way that a novice student of magmatic intrusions may understand. However, I will not cover the collapse of magma chambers and the formation of caldera as the aim of this thesis is to study intrusion of magma.

The accessibility of the VPS is highly limited and direct observations are not achievable, instead it has been studied through extinct and exhumed systems or through indirect geophysical methods, such as seismic surveys or tomography (e.g. Almendros et al., 2002, Chiarabba et al., 2004).

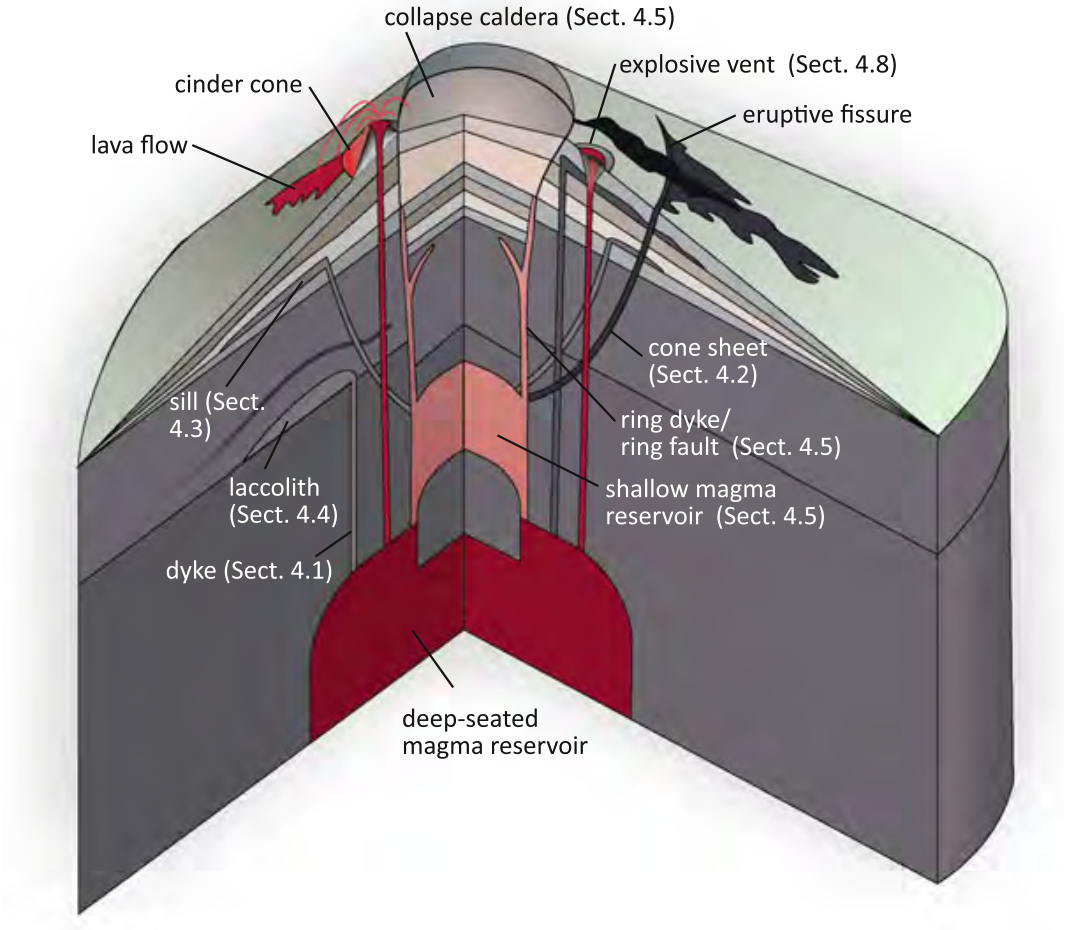

Figure 1. Simplified schematic of the Volcanic Plumbing System and the intrusions found within it (figure used with permission from Galland et al., 2018b).

At its core, a volcanic plumbing system revolves around an accumulation of magma forming a magma chamber containing totally or partially molten magma. These may be quasi-spherical or ellipsoidal (e.g. Burchardt et al., 2013). Such reservoirs are thought to be able to exist at many levels in the shallow crust. At Mt St Helens, for example, the main magma chambers has been proposed to reside just below 6 km depth (Wiemer and McNutt, 1997). Such reservoirs of magma are expected to act as sources to many different geometries of magmatic intrusion. There may be cylindrical vertical conduits of magma such as cryptodomes (e.g. Okada et al., 1981, Keating et al., 2008). However, it seems a great many components of the volcanic plumbing system are consisting of sheets in various configurations. Here we will address the major intrusion types found in the VPS:

- Common intrusions thought to facilitate vertical ascent of magma are dykes, vertical to sub-vertical planar sheet intrusions (Tibaldi et al., 2013). These may occur in "swarms", i.e. there are many dykes localized to a certain location (e.g. Callot et al., 2001). Dykes are commonly thought to "feed", or act as source for other intrusions to grow (Galindo and Gudmundsson, 2012).

- Horizontal sheet intrusions, in the shallow brittle crust, appear to emplace along mechanical weakness such as layering found in sedimentary basins and facilitate lateral spreading of magma (e.g. Svensen et al., 2012). Sills may exhibit features such as flat sections, concordant with the host layering, and ramps, which cross-cut the layering, or bridges of host rock in the sill (Eide et al., 2017). A curious version of sills are the so-called *saucer shaped sills*, which have a circular central flat region bounded by a ramping section of inwardly dipping inclined sheets. In general, these intrusions have the shape of a saucer (Polteau et al., 2008, Schmiedel et al., 2017b).

- Two sheet intrusion types remain to be addressed. The first of these are cone sheets, similar in a way to saucer shaped sill but without a central flat region, instead formed like a cone (Burchardt et al., 2013, Tibaldi et al., 2013). The second and final of the sheet intrusion are ring dykes, vertical sheet intrusion in the shape of a cylinder (Chevallier and Woodford, 1999, Kennedy and Stix, 2007). Such ring dykes have been attributed to being created through weaknesses in the crust related to magma chamber collapse structures that allow for pathways for the magma to subsequently intrude.

- Leaving the sheet intrusions, we now address the intrusions that develop into more massive types of intrusion, such as plugs, which can be related to the previously mentioned conduit-shaped intrusions but also so-called laccoliths, which are tabular intrusion uplifting their overburden. Classically laccoliths are considered to uplift their overburden through smooth elastic bending, however, field observations show that many aspect ratios are too high for this to be valid. Thus, alternative models have been proposed called punched laccoliths that uplift the overburden through shear failure. Field observations show that laccolith emplacement can occur through both described mechanisms (e.g. Mattsson et al., 2018).

- In the case of very high viscosity magmas, so called *cryptodomes* can form, i.e. large-scale finger structures. These propagate by dominantly pushing their overburden upward and can erupt at the surface (e.g. Major et al., 2009). Okada et al. (1981) showed that the 1977-1978 eruptions of the volcano Usu displayed doming, i.e. vertical uplift, and a ring-shaped pattern of locations for the spatial distribution of seismicity.

All intrusion geometries considered, it seems that sheet intrusions in one way or another is a primary emplacement geometry found in volcanic plumbing system. To understand the emplacement of individual parts we need to address several factors. The influx of new magma, differentiation of magma, crystallization and assimilation of host rock implies that large ranges of magma viscosities are possible. Moreover, it is expected that the effect of temperature and how it influences deformation, pore pressure and supercritical fluids will also influence emplacement. However, a significant control on the deformation refers to host

rock properties such as cohesion. Ultimately, the host rock needs to accommodate space for magma to intrude it, which will naturally vary if it is very competent, such as crystalline bedrock or weaker such as rocks in sedimentary basins. The way the host rock deforms will control the dynamics of emplacement and feedbacks mechanically into the intrusion propagation. To further study this, we will review host rock deformation observed in both small scale (tip/outcrop) and large scale (mainly surface deformation).

3. Observations of Deformation accomodating Intrusions

The basis for creating a model must be based on, and benchmarked against, observations associated with the process it is intended to model. In this chapter, we will review observations of deformation and emplacement of intrusions firstly in the near-field surrounding of intrusions referred to as the small-scale, and secondly in the far-field large-scale surface deformation.

3.1 Small-Scale Deformation

Intrusion emplacement may induce both near-field and far-field deformation. In addressing small-scale deformation, we may consider both the surrounding of the intrusion, i.e. internal host intrusion-scale deformation, and the immediate surrounding of the tip, i.e. tip-scale host deformation (Fig. 2). Deformation may be governed by properties such as the strain rate and traction along the interface that may vary depending on host properties and the scale considered. Ultimately, the rheology of the host rock plays a governing role in how the intruding magma is accommodated. Many models assume a reversible elastic rheology, where stress and strain maintain a linear relationship, implying that once the stress is released the rock would retain its original shape. Rocks may also deform through viscous ductile flow, a form of irreversible plastic deformation. However, this occurs over certain conditions such as when subjected to low strain rate for a long time and/or higher pressure and temperature conditions in the deeper crust. This thesis deals with the intrusion of magma in the upper shallow crust where the rock deforms in a brittle manner. This is usually characterized by a Mohr-Coulomb linear failure criterion. For cohesionless material such as sand, the shear stress at failure is directly proportional to the normal stress and tangent of the angle of internal friction. Rocks, however, are cohesive and can sustain stress without failing. The intercept of the failure envelope with the y-axis characterizes this property (Jaeger et al., 2009). Magma on the other hand is molten fluid rock with a composition-dependent viscosity, i.e. the fluid retains a resistance to flow. This means that a magma with a higher silica content will have a higher viscosity and magma viscosity can span several orders of magnitude (Bottinga and Weill, 1972, Scaillet et al., 1997). Moreover the viscous flow in narrow slits or pipes may also induce even larger viscous stresses, which have to be overcome for flow to occur and so result in a larger pressure build-up. This is ultimately one of the reasons for the explosive nature of some volcanoes.

Intrusion-scale and tip-scale are two identifiable zones where the aforementioned processes can be highly variable. The intrusion tip has previously been identified to be particularly interesting, especially considering sheet intrusions (Rubin, 1993, Rubin, 1995).

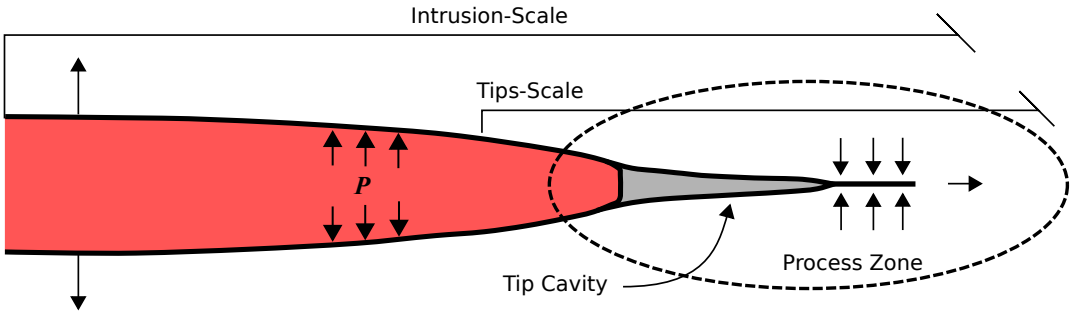

Figure 2. Schematic of intrusion and tip scales of a magmatic intrusion with tip cavity present.

Obtaining observations of the intrusion process is difficult. Although, volcanic processes, or at least shallow intrusions and eruptions, occur within timespans comprehensible to humans, we still face many challenges. Observations of surface fractures occurring before eruption for example are very dangerous to observe and many physical processes are hard to distinguish such as free surface effects (Fig. 3.). The subsurface nature of the process does not allow direct observations of the active process at depth. As such we must base our observations on indirect methods interpreted to be associated with the intrusion tip or near field deformations along the intrusion wall, such as seismicity (e.g. Ágústsdóttir et al., 2016). In other cases we have to rely on observations on outcrop scale. However, outcrops limit our observations to instantaneous snapshots of the intrusion processes restricted to the particular part of outcropping intrusion. This means we rarely get the full image at any given time. Nevertheless, field observations provide important observations to which we can compare models and hopefully improve our understanding.

The nature of an intrusion at tip-scale may be simplified into two end-members, a 3D geometry as in the end of a finger type intrusion, or a 2D geometry as the end of sheet geometry (e.g. Pollard et al., 1975, Rubin, 1993). Their orientation in space, i.e. vertical or horizontal, may here be considered a secondary feature attributed to many things such as for example emplacing along weaknesses, neutral buoyancy level, regional or local stress fields or stress reorientations (e.g. Taisne and Jaupart, 2009, Menand et al., 2010, Hansen et al., 2011). There are many parameters that may influence the nature of intrusion emplacement and propagation concerning the physical properties of the intruding magma and host rock. Here, we will consider the nature of the emplacement as documented by field observations or by seismicity monitored during intrusions of magma proposed to be associated with the intrusion tip.

Figure 3. Surface fractures caused by the underlying intrusion of magma into the lower East Rift Zone on Hawaii associated with eruption of Kilauea 2018 currently on-going during the writing of this thesis (photos available under the public domain from the U.S. Geological Survey).

Sheet intrusions, particularly sub-vertical dykes, are generally considered to open in a tensile mode. Effectively splitting the host in two as it propagates resulting in host displacement perpendicular to the orientation of the main sheet. Such sharp tips are observed (Rubin, 1993). Dyke tips may exhibit a tip cavity where magma fails to fill the fracture and forcing the fracture to open in a tensile mode, the nature of such tip cavity remain discussed. However, even though tips may be sharp, curving of the dyke may reveal inelastic deformation is occurring (Rubin, 1995). Other observations from Iceland show rounded tips that are attributed the intrusion occurring in a weaker, or softer, host rock. There are also very blunt, rectangular, tips attributed to the dyke interacting with harder layer as it ascends (Gudmundsson, 2002). Structural studies also show reverse faulting activated by dyking indicating that displacement, with respect to the vertical dyke may not always be primarily horizontal (Gudmundsson et al., 2008).

The tips of horizontal sheet intrusions can also exhibit sharp thin tips primarily opening the host rock (Hansen et al., 2011, Eide et al., 2017). However, Pollard et al. (1975) observed that the peripheral part of sheet intrusion into a sandstone-shale formation (relatively weak rock) transitioned into fingers. These fingers displayed blunt rounded tips with host rock being bent, folded and squeezed ahead of the intrusion tip. Furthermore, vertical sheet intrusion of felsic composition (high viscosity) also showed the development of small fingers

along offsets in the main intrusion but the longevity of such structures is unknown. The intrusion-scale contact in this observation also exhibited a sinusoidal wavy nature of the margin. Further observations of similar geological scenarios where higher viscosity intrusion have intruded geologically weak rocks show outcrops of fingers displaying very localized deformation ahead of the main sheet geometry (Schofield et al., 2012). However, also ahead of intrusions of dominant sheet intrusion geometry we see substantial folding, wedging bending where viscous magma intrudes a geologically weaker host rock (Fig. 4H; Spacapan et al., 2017).

Seismicity monitored during intrusion episodes is thought to be associated with the intrusion front and gives access to information on the dynamics of the intrusion tip. Sigmundsson et al. (2015) and Ágústsdóttir et al. (2016) reported on a stunning dataset on the dyke intrusion leading up the Bárðarbunga eruption in August 2014. The dyke propagated laterally for great lengths before finally erupting. The located seismic signals, attributed to the dyke tip, show the seismicity front advancing in bursts. Curiously enough the moment tensor solutions all displayed shear as the cause of seismicity. Moreover, the origins of seismicity were dominantly one-sided in their sense of shear (White et al., 2011, Ágústsdóttir et al., 2016). However, although the seismic sources all appear in a localized manner it has been also proposed that these are in fact not directly attributed to the tip but to the local surrounding volume of host rock responding to the tensile opening.

Several models have been developed to explain tip deformation associated with intrusion (Fig. 4) and the nature of the tip, or process zone remains debated. The established model of sheet intrusions commonly assumes a linear elastic behaviour of the host and a tensile opening of the tip and a tip cavity is expected. The opening, or failure criteria, of the tip is generally governed by an empirical value called the *fracture toughness*, K_c (Rubin, 1995). However, it has long been acknowledged that there are sheet intrusions which do not fit the general description provided by tensile fracture and linear elastic behaviour of the host (Pollard, 1973). Vachon and Hieronymus (2016) demonstrated numerically that allowing for plastic deformation in the host of an ellipsoidal crack blunted the intrusion tip similar to some observations of blunt intrusion tips in nature.

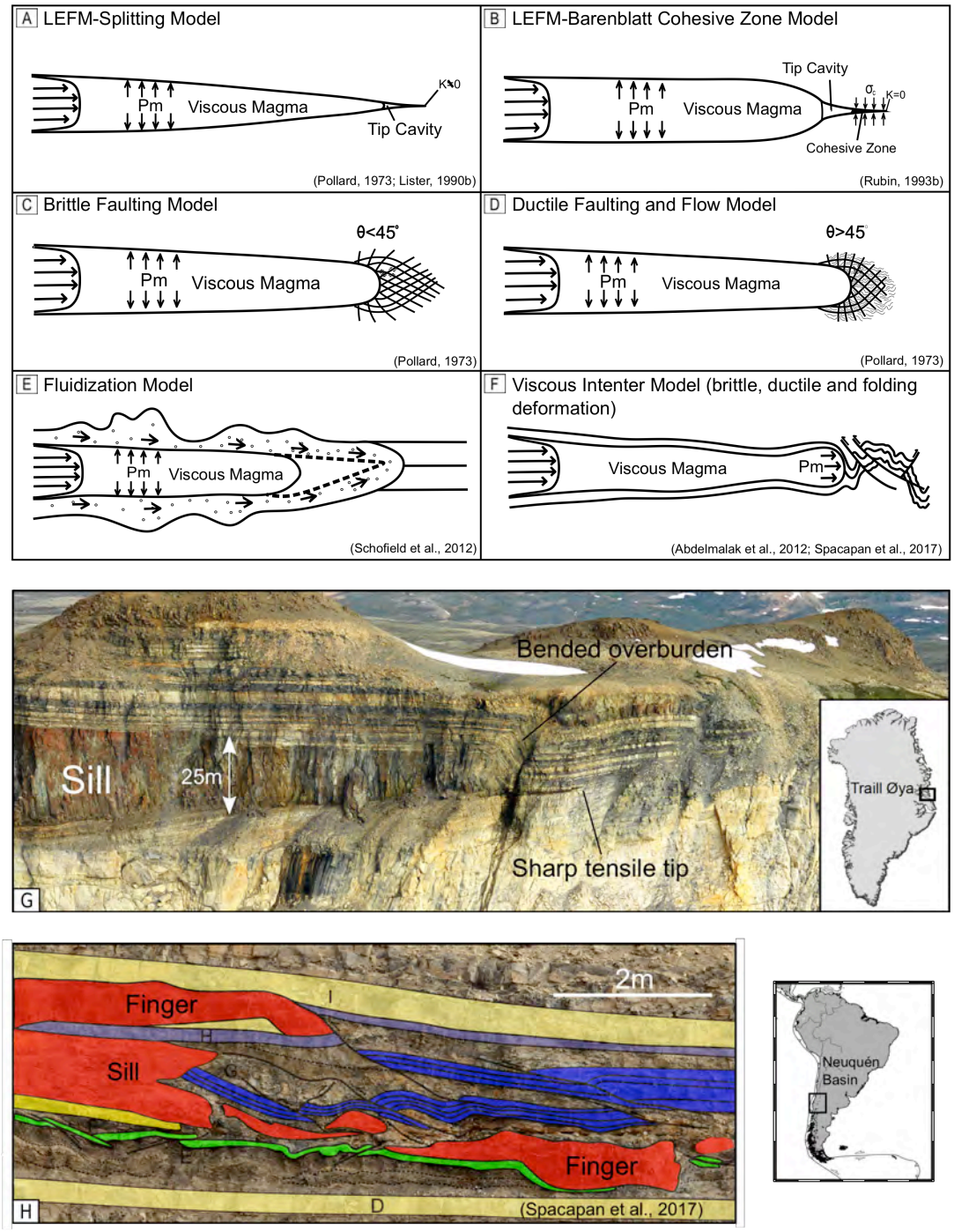

Figure 4. Top schematics show proposed models for propagation and emplacement of sheet intrusion. Bottom photos show field photos of deformation observed in association with intrusions. G demonstrates intrusion associated with sharp tensile tips. H shows sheet intrusions associated with substantial inelastic deformation and shear failure ahead of the intrusion (figure used with permission from Galland et al., 2018a).

This review demonstrates the differing nature of magma propagation and emplacement. It is obvious that the observations demonstrate a diversity of deformation and emplacement mechanics yet models predominantly only allow for linear elastic deformation and tensile opening. Therefore the question of *how the host rock deforms, in small scale, to accommodate intruding magma* remains. So that if small-scale deformation, in 2D, associated with the propagating crack-tip can be resolved, then we might be able to improve upon existing models of sheet propagation and emplacement.

3.2 Large-Scale Deformation

The previous section demonstrated how small-scale deformation is of great importance in interpreting and developing models for magma emplacement. In large-scale deformation we will consider the deformation in the far-field occurring around the intrusion. An accessible way to assess this in nature is to monitor surface deformation. This has been an emerging field of studies that has greatly developed during the last 20 years. Early measurements relied greatly on tilt measurements, levelling and triangulation (e.g. Fiske and Kinoshita, 1969, Tryggvason, 1994). Although tilt measurements are still commonly used and allow for a high temporal resolution, they do not allow for a complete mapping of the deformation field. More recent techniques include the use of Light Detection and Ranging (LIDAR) and aerial or ground-based Photogrammetry (e.g. Pesci et al., 2007, Diefenbach et al., 2012). However, the great advancements lie now with satellite observations, like the Global Navigation Satellite Systems (GNSS) such as GPS and GLONASS, and Interferometric Synthetic Aperture Radar (InSAR). The network of positioning satellites now allow for high temporal resolution (Continuous GPS, CGPS) of a point in 3D space but is still impractical for the capture of the entire deformation field but allows for dynamic modelling (e.g. Segall et al., 2001). However, many of the current strain, tilt and CGPS monitoring are being discontinued (Fernández et al., 2017). The primary method of monitoring for the future appears to be predominantly through InSAR. This system has a great advantage in being able to map the entire of deformation field with respect to a reference digital elevation model. The temporal resolution is increasing with the expected addition of new satellites and can now capture new satellite radar images each day (Fernández et al., 2017). In brief, InSAR relies on a satellite making several passes monitoring the radar distance in swathes producing a set of SAR images in the satellites line-of-sight. Subsequent images can be differenced with the initial image to produced interferograms to show the change in ground elevation with the temporal resolution decided by the time between satellite passes. This can allow displacement to be resolved down to millimetre scale (Dzurisin and Lu, 2007). Many InSAR studies of the past decade have resulted in stunning images revealing the deformation pattern of intruding magma. Notably the deformation pattern of Bárðarbunga eruption garnered a lot of attention (Sigmundsson et al., 2015).

Surface deformation in volcanic areas can display both subsidence and uplift (Fig 5.). While inflation is thought to be due to influx of magma, the pressurization of a storage of magma and/or the injection of a new intrusion. Often inflation or deflation is characteristically observed to be in a roughly axisymmetric fashion (Massonnet et al., 1993, Lanari et al., 1998, Amelung et al., 2000, Pritchard and Simons, 2002). Subsidence is generally thought to be the result of decrease in magma pressure, drainage of magma or cooling/crystallization processes (Massonnet et al., 1995, Pritchard and Simons, 2002). There is a third very characteristic pattern showing two uplifted bulges separated by a localized narrow band of very low or subsiding deformation separating the two bulges (Rubin and Pollard, 1988, Biggs et al., 2009, Nobile et al., 2012).

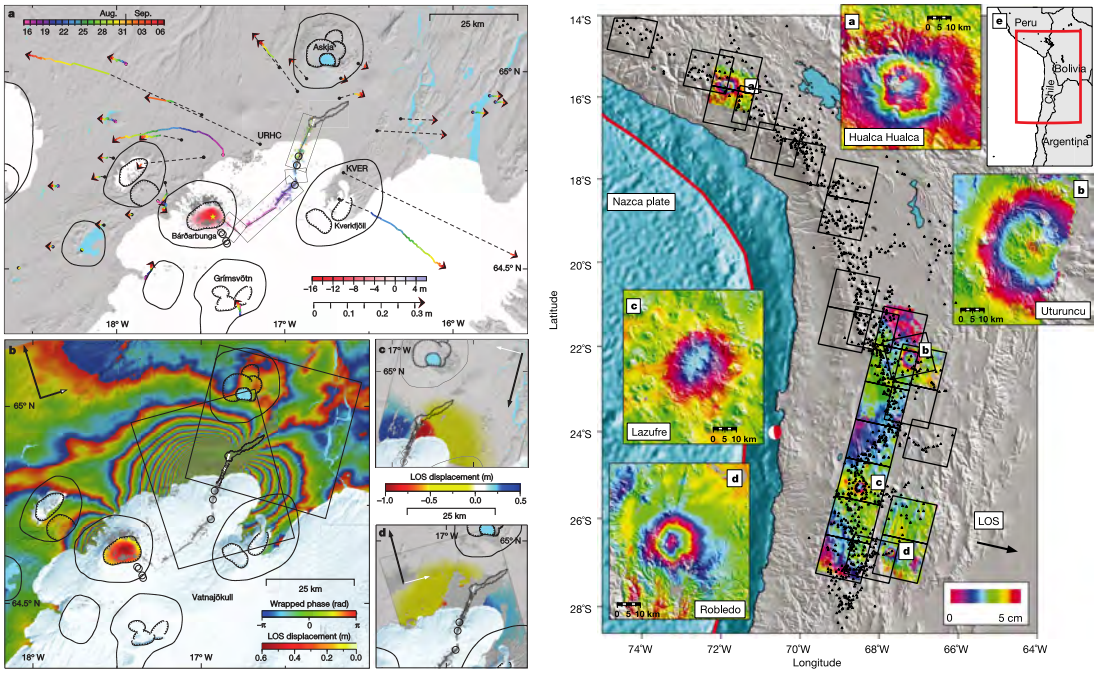

Figure 5. Examples of large-scale surface deformation monitored in volcanic environments. The lower left shows two bulges separated by a trough while the upper left inlay shows subsidence in the Bárðarbunga caldera (figure used with permission from Sigmundsson et al., 2015). Right figure shows several areas of axisymmetric uplift occurring in volcanic centres in the Andes (figure used with permission from Pritchard and Simons, 2002).

The common approach to modelling the described surface deformation is using prescribed geometries and static volume or pressure change in a semi-infinite elastic half-space (Battaglia et al., 2013a). These analytic models approximate the geometries of various intrusions shapes observed in the field such as sheets (Okada, 1985, Fialko et al., 2001), conduits (Bonaccorso and Davis, 1999), spheres (McTigue, 1987) and prolate spheroids (Yang et al., 1988). However, one of the most used is that of a pressurized point source, or the Mogi-model (Fig. 6; Mogi, 1958). This is commonly used to fit inflating or deflating axisymmetric deformation and is thought to approximate the behaviour of a magma chamber (e.g. Cayol and Cornet, 1998b, Cayol and Cornet, 1998a). The other dominant

model is that of the Okada-model commonly used for both horizontal and vertical sheet intrusions. This consists of a rectangular dislocation and can be configured to represent both tensile and shear dislocation. The tensile version is commonly used for sills and dykes and shear dislocation is commonly used in modelling deformation due to earthquakes. The vertical tensile version configuration of Okada's model produces a deformation pattern consisting of two bulges separated by a trough of subsidence (Fig. 6). This is similar to the surface deformation patterns commonly seen in rifts. However, Okada's model does not account for rifting. In general, it is common to combine several static elastic sources to fit the observed deformation in nature (e.g. Biggs et al., 2009).

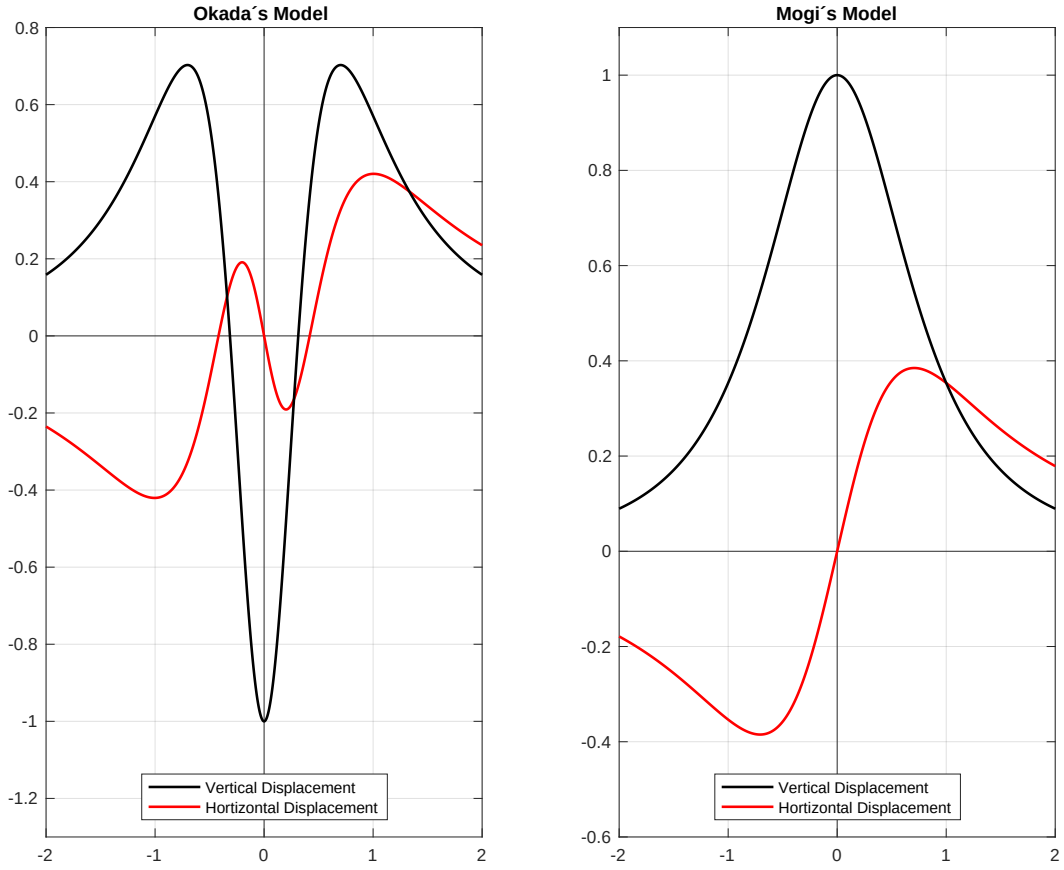

Figure 6. (Left) The instantaneous elastic response in the surface produced by an opening vertical configuration of Okada's model (Battaglia et al., 2013b). (Right) The instantaneous elastic response at the free surface produced by a pressurized Mogi point source (Mogi, 1958). The deformation has been normalized by the absolute maximum vertical displacement. The horizontal axis has been plotted until 2 times the depth to the centre of the vertical sheet in Okada's formulation (Left) and until 2 times the depth of the source for the Mogi point source (Right).

Even if the former paragraphs describe the common approach, several have attempted to build on the current understanding and include mechanics relevant to volcanic systems. The common deformation modelling techniques are often static but many do indeed develop dynamic models (e.g. Segall et al., 2001, Anderson and Segall, 2013, Montagna and Gonnermann, 2013). These attempt to explain the modelled deformation through dynamically evolving models, which is physically relevant in volcanic system, but are often limited to linear elastic rheology of the host. For these reasons numerical models accounting for elasto-plastic deformation have been developed (e.g. Got et al., 2013). An interesting piece of work was performed by Holohan et al. (2017) who looked at the effect of host rock fracturing on the signal of common elastic source models. It indicates that host rock fracturing acts to localize the surface deformation. If this is the case it might be possible that fitting of elastic source models to heavily fractured rock might underestimate the size of intrusion. This may be one of the reason for the discrepancy between modelled magma volume and the measured erupted volume of magma (e.g. Jay et al., 2014). Finally, the geology and topography of a local site may have important effects on intrusion emplacement (e.g. Cayol et al., 2014, Chaput et al., 2014). These demonstrate that shearing of sills may be attributed to the weight of the overburden and the inclination of geological formations. The local site geology and topography will be an integral part in understanding the local intrusion emplacement. However, this will not provide a general understanding of intrusion mechanics.

There are several limitations to the current fitting of models to natural surface deformation. Firstly, they mainly allow for static elastic deformation. The previous chapter shows that in many cases inelastic deformation may be non-negligible. Secondly, intrusion processes are dynamic while most models used are static. Moreover, deformation has been observed showing only uplift where surface fractures suggest that deformation was induced by a dyke, which does not match the Okada model (Jay et al., 2014). Exhumed dykes show that they do not only occur in rifts and do not always involve low-viscosity magma and strong crust (Fink, 1985, Poland et al., 2008). A Mogi point source offers the possibility to compare and benchmark different deformation studies but is not particularly relevant for the physics of volcanic systems. Therefore my second goal of this research project was to study *how large-scale surface deformation reflects the subsurface processes* using laboratory models of intrusions and their associated surface deformation.

4. Laboratory Modelling of Intrusions

Laboratory modelling of intrusions allows for benchmarking existing models and development of new understanding. There are many different setups and subtleties to how intrusions can be modelled. This chapter will be an attempt to cover the general experimental approaches regarding choice of fluid and host and their implications for the shallow crust.

4.1 Laboratory Models Used to Model Magma Intrusion

Hubbert (1937) stated that to properly scale a model to its natural prototype one needs to fulfil three similarity criterions; geometric, kinematic and dynamic. This means that models must scale accordingly to its natural prototype in length, velocities and mechanical forces. This developed rigorous scaling techniques for physical models of geological processes. However, in some cases it is not as important that the model scale relative to the prototype but that the internal scale of the models match that of the corresponding natural prototype. As demonstrated by Ribe and Davaille (2013), for dynamical similarity to be true the density distribution need not be a constant multiple of the prototype. Instead, several densities can in fact be used as long as their internal scale matches. This is due to the fact that geological processes can generally be considered inertia free processes. However, matching specific sites or choosing to narrow a parameter range may lead to a limited understanding of the processes. A general approach to study systems in which the complex physics is unknown is to study the parameter space and apply dimensional analysis to identify the governing dimensionless ratios of experimental parameters and compare to how this is applicable to geological systems (Gibbings, 2011).

The common linear elastic assumption of host rock rheology when modelling intrusions, in near-field and far-field deformation, produces a general good fit to that of experiments in gelatine where low-viscosity fluids such as water or air is injected (Acocella and Tibaldi, 2005, Kavanagh et al., 2013, Le Corvec et al., 2013). Gelatine models have many advantages in that it has a well-defined rheology in addition to being transparent (so that you can track the intrusion at depth) and birefringent (so that you through polarized light can qualitatively monitor stress build-up in the host). Recent advances in experiment monitoring also allow for capturing fluid flow within the intrusion along with strain and surface displacement in the host (Kavanagh et al., 2018). The rheological behaviour of gelatine is largely dependent on the gel concentration, temperature and the time that you allow it to set, or curing time. To simplify it, longer curing time allows for a stiffer gel with intermediate times also allowing for viscous behaviour (Di Giuseppe et al., 2009, Kavanagh et al., 2013). Through stacking of blocks of gelatine one can model the effect of

mechanical discontinuities in gelatine and study the deviation of vertical sheet intrusions to horizontal sheets (Rivalta et al., 2005, Kavanagh et al., 2015).

The gelatine and water/air experiments model an end-member where the magma is fluid, i.e. of low viscosity, and the host is strong, i.e. very cohesive. However, the use of water or air in experiments neglects the viscous stresses due to flow of magma and may not accurately model geologic conditions. A potential second end-member in the relationship between fluid viscosity and host strength is when high viscosity fluids intrudes weakly cohesive materials such as in the case for plutonic intrusion such as granites (Galland et al., 2018b). In this case common materials are polydimethylsiloxane (PDMS), a viscous silicone putty and cohesionless sand (Roman-Berdiel et al., 1995, Corti et al., 2005, Girard and de Vries, 2005).

Intrusions in the shallow crust cover a large range of viscosities ($10^{2\text{-}15}$ Pa s) and host rock strength (Scaillet et al., 1997). Rocks, and the shallow crust, do not only deform elastically, as evidenced by the previous review of observations in nature, but is not completely cohesionless either, instead it is a cohesive Mohr-Coulomb material (Jaeger et al., 2009). Therefore experiments have been developed using vegetable oil and cohesive silica flour (Galland et al., 2006, Galland et al., 2007, Abdelmalak et al., 2016). Silica flour, after compaction, is cohesive and sustains vertical walls. Galland et al. (2014) showed that by intruding a vegetable oil, under the trademark Végétaline, into compacted macroscopically homogeneous cohesive silica flour, representative of intermediately viscous magma intruding host rocks common to sedimentary basins, it was possible to create vertical sheet intrusions, similar to dykes (Fig. 7). Moreover, by independently varying injection velocity, injection depth and injection source diameter this experimental setup can produce both dykes and cone sheets, the first model to be able to so, and that this transition is determined by a power law relationship governed by two dimensionless parameters (Galland et al., 2014). The first dimensionless ratio being the aspect ratio of depth to diameter of the inlet and the second ratio considering the product of viscosity and injection velocity divided by the cohesion times inlet diameter. Such that dykes would be favoured in where the source is small and deep and cone sheets when the source is shallow and wide. Schmiedel et al. (2017a) showed that, including a mechanical weakness, represented by a coarse net, and varying the host rock strength, it was possible to create sills, saucer-shaped sills, cone sheets and punched laccoliths. This is to my knowledge the only experimental setup able to produce such a wide variety of intrusion shapes in a very generalized setup and by only varying the governing physical parameters. However, it is difficult to quantify the effective elastic properties of cohesive granular media making it difficult to scale the models to that of nature.

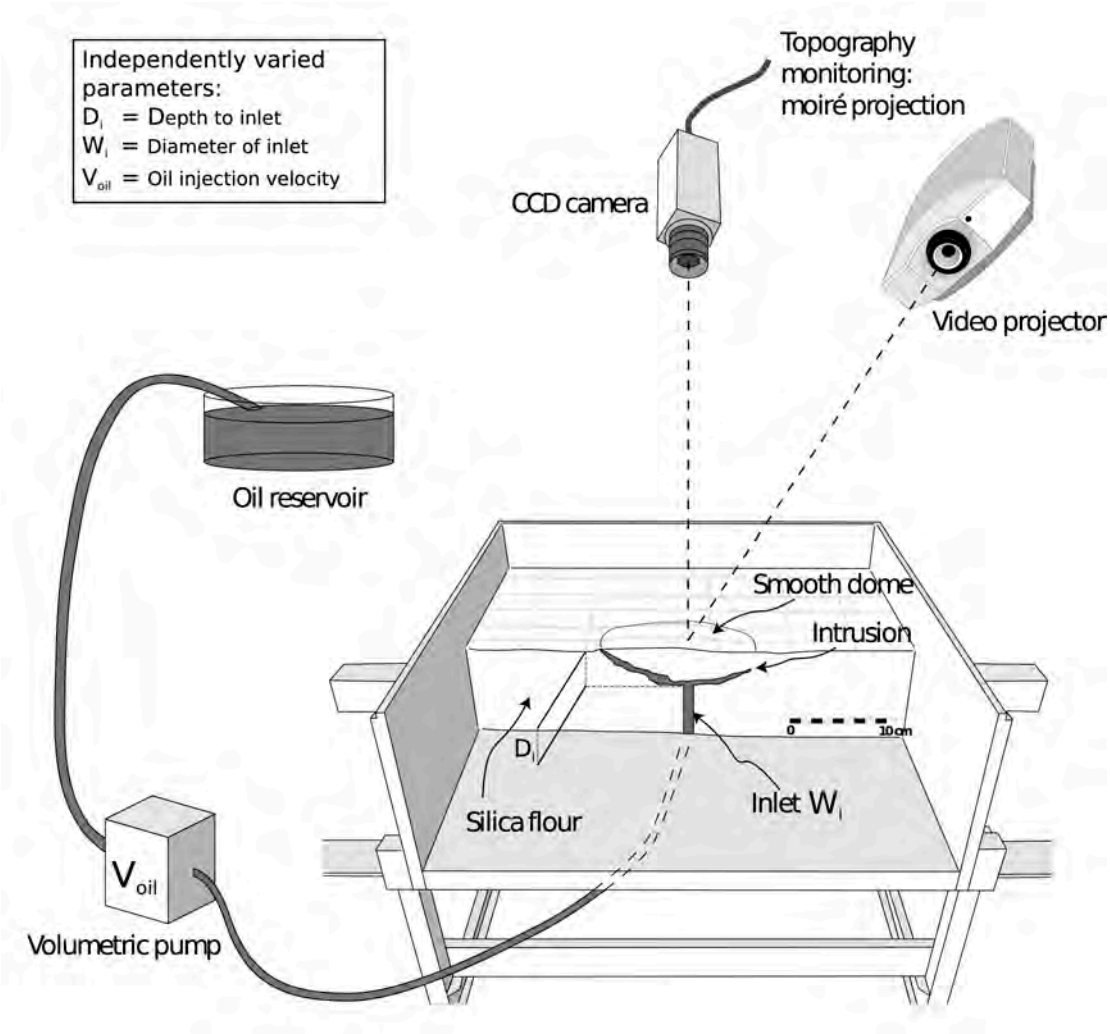

Figure 7. The experimental setup used by Galland et al. 2014 including the Moiré monitoring system. The system uses cohesive silica flour into which a vegetable oil is injected. The oil solidifies once it reaches room temperature making it possible to excavate and study the intrusion shape. Through varying injection depth, inlet diameter and injection velocity, Galland et al. 2014 showed it was consistently possible to create both sub-vertical dykes and cone sheets in the same simple laboratory setup.

Surface deformation was monitored during the experiments that was presented in Galland et al. (2014). The monitored surface deformation is presented and analyzed in Guldstrand et al. (2017) & Guldstrand et al. (2018), included in this thesis. The vertical sheet intrusions do not show a surface deformation patterns matching that of the elastic models or the dykes observed in rifts in the InSAR report. The dykes into cohesive silica flour only showed uplift, initially in an axisymmetric pattern. This pattern instead developed asymmetry with time. However, it was far from the typical Okada model pattern where there are two bulges separated by a trough of subsidence. Abdelmalak et al. (2012) used a 2D setup intruding a more viscous fluid, golden syrup, into similar cohesive material and showed how the intrusion tip of dykes into such materials are associated with shear bands extending from the tip and so uplifted.

This is very different from the theoretical models of linear elastic fracture and gelatine models. So even though cohesive silica flour and viscous fluid intrusion models explain a wide variety of intrusion geometries, there are still questions left to answer. What is the nature of the Okada surface deformation pattern and when is it valid? How does rifting influence viscous intrusion into silica flour models? Geological intrusion scenarios cover a wide range of possible cases that appear to be needed to account for when studying and monitoring surface deformation.

4.2 Monitoring of deformation in Laboratory Models

4.2.1. Deformation monitoring in Laboratory Models

Extracting physical relationships in laboratory models requires precise monitoring to be able to quantify the desired parameters such as pressure, stress but in this thesis, specifically deformation. Many methods are available depending on what aspect of deformation that is being modelled. Early experimental deformation studies used photographs and square grids to be able to quantify strain through strain ellipses (Dixon and Summers, 1985, Dixon and Simpson, 1987, Nilforoushan et al., 2008). Recent techniques to capture strain and fluid movement in experiment photography include Particle Image Velocimetry, PIV, a method that tracks the displacement of particles (Abdelmalak et al., 2012, Mourgues et al., 2012, Bureau et al., 2014) and Digital Image Correlation, a method that identifies patterns in the images and tracks their displacement (Le Corvec and Walter, 2009, Burchardt and Walter, 2010, Kavanagh et al., 2017).

More recently, laser scanning is commonly used to monitor the complete surface elevation and so the surface deformation. The time of flight of a laser pulse is easily converted into distance (Nilforoushan et al., 2008, Trippanera et al., 2014, Kavanagh et al., 2018). The advantage of using laser monitoring is that they have high temporal resolution capable of making several measurements at a given spot. However, scanning a complete surface can take time, which is a limiting factor for the method. Because of such limitations, Galland et al. (2016) devised a method to use open-source Structure-from-Motion software MicMac, which uses photogrammetry to monitor the surface of the models. This will be explained in further detail below.

4.2.2. Moiré Monitoring

The monitoring of surface deformation analyzed in Guldstrand et al. (2017) and Guldstrand et al. (2018), part of this thesis, uses a moiré projection technique (e.g. Bréque et al., 2004). This technique assesses distance based on the deformation of fringes of structured light projected onto a surface so that a distance model can be created. Sets of slowly moving fringes are projected on to the surface, a so-called moiré pattern. These are recorded with a video camera so

that a complete scan of the surface takes 1.5 seconds. A total of 8 images were produced for a single scan. These images can then be used to calculate a digital elevation model of the surface at a given time of scan. However, the drawback with the scanning time of the surface causes the obtained surface to be a smoothed or averaged surface of the dynamic intrusion process. This issue is of greater importance especially for shorter experiments. Moreover, it does not allow for extracting vertical and horizontal components of deformation. As such this was not a fully optimal method for studying deformation but allowed for identifying key first order observations of the dynamic surface deformation above laboratory models in a cohesive coulomb brittle crust.

4.2.3. PHOTOGRAMMETRY, STRUCTURE-FROM-MOTION AND DIGITAL IMAGE CORRELATION THROUGH THE USE OF MICMAC

Using moiré monitoring, although it produced relevant results, is not an optimal technique to monitor surface deformation. The scanning of the surface resulted in an averaging of the surface deformation during the time the scan was made. Moreover, the fringes were not perfectly matched at all times so these fringes can still be slightly visible in some digital elevation models. Instead a system using the open-source Structure-from-motion software MicMac developed by the French national institute of geography (IGN). It is a mostly command line based software working best on Linux OS. This allows for computing orthophotos and digital elevation models (DEMs) from the use of several photos of an object and photogrammetry. An orthophoto is a photo that has been corrected for camera distortion and distortions of perspective, such that it is effectively an equal distance map projection. In our laboratory models we use 4 cameras covering the model with 100% overlap. Because these are all fixed lens cameras with the same specifications we may treat them as one camera. Our cameras take synchronised images each second through a custom designed Arduino® setup. The four images in the first time step are then analyzed for their camera distortion parameters and corrected and applied to all subsequent time steps. Through points of known coordinates, we can convert the arbitrary scale to real world scale. MicMac identifies feature points in the images to create the outputs so it is important that the models have texture. Therefore we apply sieved olivine sand and coffee powder. The setup allows us to create high resolution DEMs and orthophotos at a high temporal resolution.

The orthophotos can then be analyzed with MicMac's own implementation of Digital Image Correlation; MM2DPosSism. This can be used on any photo to analyse strain and deformation. This was done for manuscript 9.4 on which experiment photos were taken and corrected for lens distortion in MATLAB's image toolbox to study the internal host deformation of a viscous 2D dyke intruding into hosts of varying cohesion (Fig 8).

Figure 8. The 2D Hele-Shaw setup filled with compacted cohesive fine-grained host. The intruding fluid is golden syrup injected at constant flow. Fine-grained aluminium silicate has been introduced into the host such that it is possible to apply Digital Image Correlation to study small deformations.

5. SUMMARY OF MANUSCRIPTS

3 articles and 1 manuscript were produced during the period of work for this PhD thesis, aimed at answering the previously stated research aims but also at improving experimental methods. The following describes which research questions are addressed by which manuscripts.

- (1) *How does the host rock deform, in small-scale, to accommodate intruding magma? :* Publication 2 / In prep. Manuscript 4

- *(2) How does large-scale surface deformation reflect the subsurface processes?* : Publication 1 / Publication 2 / Publication 3

- *(3) Under which conditions can a propagating fracture filled with viscous fluid best be described by Linear Elastic Fracture Mechanics models or Viscous Indenter models and if both models apply how do the transition between the two appear? :* Publication 2 / In prep. Manuscript 4

In this chapter, I will briefly summarize the main results and conclusions of the articles and comment on how they fit into the broader scientific setting established in previous chapters. The publications and manuscript are available in its entirety in chapter 9.

5.1 PUBLICATION 1: APPLICATION OF OPEN-SOURCE PHOTOGRAMMETRIC SOFTWARE MICMAC FOR MONITORING OF SURFACE DEFORMATION IN LABORATORY MODELS

The first article, *Application of Open-Source Photogrammetric Software MicMac for Monitoring of Surface Deformation in Laboratory Models,* aimed at describing the use of an open-source source photogrammetric software in generating high resolution deformation monitoring. My contribution consisted in performing experiments, development of MicMac scripts, computation and analysis, producing figures, strategic discussions and commenting on manuscript text. It was published in *Journal of Geophysical Research: Solid Earth* on the 4th of March 2016.

Experimentalists rely on being able to accurately and precisely monitor quantities in experiments to extract physical relationships and explain the studied process. In this article, we focused on extracting deformation data through studying the changing laboratory model surface. As presented in the previous chapter, extracting a lot of surface data at a high temporal resolution can be challenging. We introduce the use of the open-source photogrammetric software MicMac in monitoring surface deformation in laboratory models. This software has been developed by the French national geographical institute (IGN) and was primarily intended for aerial mapping. The basic outputs of MicMac include orthophotos and digital elevation models. These are created from

multiple photos perpendicular to an object with a sufficient overlap and texture. We apply olivine sand and ground coffee powder to the experiment surface to produce a texture for the algorithm. The software finds tie-points, i.e. points with the same real word location, in different photos. This allows for creating a relative orientation between the photos and correcting for lens distortion. By using four identical cameras focused on the same point, we can apply the same camera distortion to all cameras throughout the series. We measure four known points (Ground Control Points) on the model to be used to convert from an arbitrary computer vision scale to a real world scale. Synchronized shooting of the cameras allows us to capture high-resolution images of the surface at 1-second intervals and construct orthophotos, digital elevation models (DEMs) and point clouds. Using MicMac's own digital image correlation algorithm on the orthophotos allows for detecting small displacements in the plane of the orthophoto, in our case these correspond to horizontal displacements.

Simple post-processing of the DEMs in MATLAB allows for the creation of differential ΔDEMs to study the evolving surface. Horizontal displacements are an interesting data output on their own but can also be used for computing shear strain and divergence, which allows for mapping extensional and compressional faults, fractures and their kinematics. A simple statistical analysis of the data output of several computations and camera orientations showed that we could detect displacements, in both the vertical and horizontal, of sub-millimetre accuracy.

The review in the previous chapters showed that monitoring of deformation can be difficult due to limitations in scanning time of the chosen method. This is not a problem for the setup we propose. Moreover, it comes at a very low cost compared to other systems such as scanners or proprietary setups based on photogrammetry.

5.2 Publication 2: Dynamics of Surface Deformation Induced by Dikes and Cone Sheets in a Cohesive Coulomb Brittle Crust

The second article, *Dynamics of Surface Deformation Induced by Dikes and Cone Sheets in a Cohesive Coulomb Brittle Crust,* used an older dataset comprised of laboratory models in which the surface deformation was monitored using the projection of structured light and moiré interference patterns. This revealed the deformation in experimental large scale above dykes and cone sheets in a cohesive coulomb material. This was seen to differ greatly from that expected of tensile elastic models. My contribution consisted in performing computation and analysis, producing figures and writing the main part of the manuscript text. It was published in *Journal of Geophysical Research: Solid Earth* on the 21st of October 2017.

The surface deformation captured during the dyke and cone sheet experiments of Galland et al. (2014) allowed for a dataset of 37 analysable experiments. These experiments showed that it is possible to systematically produce dykes and cone sheets using vegetable oil and compacted cohesive silica flour failing according to a coulomb criterion by only varying key parameters. These include injection depth, injection flow rate and injection source diameter. Through dimensional analysis, it could be demonstrated that the separation of the two parameter-spaces defined a power law. The study applied a moiré monitoring technique described in the previous chapter. The experiments showed that both dykes and cone sheets formed an initial axisymmetric area of uplift that gradually developed an asymmetry. We extracted the uplifted area, volume and the point of maximum uplift and studied their evolution.

The scaled evolution of the maximum uplift showed that for dykes, a two-stage or two-phase evolution exists. First showing slow a rate of uplift, which then accelerates for the second phase. Cone sheets showed a quick initial uplift and then developed quasi-linearly for the remainder of the experiment. The scaled evolution of the uplift area quickly reached a plateau and was always larger for cone sheets than for dykes. The scaled dynamic uplift, that took into account the difference between injected volume of oil and uplifted volume of the host, showed that cone sheets uplift the material above it to a larger degree than dykes. Finally, addressing the development of asymmetry through studying the deviation of the full surface DEM from a mean symmetric profile showed that it developed similarly to the evolution of the point of maximum uplift. Thus successfully identifying and tracking the point of maximum uplift acts as proxy for the overall evolution.

This paper highlights the difference between established model of tensile sheet intrusions in a linear elastic medium and sheet intrusions in Mohr-Coulomb materials. Our experimental dykes show uplift at all times during the experiment in contrast to the bulge-trough-bulge pattern produced in gelatine and by Okada's model. Moreover, we document the surface deformation associated with cone sheets. Cone sheets remain poorly understood and modelled despite being observed in nature. Our experiments show that fundamental intrusion geometries such as dykes and cone sheets can form just by varying essential parameters in the volcanic plumbing system and that there is still work to be done to understand what generates the surface deformation seen in nature.

5.3 Publication 3: Experimental Constraints on Forecasting the Location of Volcanic Eruptions from Pre-Eruptive Surface Deformation

The third article, *Experimental Constraints on Forecasting the Location of Volcanic Eruptions from Pre-Eruptive Surface Deformation,* analyzed the experimental surface deformation for precursors that could be useful in identifying the forthcoming eruption location without the use of heavy computational modelling. My contribution consisted in performing computation and analysis, producing figures and writing the main part of the manuscript text. It was published in a special issue called *Towards Improved Forecasting of Volcanic Eruptions* in *Frontiers in Earth Science* on the 20th of February 2018.

Volcanic deformation is commonly monitored in nature and studied to understand volcano behaviour and if they are about to erupt. We used our experimental surface deformation dataset to try to extract proxies relevant for forecasting the eruption without assumptions of intrusion geometry and emplacement mechanics. To do this we identified a vector connecting the centre of the uplifted area and the point of maximum uplift. This vector was initially random in orientation and very short. With time this vector elongated and stabilized and finally pointed to location of the eruption. More importantly, the vector pointed to the general area of eruption before eruption occurred once localization of the vector started. We defined localization to be when the change in angle between the vectors of two subsequent time steps was below 20°. This was true for both dykes and cone sheets. In dykes, this occurred fairly late at ~60% of the total experiment duration. For cone sheets this localization occurred much earlier, at ~30% of the experiment duration. The elongation of the vector showed that dykes exhibit a first period where the vector is short, a transitional phase where the vector elongates rapidly and a final phase where the elongated distance is near constant. The vector development for cone sheets continually elongated throughout the experiment.

Our experiments show that, for intrusions not occurring in rifts, where deformation is monitored with sufficient spatial and temporal resolution, it may be possible to forecast the eruption without the use of costly computational modelling. Our experiments do not include the effect of topography and crustal heterogeneities but we expect the surface deformation would still reflect the subsurface asymmetry. Similar analysis have been performed on surface deformation in nature (Toutain et al., 1992). Moreover, computing the average centre of the uplifted area should give information on the amassing of magma at depth with the shallowest point represented by the maximum uplift. As such, with the improving coverage and availability of satellite imagery and automated processing, we expect this to be a relevant analysis in the future.

5.4 In Prep. Manuscript: Emplacement and Propagation of Viscous Laboratory Dykes and the Associated Quasi-2D Deformation in Cohesive Mohr-Coulomb Hosts

The final article manuscript, *Emplacement and Propagation of Viscous Laboratory Dykes and the Associated Quasi-2D Deformation in Cohesive Mohr-Coulomb Hosts,* studies the internal host deformation and deformation at small scale associated with the tip of a propagating viscous intrusion into a cohesive Coulomb host. My contribution consisted in designing the setup, developing the analyses, performing computation and analysis, producing figures and writing the main part of the manuscript text. It is currently in preparation with intended submission to *G^3 (Geochemistry, Geophysics, Geosystems)* over the course of the summer 2018.

The 8 experiments in this manuscript are performed in a thick 2D Hele-Shaw cell that is lined with glass plates. Among these 8 experiments, 4 were performed to assess the repeatability of the setup. Black tracer particles were introduced into the host, which allows for tracking the internal host deformation associated with the intrusion by using digital image correlation (DIC). The only parameter varied was the cohesion of the host by using four mixes of glass beads and silica flour. Viscous golden syrup was used as the model magma.

The experiments showed a transition from vertical sheets to finger structures depending on the host cohesion. Strong cohesion resulted in clear sheet like geometry (2D), while lower cohesion resulted in a finger shaped intrusion (3D). In all experiments, intrusion was associated with uplift of the surface and small-scale uplift associated with the tip. The uplift was larger for low cohesion hosts compared to high cohesion. The horizontal displacements show that for low cohesion host deformation is mainly associated with the intrusion tip. High cohesion hosts demonstrated opening along the entire fracture wall during the propagation at depth. The drastically different pressure inlet measurements between low and high cohesion experiments verify potentially two different emplacement mechanisms at work. Propagation velocities were extracted from the images and showed that the propagation exhibited a burst-like dynamic similar to that reported from seismic studies.

Although only 8 experiments were produced for this manuscript the use and repeatability of this setup and experiment has been demonstrated at length by Abdelmalak et al. (2012). These experiments again show the versatility of the cohesive coulomb models in bridging the gap between different end-member models of magma emplacement. The first being finger-like intrusions, such as those visible in association with the extremities of both dyke and cone sheets, but also from highly viscous intrusion such as cryptodomes. The second being sheet intrusion such as dykes. It challenges consensus model of sheet intrusion being primarily tensile in a linear elastic host and the associated surface

deformation with such models. It is a first step in establishing a continuum in the ranges of possible intrusions into strong hosts favouring elastic deformation and very weak hosts.

6. Discussion and Outlook

The previous chapters have attempted to give the reader a broad overview of current state of volcanic plumbing systems research and the context to where my research has contributed to the current state of intrusion emplacement understanding. By reviewing the current literature, I have tried to demonstrate the diverse range of intrusion geometries in the VPS and in observations of deformation occurring associated with intrusion of magma in the shallow crust. This in specific settings; (1) In small-scale associated mainly with the tip in outcrops and indirect observations from seismic monitoring; (2) In large-scale associated mainly with surface deformation monitoring in nature. This shows that we have various ways of emplacing magma, through tensile sheet, sheets that push their material ahead of them (*viscous indenters*) and finger-shaped intrusions. The models that we currently use assume hosts that are linearly elastic or completely plastic allowing only for two emplacement mechanisms, tensile failure or shear failure. Moreover, magma viscosity is often neglected in magma emplacement experiments and theory, although it is often mentioned to be an important property. This leads to the formulation of my first research question of how the host rock deforms, in small scale, to accommodate intruding magma? A first series of experiment have been attempted to address this in the fourth manuscript. By using mixes of cohesive Mohr-Coulomb flour, we could study the effect of host cohesion on fluid intrusion. Firstly, this flour is more similar to the rheological behaviour of the shallow crust. It allows for cohesion such that the material can sustain vertical walls and distributed stress, but will also fail in shear. The experiments shows that varying the cohesion will allow sheet intrusions in strong hosts and finger shaped intrusions in weak hosts. With differing emplacement mechanisms associated with the two, however, both are associated with uplift. More importantly, this allows us to study the intrusion process as part of a continuum instead of confined to end-members. To improve these models, we would need a better grasp of the elastic properties of such materials and also to study the influence of rifting on the intrusion process.

The applicable goal of volcanology is naturally to understand the intrusion process such that we could predict volcanic eruptions with certainty. The observed surface deformation is a key parameter in this. The previous review shows that we have various fundamental patterns observed, axisymmetric subsidence, axisymmetric uplift and the bulge-trough-bulge pattern. Modelling these have primarily been done through applying static models only assuming elastic behaviour of the host even where the crust has been proposed to be weak, such as in Iceland (e.g. Thun et al., 2016). Some of these models have a very small physical relevance in terms of intrusion geometry such as the Mogi (1958) point source often used for uplifts. The model

that is used is assumed based largely on the pattern that is observed, such that the dataset of what the surface deformation is attributed to can lead to being somewhat biased. Thus this lead to my second research question, how will large-scale surface deformation reflect the subsurface processes?

The models presented by Galland et al. (2014), Schmiedel et al. (2017a) and the fourth manuscript in this thesis show that allowing for a Mohr-Coulomb host and varying key parameters explains to a first order many of the intrusion geometries that have been observed in nature. However, fundamental large-scale deformation associated with key intrusion geometries, such as dykes, differ greatly from experiment to what is expected. Guldstrand et al. (2017) and Guldstrand et al. (2018) demonstrated that the dykes were associated with large-scale uplift and doming at all times, developing an asymmetry similar to volcanic deformation that can be observed. The nature of emplacement must cover a wide range of geological scenarios in terms of relative host strength and viscosity, and the tectonics at play, such as rifting, which is generally not accounted for. My work offers an alternate explanation to many of the uplifts seen in volcanic deformation but does not give a definitive answer on the nature of rifting on large-scale deformation. However, in more applied goals such as forecasting volcanic eruptions, Guldstrand et al. (2018) show that it may not be necessary to understand the emplacement, but instead extract relevant parameters of the surface deformation. This procedure allows for tracking of the centre of uplifted area and the point of maximum uplift. Combining these points to create a vector shows that the evolution of the vector stabilizes in orientation, and allows for forecasting the point of eruption before the fact. Admittedly, we cannot yet predict volcanic eruptions but this analysis may allow for hazard mitigation, given that one has access to deformation data of high spatial and temporal resolution.

The ultimate question of my PhD was to address under which conditions a propagating fracture filled with a viscous fluid could best be described by a linear elastic tensile model, or a viscous indenter type model? The question included a by-line asking that if both models apply, how does the transition between the two appear? Observations and results of modelling support parts of both models. There are sharp tipped intrusions that appear to have opened in tensile mode, but also rounded tips and evidence for forceful intrusion of magma. The sharp-tipped intrusions are successfully modelled using gelatine experiments, however, the 2D intrusions into Mohr-Coulomb hosts also appear to exhibit sharp-tipped intrusion. Okada's model statically reproduces the elastic answer similar to that seen in nature. However, neglecting for the rifting tectonic environment and the fact that monitored seismicity associated with propagation indicate a high degree of shear failure of the tip or surrounding volume of host rock. The nature of uplift in volcanic environments has remained largely unexplained, other than inflating magma chambers, sills or physically infeasible

point sources. Our experiments show that these uplifts could also be related to dyking. Especially considering higher viscosity dykes not occurring in rifts and where the shallow crust is weak. In future considerations for surface deformation modelling, new models have to be developed that take into consideration the geologic setting, however, this is beyond the scope of this thesis. The results in the manuscripts produced during the work for this thesis offer a starting point for understanding the continuum of possible ranges of intrusions as well as the associated deformation and emplacement mechanisms.

7. BIBLIOGRAPHY

Abdelmalak, M., Bulois, C., Mourgues, R., Galland, O., Legland, J.-B. & Gruber, C. 2016. Description of new dry granular materials of variable cohesion and friction coefficient: Implications for laboratory modeling of the brittle crust. *Tectonophysics,* 684**,** 39-51.

Abdelmalak, M., Mourgues, R., Galland, O. & Bureau, D. 2012. Fracture mode analysis and related surface deformation during dyke intrusion: Results from 2D experimental modelling. *Earth and Planetary Science Letters,* 359**,** 93-105.

Acocella, V. & Tibaldi, A. 2005. Dike propagation driven by volcano collapse: a general model tested at Stromboli, Italy. *Geophysical Research Letters,* 32.

Ágústsdóttir, T., Woods, J., Greenfield, T., Green, R. G., White, R. S., Winder, T., Brandsdóttir, B., Steinthórsson, S. & Soosalu, H. 2016. Strike‐slip faulting during the 2014 Bárðarbunga‐Holuhraun dike intrusion, central Iceland. *Geophysical Research Letters*.

Almendros, J., Chouet, B., Dawson, P. & Bond, T. 2002. Identifying elements of the plumbing system beneath Kilauea Volcano, Hawaii, from the source locations of very-long-period signals. *Geophysical Journal International,* 148**,** 303-312.

Amelung, F., Jónsson, S., Zebker, H. & Segall, P. 2000. Widespread uplift and 'trapdoor'faulting on Galapagos volcanoes observed with radar interferometry. *Nature,* 407**,** 993-996.

Anderson, K. & Segall, P. 2013. Bayesian inversion of data from effusive volcanic eruptions using physics‐based models: Application to Mount St. Helens 2004‐2008. *Journal of Geophysical Research: Solid Earth,* 118**,** 2017-2037.

Battaglia, M., Cervelli, P. F. & Murray, J. R. 2013a. dMODELS: A MATLAB software package for modeling crustal deformation near active faults and volcanic centers. *Journal of Volcanology and Geothermal Research,* 254**,** 1-4.

Battaglia, M., Cervelli, P. F. & Murray, J. R. 2013b. Modeling crustal deformation near active faults and volcanic centers—a catalog of deformation models. *US Geological Survey Techniques and Methods***,** 13-B1.

Biggs, J., Amelung, F., Gourmelen, N., Dixon, T. H. & Kim, S.-W. 2009. InSAR observations of 2007 Tanzania rifting episode reveal mixed fault and dyke extension in an immature continental rift. *Geophysical Journal International,* 179**,** 549-558.

Bonaccorso, A. & Davis, P. M. 1999. Models of ground deformation from vertical volcanic conduits with application to eruptions of Mount St. Helens and Mount Etna. *Journal of Geophysical Research: Solid Earth (1978–2012),* 104**,** 10531-10542.

Bottinga, Y. & Weill, D. F. 1972. The viscosity of magmatic silicate liquids; a model calculation. *American Journal of Science,* 272**,** 438-475.

Bréque, C., Dupre, J.-C. & Bremand, F. 2004. Calibration of a system of projection moiré for relief measuring: biomechanical applications. *Optics and Lasers in Engineering,* 41**,** 241-260.

Briffa, K. R., Jones, P. D., Schweingruber, F. H. & Osborn, T. J. 1998. Influence of volcanic eruptions on Northern Hemisphere summer temperature over the past 600 years. *Nature,* 393**,** 450-455.

Burchardt, S., Troll, V. R., Mathieu, L., Emeleus, H. C. & Donaldson, C. H. 2013. Ardnamurchan 3D cone-sheet architecture explained by a single elongate magma chamber. *Scientific reports,* 3**,** 2891.

Burchardt, S. & Walter, T. R. 2010. Propagation, linkage, and interaction of caldera ring-faults: Comparison between analogue experiments and caldera collapse at Miyakejima, Japan, in 2000. *Bulletin of Volcanology,* 72**,** 297-308.

Bureau, D., Mourgues, R. & Cartwright, J. 2014. Use of a new artificial cohesive material for physical modelling: Application to sandstone intrusions and associated fracture networks. *Journal of Structural Geology,* 66**,** 223-236.

Callot, J.-P., Geoffroy, L., Aubourg, C., Pozzi, J. & Mege, D. 2001. Magma flow directions of shallow dykes from the East Greenland volcanic margin inferred from magnetic fabric studies. *Tectonophysics,* 335**,** 313-329.

Cayol, V., Catry, T., Michon, L., Chaput, M., Famin, V., Bodart, O., Froger, J. L. & Romagnoli, C. 2014. Sheared sheet intrusions as mechanism for lateral flank displacement on basaltic volcanoes: Applications to Réunion Island volcanoes. *Journal of Geophysical Research: Solid Earth,* 119**,** 7607-7635.

Cayol, V. & Cornet, F. H. 1998a. Effects of topography on the interpretation of the deformation field of prominent volcanoes—Application to Etna. *Geophysical Research Letters,* 25**,** 1979-1982.

Cayol, V. & Cornet, F. H. 1998b. Three‐dimensional modeling of the 1983‐1984 eruption at Piton de la Fournaise Volcano, Réunion Island. *Journal of Geophysical Research: Solid Earth (1978‐2012),* 103**,** 18025-18037.
Chaput, M., Pinel, V., Famin, V., Michon, L. & Froger, J. L. 2014. Cointrusive shear displacement by sill intrusion in a detachment: A numerical approach. *Geophysical Research Letters,* 41**,** 1937-1943.
Chevallier, L. & Woodford, A. 1999. Morpho-tectonics and mechanism of emplacement of the dolerite rings and sills of the western Karoo, South Africa. *South African Journal of Geology,* 102**,** 43-54.
Chiarabba, C., De Gori, P. & Patane, D. 2004. The Mt. Etna plumbing system: the contribution of seismic tomography. *Mt. Etna: volcano laboratory***,** 191-204.
Corti, G., Moratti, G. & Sani, F. 2005. Relations between surface faulting and granite intrusions in analogue models of strike-slip deformation. *Journal of Structural Geology,* 27**,** 1547-1562.
De la Cruz-Reyna, S. & Siebe, C. 1997. Volcanology: the giant Popocatépetl stirs. *Nature,* 388**,** 227-227.
Di Giuseppe, E., Funiciello, F., Corbi, F., Ranalli, G. & Mojoli, G. 2009. Gelatins as rock analogs: A systematic study of their rheological and physical properties. *Tectonophysics,* 473**,** 391-403.
Diefenbach, A. K., Crider, J. G., Schilling, S. P. & Dzurisin, D. 2012. Rapid, low-cost photogrammetry to monitor volcanic eruptions: an example from Mount St. Helens, Washington, USA. *Bulletin of volcanology,* 74**,** 579-587.
Dixon, J. M. & Simpson, D. G. 1987. Centrifuge modelling of laccolith intrusion. *Journal of Structural Geology,* 9**,** 87-103.
Dixon, J. M. & Summers, J. M. 1985. Recent developments in centrifuge modelling of tectonic processes: equipment, model construction techniques and rheology of model materials. *Journal of Structural Geology,* 7**,** 83-102.
Dzurisin, D. & Lu, Z. 2007. *Volcano deformation--Geodetic monitoring techniques,* Berlin, Springer-Verlag.
Eide, C. H., Schofield, N., Jerram, D. A. & Howell, J. A. 2017. Basin-scale architecture of deeply emplaced sill complexes: Jameson Land, East Greenland. *Journal of the Geological Society,* 174**,** 23-40.
Farrimond, P., Bevan, J. C. & Bishop, A. N. 1996. Hopanoid hydrocarbon maturation by an igneous intrusion. *Organic Geochemistry,* 25**,** 149-164.
Fernández, J., Pepe, A., Poland, M. P. & Sigmundsson, F. 2017. Volcano Geodesy: Recent developments and future challenges. *Journal of Volcanology and Geothermal Research,* 344**,** 1-12.
Fialko, Y., Khazan, Y. & Simons, M. 2001. Deformation due to a pressurized horizontal circular crack in an elastic half-space, with applications to volcano geodesy. *Geophysical Journal International,* 146**,** 181-190.
Fink, J. H. 1985. Geometry of silicic dikes beneath the Inyo Domes, California. *Journal of Geophysical Research: Solid Earth,* 90**,** 11127-11133.
Fiske, R. S. & Kinoshita, W. T. 1969. Inflation of Kilauea volcano prior to its 1967-1968 eruption. *Science,* 165**,** 341-349.
Galindo, I. & Gudmundsson, A. 2012. Basaltic feeder dykes in rift zones: geometry, emplacement, and effusion rates. *Natural Hazards and Earth System Sciences,* 12**,** 3683.
Galland, O., Bertelsen, H., Eide, C., Guldstrand, F., Haug, Ø., Leanza, H. A., Mair, K., Palma, O., Planke, S. & Rabbel, O. 2018a. Storage and Transport of Magma in the Layered Crust—Formation of Sills and Related Flat-Lying Intrusions. *Volcanic and Igneous Plumbing Systems.* Elsevier.
Galland, O., Bertelsen, H. S., Guldstrand, F., Girod, L., Johannessen, R. F., Bjugger, F., Burchardt, S. & Mair, K. 2016. Application of open‐source photogrammetric software MicMac for monitoring surface deformation in laboratory models. *Journal of Geophysical Research: Solid Earth,* 121**,** 2852-2872.
Galland, O., Burchardt, S., Hallot, E., Mourgues, R. & Bulois, C. 2014. Dynamics of dikes versus cone sheets in volcanic systems. *Journal of Geophysical Research: Solid Earth,* 119**,** 6178-6192.
Galland, O., Cobbold, P. R., de Bremond d'Ars, J. & Hallot, E. 2007. Rise and emplacement of magma during horizontal shortening of the brittle crust: Insights from experimental modeling. *Journal of Geophysical Research: Solid Earth,* 112.

Galland, O., Cobbold, P. R., Hallot, E., de Bremond d'Ars, J. & Delavaud, G. 2006. Use of vegetable oil and silica powder for scale modelling of magmatic intrusion in a deforming brittle crust. *Earth and Planetary Science Letters,* 243**,** 786-804.
Galland, O., Holohan, E., van Wyk de Vries, B. & Burchardt, S. 2018b. Laboratory Modelling of Volcano Plumbing Systems: A Review. Berlin, Heidelberg: Springer Berlin Heidelberg.
Gibbings, J. C. 2011. *Dimensional analysis*, Springer Science & Business Media.
Girard, G. & de Vries, B. v. W. 2005. The Managua Graben and Las Sierras-Masaya volcanic complex (Nicaragua); pull-apart localization by an intrusive complex: results from analogue modeling. *Journal of Volcanology and Geothermal Research,* 144**,** 37-57.
Got, J. L., Peltier, A., Staudacher, T., Kowalski, P. & Boissier, P. 2013. Edifice strength and magma transfer modulation at Piton de la Fournaise volcano. *Journal of Geophysical Research: Solid Earth,* 118**,** 5040-5057.
Grattan, J. 2006. Aspects of Armageddon: an exploration of the role of volcanic eruptions in human history and civilization. *Quaternary International,* 151**,** 10-18.
Gudmundsson, A. 2002. Emplacement and arrest of sheets and dykes in central volcanoes. *Journal of Volcanology and Geothermal Research,* 116**,** 279-298.
Gudmundsson, A., Friese, N., Galindo, I. & Philipp, S. L. 2008. Dike-induced reverse faulting in a graben. *Geology,* 36**,** 123-126.
Guldstrand, F., Burchardt, S., Hallot, E. & Galland, O. 2017. Dynamics of Surface Deformation Induced by Dikes and Cone Sheets in a Cohesive Coulomb Brittle Crust. *Journal of Geophysical Research: Solid Earth,* 10.1002/2017JB014346**,** n/a-n/a.
Guldstrand, F., Galland, O., Hallot, E. & Burchardt, S. 2018. Experimental Constraints on Forecasting the Location of Volcanic Eruptions from Pre-eruptive Surface Deformation. *Frontiers in Earth Science,* 6**,** 7.
Hansen, J., Jerram, D., McCaffrey, K. & Passey, S. 2011. Early Cenozoic saucer-shaped sills of the Faroe Islands: an example of intrusive styles in basaltic lava piles. *Journal of the Geological Society,* 168**,** 159-178.
Holohan, E., Sudhaus, H., Walter, T., Schöpfer, M. & Walsh, J. 2017. Effects of Host-rock Fracturing on Elastic-deformation Source Models of Volcano Deflation. *Scientific reports,* 7**,** 10970.
Hubbert, M. K. 1937. Theory of scale models as applied to the study of geologic structures. *Geological Society of America Bulletin,* 48**,** 1459-1520.
Jaeger, J. C., Cook, N. G. & Zimmerman, R. 2009. *Fundamentals of rock mechanics*, John Wiley & Sons.
Jay, J., Costa, F., Pritchard, M., Lara, L., Singer, B. & Herrin, J. 2014. Locating magma reservoirs using InSAR and petrology before and during the 2011–2012 Cordón Caulle silicic eruption. *Earth and Planetary Science Letters,* 395**,** 254-266.
Kamo, S. L., Czamanske, G. K., Amelin, Y., Fedorenko, V. A., Davis, D. & Trofimov, V. 2003. Rapid eruption of Siberian flood-volcanic rocks and evidence for coincidence with the Permian–Triassic boundary and mass extinction at 251 Ma. *Earth and Planetary Science Letters,* 214**,** 75-91.
Kavanagh, J., Boutelier, D. & Cruden, A. 2015. The mechanics of sill inception, propagation and growth: Experimental evidence for rapid reduction in magmatic overpressure. *Earth and Planetary Science Letters,* 421**,** 117-128.
Kavanagh, J., Menand, T. & Daniels, K. A. 2013. Gelatine as a crustal analogue: Determining elastic properties for modelling magmatic intrusions. *Tectonophysics,* 582**,** 101-111.
Kavanagh, J., Rogers, B., Boutelier, D. & Cruden, A. 2017. Controls on sill and dyke-sill hybrid geometry and propagation in the crust: The role of fracture toughness. *Tectonophysics,* 698**,** 109-120.
Kavanagh, J. L., Burns, A. J., Hazim, S. H., Wood, E., Martin, S. A., Hignett, S. & Dennis, D. J. 2018. Challenging dyke ascent models using novel laboratory experiments: Implications for reinterpreting evidence of magma ascent and volcanism. *Journal of Volcanology and Geothermal Research*.
Keating, G. N., Valentine, G. A., Krier, D. J. & Perry, F. V. 2008. Shallow plumbing systems for small-volume basaltic volcanoes. *Bulletin of Volcanology,* 70**,** 563-582.
Kennedy, B. & Stix, J. 2007. Magmatic processes associated with caldera collapse at Ossipee ring dyke, New Hampshire. *Geological Society of America Bulletin,* 119**,** 3-17.
Lanari, R., Lundgren, P. & Sansosti, E. 1998. Dynamic deformation of Etna volcano observed by satellite radar interferometry. *Geophysical Research Letters,* 25**,** 1541-1544.

Le Corvec, N., Menand, T. & Lindsay, J. 2013. Interaction of ascending magma with pre‐existing crustal fractures in monogenetic basaltic volcanism: an experimental approach. *Journal of Geophysical Research: Solid Earth,* 118**,** 968-984.
Le Corvec, N. & Walter, T. R. 2009. Volcano spreading and fault interaction influenced by rift zone intrusions: Insights from analogue experiments analyzed with digital image correlation technique. *Journal of Volcanology and Geothermal Research,* 183**,** 170-182.
Li, X., Su, L., Chung, S. L., Li, Z., Liu, Y., Song, B. & Liu, D. 2005. Formation of the Jinchuan ultramafic intrusion and the world's third largest Ni‐Cu sulfide deposit: Associated with the~ 825 Ma south China mantle plume? *Geochemistry, Geophysics, Geosystems,* 6.
Major, J., Dzurisin, D., Schilling, S. & Poland, M. P. 2009. Monitoring lava-dome growth during the 2004–2008 Mount St. Helens, Washington, eruption using oblique terrestrial photography. *Earth and Planetary Science Letters,* 286**,** 243-254.
Massonnet, D., Briole, P. & Arnaud, A. 1995. Deflation of Mount Etna monitored by spaceborne radar interferometry. *Nature,* 375**,** 567-570.
Massonnet, D., Rossi, M., Carmona, C., Adragna, F., Peltzer, G., Feigl, K. & Rabaute, T. 1993. The displacement field of the Landers earthquake mapped by radar interferometry. *Nature,* 364**,** 138-142.
Mattsson, T., Burchardt, S., Almqvist, B. S. G. & Ronchin, E. 2018. Syn-emplacement fracturing in the Sandfell laccolith, eastern Iceland–implications for rhyolite intrusion growth and volcanic hazards. *Frontiers in Earth Science,* 6**,** 5.
McTigue, D. 1987. Elastic stress and deformation near a finite spherical magma body: resolution of the point source paradox. *Journal of Geophysical Research: Solid Earth (1978–2012),* 92**,** 12931-12940.
Menand, T., Daniels, K. & Benghiat, P. 2010. Dyke propagation and sill formation in a compressive tectonic environment. *Journal of Geophysical Research: Solid Earth (1978–2012),* 115.
Mogi, K. 1958. Relations between the eruptions of various volcanoes and the deformations of the ground surfaces around them. *Bull. Earthquake Res. Inst.,* 36**,** pp. 99-134.
Montagna, C. P. & Gonnermann, H. M. 2013. Magma flow between summit and Pu ʻu ʻŌ ʻō at Kīlauea Volcano, Hawai ʻi. *Geochemistry, Geophysics, Geosystems,* 14**,** 2232-2246.
Mourgues, R., Bureau, D., Bodet, L., Gay, A. & Gressier, J. 2012. Formation of conical fractures in sedimentary basins: Experiments involving pore fluids and implications for sandstone intrusion mechanisms. *Earth and Planetary Science Letters,* 313**,** 67-78.
Nilforoushan, F., Koyi, H. A., Swantesson, J. O. & Talbot, C. J. 2008. Effect of basal friction on surface and volumetric strain in models of convergent settings measured by laser scanner. *Journal of Structural Geology,* 30**,** 366-379.
Nobile, A., Pagli, C., Keir, D., Wright, T. J., Ayele, A., Ruch, J. & Acocella, V. 2012. Dike‐fault interaction during the 2004 Dallol intrusion at the northern edge of the Erta Ale Ridge (Afar, Ethiopia). *Geophysical Research Letters,* 39.
Okada, H., Watanabe, H., Yamashita, H. & Yokoyama, I. 1981. Seismological significance of the 1977–1978 eruptions and the magma intrusion process of Usu volcano, Hokkaido. *Journal of volcanology and geothermal research,* 9**,** 311-334.
Okada, Y. 1985. Surface deformation due to shear and tensile faults in a half-space. *Bulletin of the seismological society of America,* 75**,** 1135-1154.
Pesci, A., Fabris, M., Conforti, D., Loddo, F., Baldi, P. & Anzidei, M. 2007. Integration of ground-based laser scanner and aerial digital photogrammetry for topographic modelling of Vesuvio volcano. *Journal of Volcanology and Geothermal Research,* 162**,** 123-138.
Poland, M. P., Moats, W. P. & Fink, J. H. 2008. A model for radial dike emplacement in composite cones based on observations from Summer Coon volcano, Colorado, USA. *Bulletin of Volcanology,* 70**,** 861-875.
Pollard, D. D. 1973. Derivation and evaluation of a mechanical model for sheet intrusions. *Tectonophysics,* 19**,** 233-269.
Pollard, D. D., Muller, O. H. & Dockstader, D. R. 1975. The form and growth of fingered sheet intrusions. *Geological Society of America Bulletin,* 86**,** 351-363.
Polteau, S., Mazzini, A., Galland, O., Planke, S. & Malthe-Sørenssen, A. 2008. Saucer-shaped intrusions: Occurrences, emplacement and implications. *Earth and Planetary Science Letters,* 266**,** 195-204.
Pritchard, M. E. & Simons, M. 2002. A satellite geodetic survey of large-scale deformation of volcanic centres in the central Andes. *Nature,* 418**,** 167.

Ribe, N. & Davaille, A. 2013. Dynamical similarity and density (non-) proportionality in experimental tectonics. *Tectonophysics,* 608**,** 1371-1379.
Rivalta, E., Böttinger, M. & Dahm, T. 2005. Buoyancy-driven fracture ascent: Experiments in layered gelatine. *Journal of Volcanology and Geothermal Research,* 144**,** 273-285.
Roman-Berdiel, T., Gapais, D. & Brun, J. 1995. Analogue models of laccolith formation. *Journal of Structural Geology,* 17**,** 1337-1346.
Rubin, A. M. 1993. Tensile fracture of rock at high confining pressure: implications for dike propagation. *Journal of Geophysical Research: Solid Earth (1978–2012),* 98**,** 15919-15935.
Rubin, A. M. 1995. Propagation of magma-filled cracks. *Annual Review of Earth and Planetary Sciences,* 23**,** 287-336.
Rubin, A. M. & Pollard, D. D. 1988. Dike-induced faulting in rift zones of Iceland and Afar. *Geology,* 16**,** 413-417.
Scaillet, B., Holtz, F. & Pichavant, M. 1997. Rheological properties of granitic magmas in their crystallization range. *Granite: From segregation of melt to emplacement fabrics.* Springer.
Schmiedel, T., Galland, O. & Breitkreuz, C. 2017a. Dynamics of sill and laccolith emplacement in the brittle crust: Role of host rock strength and deformation mode. *Journal of Geophysical Research: Solid Earth,* 122**,** 8860-8871.
Schmiedel, T., Kjoberg, S., Planke, S., Magee, C., Galland, O., Schofield, N., Jackson, C. A.-L. & Jerram, D. A. 2017b. Mechanisms of overburden deformation associated with the emplacement of the Tulipan sill, mid-Norwegian margin. *Interpretation,* 5**,** SK23-SK38.
Schofield, N. J., Brown, D. J., Magee, C. & Stevenson, C. T. 2012. Sill morphology and comparison of brittle and non-brittle emplacement mechanisms. *Journal of the Geological Society,* 169**,** 127-141.
Segall, P., Cervelli, P., Owen, S., Lisowski, M. & Miklius, A. 2001. Constraints on dike propagation from continuous GPS measurements. *Journal of Geophysical Research: Solid Earth,* 106**,** 19301-19317.
Sigmundsson, F., Hooper, A., Hreinsdóttir, S., Vogfjörd, K. S., Ófeigsson, B. G., Heimisson, E. R., Dumont, S., Parks, M., Spaans, K. & Gudmundsson, G. B. 2015. Segmented lateral dyke growth in a rifting event at Bar [eth] arbunga volcanic system, Iceland. *Nature,* 517**,** 191-195.
Spacapan, J. B., Galland, O., Leanza, H. A. & Planke, S. 2017. Igneous sill and finger emplacement mechanism in shale-dominated formations: a field study at Cuesta del Chihuido, Neuquén Basin, Argentina. *Journal of the Geological Society,* 174**,** 422-433.
Svensen, H., Corfu, F., Polteau, S., Hammer, Ø. & Planke, S. 2012. Rapid magma emplacement in the Karoo large igneous province. *Earth and Planetary Science Letters,* 325**,** 1-9.
Taisne, B. & Jaupart, C. 2009. Dike propagation through layered rocks. *Journal of Geophysical Research: Solid Earth,* 114.
Thun, J., Lokmer, I., Bean, C. J., Eibl, E. P., Bergsson, B. H. & Braiden, A. 2016. Micrometre-scale deformation observations reveal fundamental controls on geological rifting. *Scientific reports,* 6.
Tibaldi, A. Volcano plumbing system geometry: The result of multi-parametric effects. EGU General Assembly Conference Abstracts, 2014. 3507.
Tibaldi, A., Bonali, F. L., Pasquaré, F. A., Rust, D., Cavallo, A. & D'urso, A. 2013. Structure of regional dykes and local cone sheets in the Midhyrna-Lysuskard area, Snaefellsnes Peninsula (NW Iceland). *Bulletin of volcanology,* 75**,** 764.
Toutain, J. P., Bachelery, P., Blum, P. A., Cheminee, J. L., Delorme, H., Fontaine, L., Kowalski, P. & Taochy, P. 1992. Real time monitoring of vertical ground deformations during eruptions at Piton de la Fournaise. *Geophysical research letters,* 19**,** 553-556.
Trippanera, D., Acocella, V. & Ruch, J. 2014. Dike‐induced contraction along oceanic and continental divergent plate boundaries. *Geophysical Research Letters,* 41**,** 7098-7104.
Tryggvason, E. 1994. Surface deformation at the Krafla volcano, North Iceland, 1982–1992. *Bulletin of Volcanology,* 56**,** 98-107.
Vachon, R. & Hieronymus, C. F. 2016. Effect of host-rock rheology on dyke shape, thickness, and magma overpressure. *Geophysical Journal International***,** ggw448.
White, R. S., Drew, J., Martens, H. R., Key, J., Soosalu, H. & Jakobsdóttir, S. S. 2011. Dynamics of dyke intrusion in the mid-crust of Iceland. *Earth and Planetary Science Letters,* 304**,** 300-312.

Wiemer, S. & McNutt, S. R. 1997. Variations in the frequency‐magnitude distribution with depth in two volcanic areas: Mount St. Helens, Washington, and Mt. Spurr, Alaska. *Geophysical research letters,* 24**,** 189-192.

Yang, X. M., Davis, P. M. & Dieterich, J. H. 1988. Deformation from inflation of a dipping finite prolate spheroid in an elastic half‐space as a model for volcanic stressing. *Journal of Geophysical Research: Solid Earth,* 93**,** 4249-4257.

8. SCIENTIFIC PUBLICATIONS & MANUSCRIPTS

APPLICATION OF OPEN-SOURCE PHOTOGRAMMETRIC SOFTWARE MICMAC FOR MONITORING SURFACE DEFORMATION

I

Galland, O., H. S. Bertelsen, F. Guldstrand, L. Girod, R. F. Johannessen, F. Bjugger, S. Burchardt, and K. Mair

Journal of Geophysical Research: Solid Earth, *121*(4), 2852-2872. (2016)

https://doi.org/10.1002/2015JB012564

AGU PUBLICATIONS

JGR

Journal of Geophysical Research: Solid Earth

RESEARCH ARTICLE
10.1002/2015JB012564

Key Points:
- New quantitative monitoring method in analogue models
- Computes high-resolution and high-precision (0.04 mm) DEM and horizontal displacements
- Unexpensive, easy to set up method in the laboratory

Correspondence to:
O. Galland,
olivier.galland@geo.uio.no

Citation:
Galland, O., H. S. Bertelsen, F. Guldstrand, L. Girod, R. F. Johannessen, F. Bjugger, S. Burchardt, and K. Mair (2016), Application of open-source photogrammetric software MicMac for monitoring surface deformation in laboratory models, *J. Geophys. Res. Solid Earth*, *121*, 2852–2872, doi:10.1002/2015JB012564.

Received 28 SEP 2015
Accepted 27 FEB 2016
Accepted article online 4 MAR 2016
Published online 7 APR 2016

Application of open-source photogrammetric software MicMac for monitoring surface deformation in laboratory models

Olivier Galland[1], Håvard S. Bertelsen[1], Frank Guldstrand[1,2], Luc Girod[3], Rikke F. Johannessen[1], Fanny Bjugger[2], Steffi Burchardt[2], and Karen Mair[1]

[1]Physics of Geological Processes, Department of Geosciences, University of Oslo, Oslo, Norway, [2]Centre for Mineralogy, Petrology and Geochemistry, Department of Earth Sciences, Uppsala University, Uppsala, Sweden, [3]Department of Geosciences, University of Oslo, Oslo, Norway

Abstract Quantifying deformation is essential in modern laboratory models of geological systems. This paper presents a new laboratory monitoring method through the implementation of the open-source software MicMac, which efficiently implements photogrammetry in Structure-from-Motion algorithms. Critical evaluation is provided using results from two example laboratory geodesy scenarios: magma emplacement and strike-slip faulting. MicMac automatically processes images from synchronized cameras to compute time series of digital elevation models (DEMs) and orthorectified images of model surfaces. MicMac also implements digital image correlation to produce high-resolution displacements maps. The resolution of DEMs and displacement maps corresponds to the pixel size of the processed images. Using 24 MP cameras, the precision of DEMs and displacements is ~0.05 mm on a 40 × 40 cm surface. Processing displacement maps with Matlab® scripts allows automatic fracture mapping on the monitored surfaces. MicMac also offers the possibility to integrate 3-D models of excavated structures with the corresponding surface deformation data. The high resolution and high precision of MicMac results and the ability to generate virtual 3-D models of complex structures make it a very promising tool for quantitative monitoring in laboratory models of geological systems.

1. Introduction

Since the introduction of the scaling theory by *Hubbert* [1937], the physical analysis of laboratory models of geological systems has been based on visual observations with limited resolution and precision [e.g., *Acocella et al*., 2001; *Lickorish et al*., 2002; *Donnadieu et al*., 2003; *Fort et al*., 2004]. Consequently, such a qualitative laboratory approach has become overlooked compared to numerical models, from which quantitative information (such as stress and strain) can be extracted.

The last decade, however, witnessed a quantitative revolution in laboratory modeling with the introduction of modern monitoring techniques [*Leever et al*., 2014]. Good examples are (1) digital image correlation (DIC, implemented as particle image velocimetry (PIV) for flow measurements) [e.g., *White et al*., 2003; *Sveen*, 2004], which computes displacement maps from time series of photographs of a moving surface [e.g., *Adam et al*., 2005; *Rosenau et al*., 2010; *Abdelmalak et al*., 2012]; (2) lasers that measure the topography of a surface [e.g., *Lague et al*., 2003; *Sokoutis and Willingshofer*, 2011]; and (3) systems based on structured light, also designed to measure topography [e.g., *Brèque et al*., 2004; *Babault et al*., 2007; *Galland*, 2012].

Each of the existing methods used to quantify results in laboratory models has its advantages and disadvantages (see review in section 2). Some methods only measure the topography (e.g., laser and structured light), while others compute only in-plane displacements (DIC). In addition, high-resolution/high-precision systems are usually expensive (and hence unaffordable for many laboratories), while less expensive systems produce low-resolution and/or low-precision data. Finally, with the exception of X-ray computed tomography (XCT) scanners, existing methods are limited to monitoring surfaces (model surfaces or model sidewalls), meaning that the models' internal structures cannot be imaged quantitatively.

The purpose of this paper is to present a method for quantitative monitoring of laboratory models that combines the following advantages: (1) it is relatively inexpensive, since it is based on the free open-source software MicMac; (2) it measures both topography, topography changes, and horizontal displacements in the same workflow; (3) the results are high resolution and high precision, i.e., 0.1 mm and 0.04 mm, respectively,

for a 40 cm wide system using 24 MP cameras; (4) it is straightforward to set up in the laboratory as it does not require complex calibration; and (5) it can be used both to monitor the surface evolution of the models and to image internal structures of the models after the end of the experiment.

In the following section, we briefly review the existing methods used to quantitatively monitor laboratory models and list their advantages and disadvantages. We subsequently present the principles behind MicMac and expand its implementation. Subsequently, we introduce the relevance of MicMac and its output data using two laboratory model examples: (1) magma emplacement in the brittle crust and (2) strike-slip tectonics. In the discussion, we quantify the precision of the results produced by MicMac and discuss its versatility in various laboratory studies.

2. Existing Monitoring Techniques

The methods listed below are grouped according to the types of data they produce, e.g., digital elevation models (DEMs) and in-plane displacements.

2.1. Topography Measurements

Many geological processes induce topography or topographical change, e.g., tectonic movements, erosional processes, and magma intrusion in the shallow crust. Such changes are monitored using ground-based (GPS, clinometers, and laser) and remote sensing (interferometry radar) techniques. Laboratory models designed to investigate these processes must therefore also produce topographical changes.

Topography measurements using lasers have been used in, e.g., geomorphology [e.g., *Lague et al*., 2003] and tectonics experiments [e.g., *Martinod and Davy*, 1994; *Sokoutis and Willingshofer*, 2011; *Farzipour-Saein et al*., 2013]. The laser method used by *Lague et al*. [2003] produced precise DEMs, but the acquisition time was long (hours), meaning that dynamic experiments had to be artificially stopped during the acquisition. Modern laser systems, such as those used by *Sokoutis and Willingshofer* [2011] and *Farzipour-Saein et al*. [2013], allow much faster acquisitions; however, this equipment is expensive and still not suitable for fast experiments, i.e., experiments that last for a few minutes at maximum.

Several methods for measuring topography use optical techniques based on structured light (also called moiré projection) [*Brèque et al*., 2004]. The principle is to project a pattern (typically straight black and white fringes) onto the surface to be measured. The monitored fringe pattern is then digitally analyzed to build a DEM of the surface. This method has been used extensively in laboratory models of geomorphology [e.g., *Babault et al*., 2005; *Babault et al*., 2007], tectonics [e.g., *Grujic et al*., 2002; *Graveleau and Dominguez*, 2008; *Graveleau et al*., 2012] and magma intrusions [e.g., *Galland et al*., 2009; *Galland*, 2012]. This technique can provide good temporal resolution; however, the spatial resolution is somewhat limited due to the width of the fringes. In addition, some available commercial software and equipment packages represent substantial costs, while noncommercial systems require substantial development.

Recently, *Tortini et al*. [2014] adapted the low-cost Microsoft® Kinect system (used in video games) to measure surface topography in models. This system is inexpensive; however, the spatial resolution and vertical precision of the DEMs are (much) lower than those produced by laser systems or structured light techniques.

The methods described above have been used to measure the topography of simple surfaces. Another optical method, described by *Cecchi et al*. [2003], has been implemented to reconstruct complex shapes, like a steep volcanic edifice. It is based on series of photographs taken around an object (N-view reconstruction). The principle is similar to the method presented in this paper, i.e., reconstructing the morphology of an object from a set of images using a multiview calibration method based on bundle adjustments [*Beyer*, 1992b]. In this method, both the camera calibration and the positions of the viewpoints are computed, which considerably simplifies and shortens the laboratory preparation procedure. Although this method appears promising and produces high-resolution results, it has surprisingly rarely been used in the laboratory.

All the techniques described above produce DEMs of the model surfaces. One obvious disadvantage, however, is that DEMs alone do not allow separation of the vertical and horizontal movements. In addition, subsurface structures are not accessible and therefore cannot be monitored.

2.2. In-Plane Displacements Measurements

In some geological processes (e.g., strike-slip faulting), in-plane displacements, i.e., displacements parallel to the observed surface, are large compared to the topographic changes. A simple method for quantifying such in-plane displacements in laboratory models is digital image correlation (DIC) using a camera fixed vertically above the model. DIC is used to compare images of different time steps and compute in-plane displacement maps. This technique has produced excellent results, e.g., in characterizing the complex deformation pattern associated with strike-slip and transpressional deformation [e.g., *Leever et al*., 2011] and the subsurface structure development during caldera collapse [e.g., *Burchardt and Walter*, 2010]. DIC usually requires relatively inexpensive equipment (a digital camera) [*Donnadieu et al*., 2003; *Delcamp et al*., 2008; *Leever et al*., 2011; *Abdelmalak et al*., 2012]; however, some commercial packages are very expensive (LaVision packages, used by, e.g., *Burchardt and Walter* [2010], *Haug et al*. [2014], and *Byrne et al*. [2015]). Several DIC programs are free, such as MatPIV for Matlab® [*Sveen*, 2004]; others require a commercial program, such as COSI-Corr [*Leprince et al*., 2007], which is integrated with ENVI.

DIC can also be used to monitor deformation within pseudo-2-D models when the sidewalls are transparent [e.g., *Holland et al*., 2006; *Rosenau et al*., 2010; *Abdelmalak et al*., 2012]. Boundary effects, however, can be quite prominent on the structure development in this geometry, but these effects have not been quantified.

DIC has also been used in 3-D experiments made of transparent materials (gels) containing tracers lighted up by a laser sheet [*Kavanagh et al*., 2015]. Even if the experiments are 3-D, the tracers are only visible on the 2-D plane of the laser sheet; therefore, the DIC results are 2-D only, and out-of-plane movements are not measured/corrected.

The time and spatial resolutions of DIC results depend mainly on the resolution of the cameras used and their frame rate. In addition, optical distortion, if not corrected, can lead to substantial measurement errors. In addition, large topography in the models can lead to significant distortion on images of the model surface taken from above, especially where subvertical features are involved, such as fault scarps.

2.3. Three-Dimensional Surface Displacements

Stereophotogrammetry is a common method for computing 3-D surface displacements of laboratory model surfaces. *Donnadieu et al*. [2003] describe how stereophotogrammetry was applied to measure both topography change and horizontal displacements. Their results, however, were of low spatial resolution. *Delcamp et al*. [2008] also used stereophotogrammetry to compute the vertical and horizontal displacement fields associated with volcano collapse similarly to the method of *Donnadieu et al*. [2003].

Adam et al. [2005] and *Reiter et al*. [2011] produced 3-D displacement maps of tectonic models using a commercial package (LaVision). Even if such package is robust and produces results with good resolution and precision, the price of it is prohibitive for most laboratories.

More recently, *Trippanera et al*. [2014] combined laser methods and DIC to compute topography change and horizontal displacements, respectively. Although such a combination produces 3-D displacement maps of the model surface, the inherent limitations of each separate method persist (see above). In addition, linking laser and DIC data sets is not trivial.

2.4. XCT Scanner

XCT scanners have been used to monitor internal deformation in laboratory models, both by means of (2-D) snapshots during model deformation [e.g., *Schreurs and Colletta*, 1998] and recently also as the basis of 3-D image correlation [*Adam et al*., 2013]. Even if this newest application is promising and provides spectacular images of 3-D displacement fields, there are severe limitations. (1) XCT scanners are very expensive. (2) The spatial and temporal resolution is usually quite low compared to optical methods [*Adam et al*., 2013]. (3) The size of the models that can be imaged is often limited by the size of the scanner [*Poppe et al*., 2015]. (4) Scanners produce immense data sets that are challenging to store and whose analysis generally requires the use of expensive software [*Adam et al*., 2013; *Lawson and Dawson*, 2014].

2.5. Summary

Although a number of methods exist to quantitatively monitor laboratory experiments of geological systems, none of them combines the following advantages: low cost, high resolution, high precision, both topography change and horizontal displacements, and ease of setup in the laboratory. Moreover, with the exception of

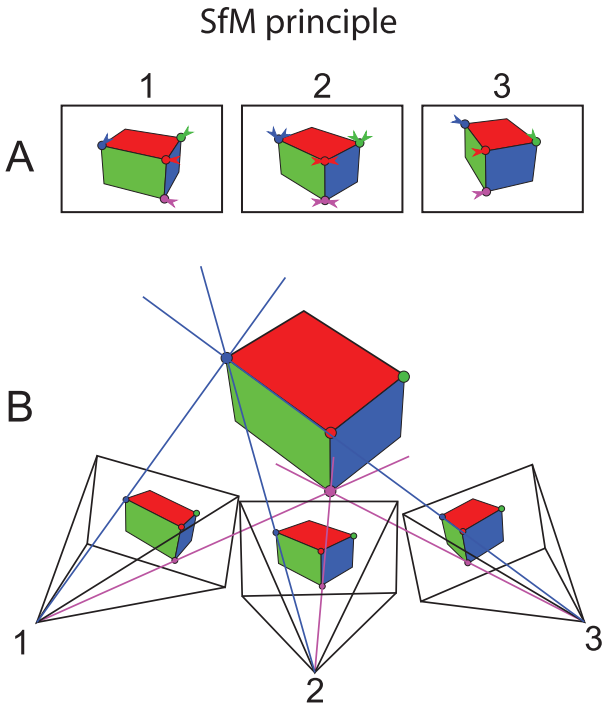

Figure 1. Schematic drawing illustrating the two main steps in SfM. (a) Step 1. Schematic set of photographs of the same object taken from different viewpoints (1, 2, and 3). A computer vision algorithm finds homologous "feature" points in each image and subsequently finds those that are homologous, i.e., the pixels in the images that correspond to the same points of the photographed object (here for simplicity, only the colored corners of the object). Due to the different viewpoints, these homologous points, defined as tie points, have different positions in the images. (b) Step 2. The SfM algorithm uses the different positions of the homologous feature points in the images to compute the relative position of the camera for each picture.

expensive XCT scanners, none of these techniques have successfully integrated (1) surface deformation with (2) the underlying structures after the end of the experiments. In this paper, we describe a method that combines these advantages.

3. Method: MicMac Photogrammetric Open-Source Package

3.1. The MicMac Workflow

Modern photogrammetry methods aim to reconstruct 3-D digital models of objects from a collection of images. The concept of reconstructing topography or depth using pairs of images was first introduced by photographers and engineers in the middle eighteenth century (the word photogrammetry was first used by *Meydenbauer* [1867]); however, it was the automation of the process through what is known as Structure from Motion (SfM) that made it so popular in a wide range of applications. The main concepts where laid out by *Koenderink and van Doorn* [1991] and later shaped into a highly efficient software by *Snavely et al.* [2006, 2008]. Modern application to geoscience was introduced by *Westoby et al.* [2012] and *Bretar et al.* [2013], among others.

The principle of SfM consists of two successive steps. The first step (Figure 1a) corresponds to detection and matching of automatic tie points (e.g., using an algorithm such as SIFT by *Lowe* [2004] or more recently SURF by *Bay et al.* [2006] or ASIFT by *Morel and Yu* [2009]). A tie point is a point that has ground coordinates that are not known but is recognizable in at least two images due to local features in the overlap area between the images. This means that pixels displaying strong local contrast (known as feature points) are detected and described, and feature points from different images with similar descriptors are automatically identified and therefore constitute tie points. The second step (Figure 1b) corresponds to bundle adjustment [*Beyer*, 1992a] where the relative locations of viewpoints (camera positions) are computed. The result of this second step is then used to reconstruct the final 3-D model of the photographed object using image correlation. This procedure makes the process extremely fast and efficient compared to analytical photogrammetry and manual interpretation. Note that large numbers of feature points provide better results for the bundle adjustment calculation. Therefore, the photographed objects must have a visible and prominent texture.

In this study, we use the versatile and accurate software MicMac [*Pierrot-Deseilligny et al.*, 2015a, 2015b] that powerfully implements photogrammetry in SfM algorithms. MicMac has been developed at the French Geographical Institute. MicMac is an acronym for "Multi Images Correspondances par Méthodes Automatiques de Corrélation." It is free open-source software distributed under the CeCILL-B license. The suitability of MicMac for laboratory models of geological processes has initially been tested by *Girod* [2012].

The main steps of the photogrammetric workflow (visualized in Figure 1) using MicMac are the following (the names of the commands in MicMac are mentioned in *[ ]* and their use described in the online documentation (available at the bottom of the page http://logiciels.ign.fr/?Telechargement,20)):

1. Several pictures (Figure 1a) of the same object (colored rectangular cuboid) are acquired from slightly different positions (Figure 1b).
2. All images are analyzed (*Tapioca/Pastis*) to compute tie points. Tie points are SIFT feature points [*Lowe*, 2004] that are common to, at least, two of the processed images (for example the colored dots in Figure 1a). In order to detect tie points, the images should have local patterns/contrasts of minimum size of a few pixels. A tie point is defined as a negative or positive peak in brightness intensity: continuous gradients or small amplitude peaks would not yield tie points [*Rosu et al*., 2015a]. Therefore, the combined camera resolution/size of features on the model surface should lead to sharp, prominent features in the processed images.
3. The tie points are used to compute automatically both the camera positions and viewing angle, and the distortion model of the cameras' optics (*Tapas/Apero*).
4. Ground control points (GCPs) are used to scale, orientate, and/or register the model in the desired geometry (*GCPBascule*). GCPs are points of (or in the vicinity of) the recorded object with known/measured positions. In our experiments, we use the corners of the box as GCPs. In general, the GCPs do not need to correspond with tie points. A minimum of three GCPs visible on at least three images is necessary for this georeferencing.
5. Using this information, a high-resolution reconstruction is performed through image correlation, yielding a depth map, i.e., a DEM (Malt/MICMAC). Points are computed on a regular grid of the interest area, regardless of the positions of the tie points calculated with Tapioca. The spatial resolution of the DEM will be close to that of the processed images. The image correlation requires that the processed images of the model surface do not display homogeneous pixel patches bigger than the correlation window, which defines the template for which correlation is computed for the templates corresponding to each pixel of the search window. The prominent features used for computing tie points are obviously relevant, as well as smoother features such as gradients.
6. Based on camera positions, camera calibration, and the DEM computed in the previous step, an orthorectified image is then produced (*Tawny*). An orthorectified image is a geometrically corrected ("orthorectified") photograph such that the scale is uniform: the photo has the same lack of distortion as a map. Unlike a normal photograph, an orthorectified image can be used to measure true horizontal distances, because it is an accurate representation of the photographed surface, having been adjusted for topographic relief, lens distortion, and camera tilt.
7. The DEM and orthorectified image are integrated, which allows computation of a high-density point cloud (*Nuage2Ply*).
8. Using orthorectified images of a deforming object at different times, high-quality DIC is then used to compute subpixel, high-resolution in-plane displacement maps at the surface of deforming objects [*Rosu et al*., 2015b] (*MM2DPosSism*). Every pixel of the image is systematically tracked, regardless of the prominence of the local pattern of pixels; the correlation would fail in the absence of this feature. Patterns seen in the images are not the tie points calculated from Tapioca.

MicMac offers the advantages of (1) a simple camera calibration procedure in the laboratory as it automatically calculates the camera calibration parameters and the camera positions, (2) fast photogrammetric computing, and (3) high-resolution and high-precision DEMs and orthorectified images of the photographed objects. A similar workflow can be used to image the internal structure of 3-D models.

The following subsection describes details of the workflow to implement MicMac in the laboratory.

3.2. Implementation in the Laboratory

The implementation of MicMac in laboratory models follows three successive steps: (1) image acquisition, (2) image processing, and (3) data analysis. Importantly, the implementation of each step is independent of the other steps.

Image acquisition. In order to produce DEMs, orthorectified images, and high-density point clouds of the surveyed model surface, it is necessary to have several images of it. In the case of an evolving surface, synchronized cameras are required to shoot photographs of the model surface synchronously. In our laboratory, we used four standard DSLR (digital single-lens reflex) cameras (Nikon D3200, lens Nikkor 35 mm), at a shooting frequency of 1 Hz. The lens parameters of the four cameras should be identical, and therefore, it is recommendable to use fixed lenses. The angles between the cameras should be 10–15°. To ensure that the

images from the four cameras are sharp, the cameras are placed at a relatively similar distance from the model surface. In our setup, the camera shooting is computer controlled and triggered by a LabView program via an infrared remote control. In theory, two cameras are necessary to implement MicMac, but the level of precision is better from four cameras. For surfaces more complex than our flat surfaces, more synchronized cameras might be needed to sample the topographic complexity. Synchronized video cameras, and even synchronized fast cameras, could also be used to monitor fast-evolving surfaces. The results of step 1 are sets of N images for each acquisition time, N being the number of synchronized cameras.

Image processing. Using MicMac does not require entering into the software code. The level of abstraction is quite high, even if there is no graphical user interface. The principle is to call MicMac functions in a terminal window (see list of functions in section 3.1), and the user specifies options and parameters for each function. The successive calls of functions can be grouped in shell scripts. All times of an experiment can then be automatically processed. The products of each time are (1) a DEM given in tagged image file format (TIFF), (2) an orthorectified image in TIFF, and (3) a high-density point cloud in polygon (PLY) format. The user can choose to run the DIC function MM2DPosSism (see section 3.1) between (i) the orthorectified image of each time and the orthorectified image of the initial surface to compute total in-plane displacement maps or/and (ii) the orthorectified images of successive times to compute incremental in-plane displacement maps. These displacement maps are also in TIFF format.

Data analysis. The TIFF format of the data produced from MicMac is very standard and can be loaded using many different data analysis programs, such as Python, Matlab®, Surfer®, and ENVI. We used Matlab®, which contains built-in functions to calculate automatically, for example, the divergence and shear strain maps of a vector field. Note as well that DEM differences and in-plane displacement maps can be calculated between different times: this data set allows computing the 3-D displacement field of the surveyed surface.

Among these three steps, only step 2 implements photogrammetry. However, the quality of the photogrammetric calculations relies on the laboratory workflow of step 1. The fact that the implementation of these three steps is independent of each other implies that the full workflow is very versatile and can be adapted to various laboratory approaches.

The following section describes two different applications of MicMac in laboratory experiments of (1) magma emplacement in the crust and (2) tectonic deformation.

4. Laboratory Applications

4.1. Magma Emplacement in a Brittle Crust

4.1.1. Experimental Setup

In this section we present characteristic laboratory results of surface deformation induced by shallow magma emplacement [see, e.g., *Galland et al*., 2009; *Galland*, 2012; *Galland et al*., 2014]. The experimental setup (Figure 2a) consists of a box filled with model crust and an oil injection system monitored from above by four synchronized cameras. We used fine-grained crystalline silica flour as an analogue for the brittle crust and a low-viscosity vegetable oil for the magma, which is injected to simulate magma emplacement. The grain size of the flour is ~15 μm. It fails according to a Mohr-Coulomb criterion, and its cohesion and friction coefficient are 369 ± 44 Pa and 0.81 ± 0.06, respectively [*Galland et al*., 2009]. This yields an angle of internal friction of ~39°. The tensile strength T of the flour is ~100 Pa [*Galland et al*., 2006]. The vegetable oil is produced by Unilever and sold in France under the name Végétaline. It is solid at room temperature but melts at ~31°C. The viscosity of the oil is poorly temperature dependent [*Galland et al*., 2006], and we injected it at ~50°C where its viscosity is $\sim 2 \times 10^{-2}$ Pa s.

As this study focuses on the application of MicMac rather than the physical meaning of the experiments, we do not develop and discuss the scaling of the modeled processes here. For a description of the scaling and relevance of the model materials, the reader is referred to *Galland et al*. [2006, 2014]; *Galland* [2012] and *Galerne et al*. [2011].

Our apparatus is a modified version of that developed by *Galland et al*. [2006, 2009, 2014] and *Galland* [2012]. The model was placed in a square box, 40 cm wide (Figure 2). The preparation procedure consisted of measuring a mass of flour, which was compacted using a high-frequency compressed-air shaker (Houston Vibrator model GT-25). Such procedure allowed a homogeneous, repeatable, and fast compaction of the flour to reach a prescribed density. To track surface deformation, we sieved powdered coffee grains, the size of

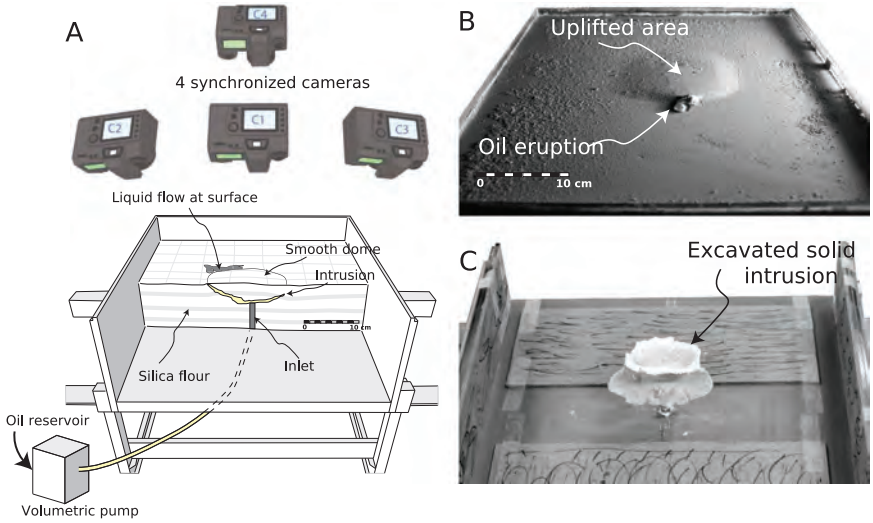

Figure 2. (a) Diagram showing the experimental apparatus used for volcano geodesy (see text for explanations). Four cameras positioned above the model monitor the surface. (b) Representative oblique view photograph of the model surface during an experiment. The surface exhibited a smooth dome, at the rim of which the oil erupted. The model surfaces are sprinkled with coffee grains (not visible on this photograph) to provide a random pattern for image analysis. (c) Representative oblique view photograph of an excavated solidified intrusion. As it is fully excavated, it is possible to apply photogrammetry and compute its 3-D shape.

which is <1 mm, on the model surface to create a dense random texture (Figure 3a). These grains are prominent features for computing tie points on the model surface with Tapioca (see section 3.1). These features are likely used for image correlation calculations using Malt and MM2DPosSism functions, in addition to other features that are not selected as feature points by Tapioca (e.g., gradients and low-amplitude brightness peaks).

The "magma" oil was injected through a circular inlet into the model "crust." *Galland et al*. [2006, 2007, 2009] showed that the shallow emplacement of magma triggered deformation of the surface of the models, producing a smooth dome (Figure 2b). During oil injection, four synchronous computer-controlled standard DSLR cameras (model Nikon D3200, lens Nikkor 35 mm) placed at different angles (Figure 2a) took photographs of the model surface at a frequency of 1 Hz. The camera shooting was computer triggered using infrared remotes activated by an in-house LabView® program.

Each experiment typically lasted for a minute or less. After the end of the experiments, the oil solidified within half an hour. After solidification, the intrusion was fully excavated (Figure 2c). We then took photographs from many different angles following a robust procedure to compute the 3-D shape of the intrusion (see section 4.1.3).

4.1.2. Model Surface Monitoring

For each time step of the models, we processed the four synchronous images taken by the four cameras with MicMac to produce a high-resolution DEM (section 3.2 and Figure 3a) and an orthorectified image (Figure 3b). The advantage of the orthorectified images is that they are very accurate representations of the model surface because they have been corrected for topographic relief, optical distortion of the lens, and camera tilt. Thus, the orthorectified images are equivalent to georeferenced maps and can be used to measure distances and angles.

Once the DEMs and orthorectified images are computed, the Nuage2Ply command combines them to produce high-density point clouds (Figure 3c). The main use of the point clouds is for 3-D display, whereas the DEMs and orthorectified images are more useful for quantitative data analysis.

Each DEM and orthorectified image corresponds to a static snapshot of the model surface at a given time. In the experiments, we monitor the evolution of the model surfaces at constant time intervals of $\Delta t = 1$ s. Thus, computing the DEMs and orthorectified images regularly through time allows to quantitatively analyze the model surface evolution. In Figure 4, we present DEM difference, i.e., the difference between the final and

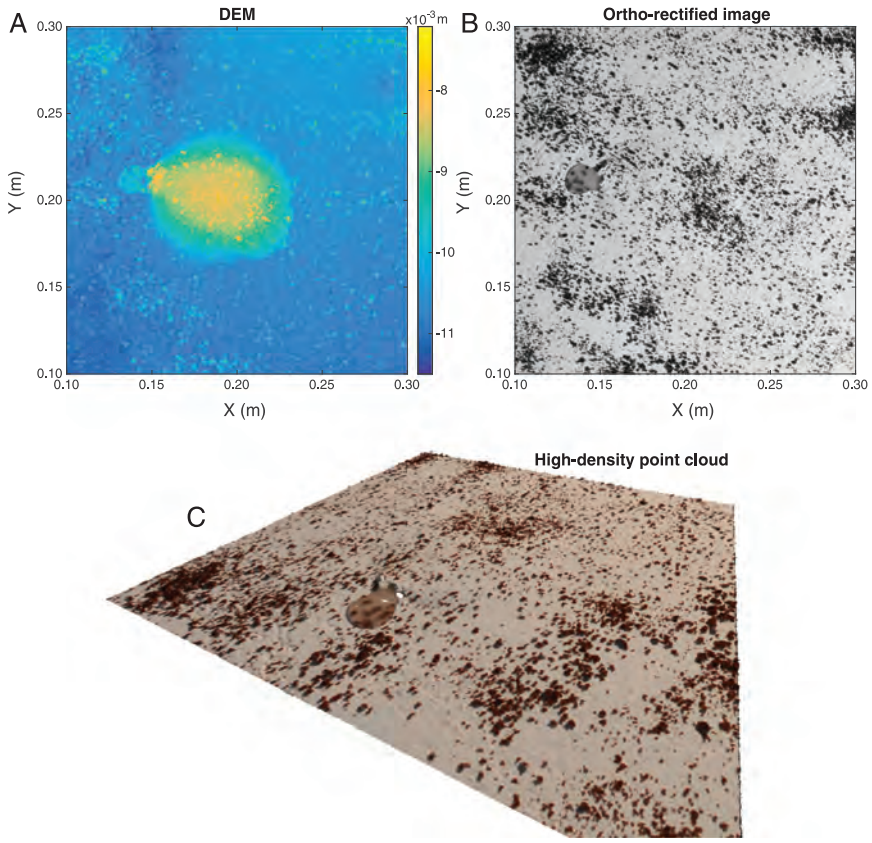

Figure 3. (a) Plot of a representative DEM of a model surface. The oil erupts at the left edge of a smooth dome. The origin elevation of the DEM is the corners of the walls of the experimental box. Notice the black coffee grains that produce a random texture on the model surface. (b) Plot of a representative georeferenced orthorectified image of a model surface. The DEM automatically covers the same area as that of the orthorectified image. Note also the roughness produced by the coffee grains (~1 mm). (c) Oblique view of a representative high-density 3-D point cloud of a model surface. The point cloud is a combination of the DEM (Figure 3a) and the orthorectified image (Figure 3b) and is useful for 3-D visualization.

initial DEM, as well as horizontal displacement maps calculated from orthorectified images. One needs to be aware that DEM difference does not correspond to a map of vertical displacements only, as topography changes can also be the result of horizontal movements.

A visual comparison between orthorectified images obtained at different times reveals horizontal displacements of the model surface. These displacements can be quantified using the MicMac command MM2DPosSism, which computes high-resolution DIC between two orthorectified images [*Rosu et al.*, 2015b]. The correlation computes subpixel (1/10 pixel) displacements, and the resolution of the computed vector fields is the same as the original orthorectified images. This MicMac command has been designed to detect and highlight sharp displacement discontinuities, such as map traces of active faults [*Rosu et al.*, 2015b; *Vallage et al.*, 2015].

In our experiments, the DIC analysis can be performed (1) between an orthorectified image of a given time and the orthorectified image of the initial time, which calculates the total displacement maps, or (2) between orthorectified images of two successive times, which calculates incremental displacement maps. The correlation window used in our study for the DIC was 9 pixels, i.e., $<$1 mm. This implies that we are able to calculate only small ($<$1 mm) displacements. To be able to calculate larger displacements, one can increase the size of the correlation window, but this leads to lower resolution of the results. Figure 4 displays a representative example of displacement maps of the model surface during a characteristic magma intrusion experiment.

Visual observation of orthorectified images highlights the formation of surface discontinuities, i.e., fractures (Figure 5a; see qualitative fracture interpretation in Figure 5b). In the middle of the uplifted area, a few open,

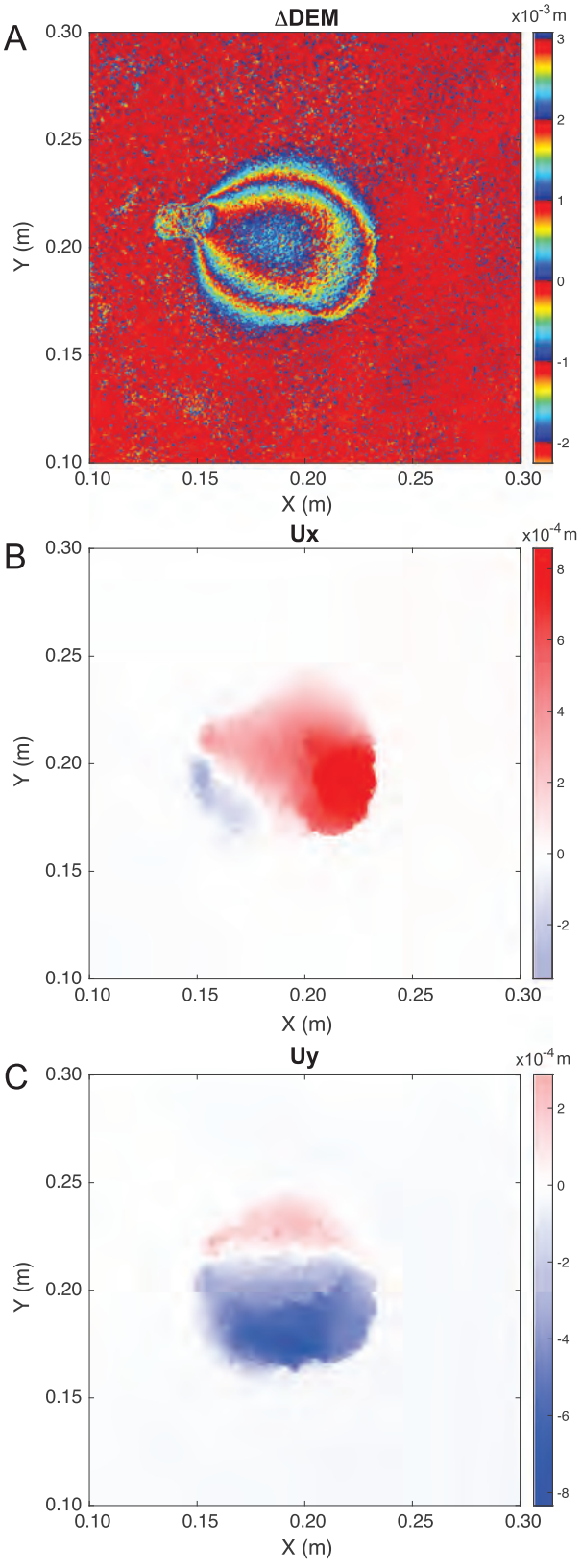

dilating cracks are clearly visible, while at the edges of the uplifted area fractures accommodating shortening are visible (Figure 5b). Such a fracture pattern is compatible with stress distribution across a dome induced by a shallow intrusion [e.g., *Pollard and Johnson*, 1973; *Galland and Scheibert*, 2013]. Displacement maps calculated automatically from DIC analysis highlight clear discontinuities (Figures 5c and 5d) coinciding with the visible surface fractures (Figure 5b). A simple method to highlight surface fractures is to compute the divergence and the shear strain fields from the displacement maps using, e.g., straightforward Matlab® scripts. Figures 5e and 5f display the divergence and shear strain fields computed from the displacement maps of Figures 5c and 5d. They clearly highlight the presence of numerous cracks, the majority of which are too small to be visually observed on the orthorectified image of Figure 5b. The divergence field nicely images opening cracks (positive divergence) in the uplifted area and the shortening fractures (negative divergence) at the edge of the uplifted area. Notice that the divergence values are higher than those of the shear strains (Figures 5e and 5f), which is intuitive given that stresses generated by surface doming are expected to be dominantly tensional or compressional [e.g., *Pollard and Johnson*, 1973; *Galland and Scheibert*, 2013].

Figure 4. (a) Plot of a characteristic DEM difference (ΔDEM) between the final state and the initial state of the model displayed in Figure 3. The data corresponding to the solidified oil that flowed at the model surface (left of uplifted area) is very noisy due to the fact that the oil is partly transparent (see coffee grains below oil in Figure 3a). Note that DEM difference is not uplift, as DEM accounts for horizontal displacements as well. (b) Plot of a representative horizontal displacement map parallel to *x* axis (U_x) between the final state and the initial state of the model as in Figure 4 a (but calculated from the orthorectified image). (c) Plot of a representative horizontal displacement map parallel to *y* axis (U_y) between the final state and the initial state of the model as in Figure 4a (but calculated from the orthorectified image).

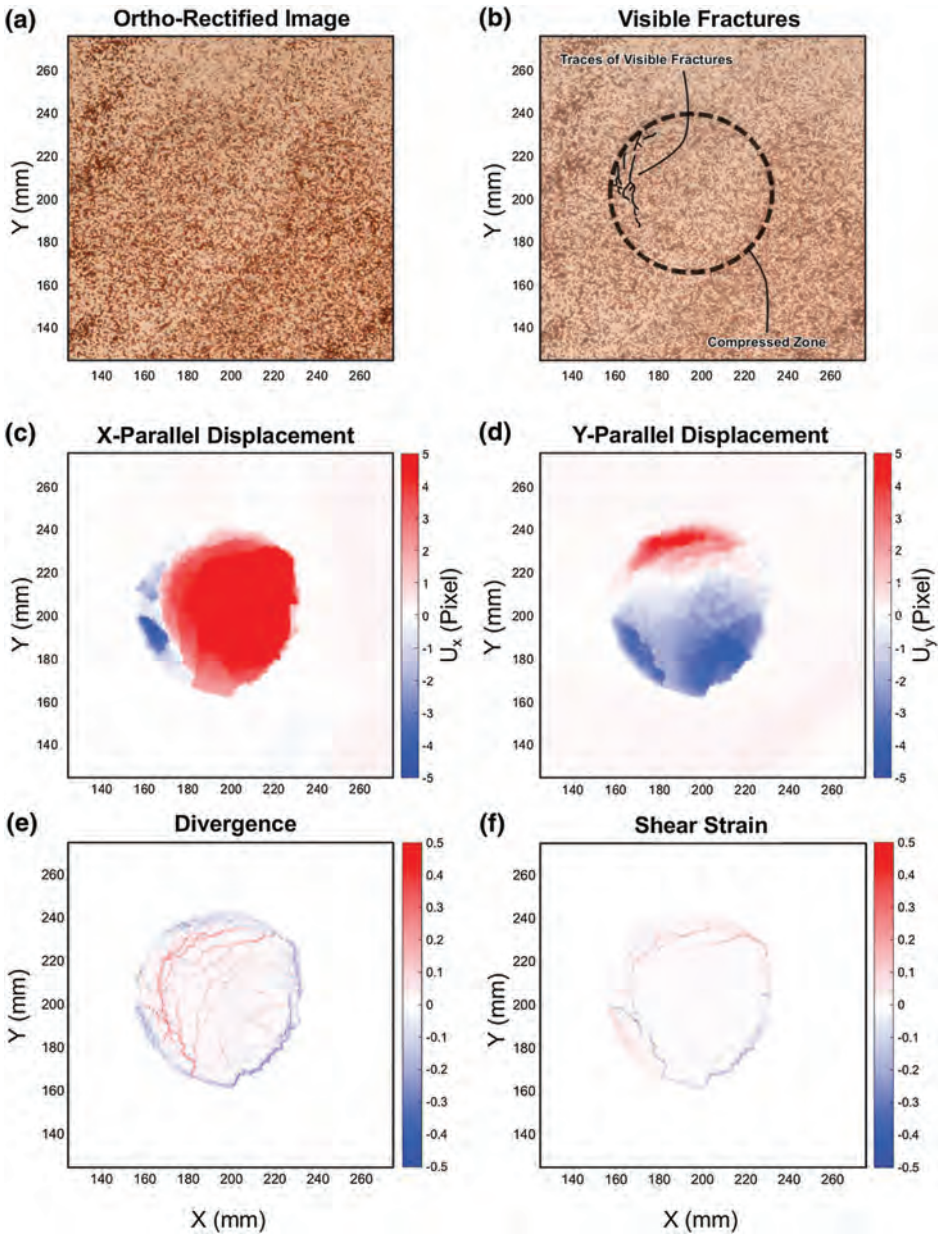

Figure 5. (a) Orthorectified image of the surface of an example experiment that simulated the emplacement of a cone sheet, just before oil eruption. The random pattern is made of coffee grains sieved onto the surface of the model. It is possible to observe a subcircular feature in the central part of the image. (b) Same orthorectified image (with light exposure increase) as in Figure 5a with tensional fractures observed visually on the image indicated by black lines. Dashed lines outline of the uplifted area, the edge of which corresponds to contractional fractures. (c) Map of U_x (displacements parallel to *x* axis) computed from image correlation between the orthorectified image of the model surface before injection and the orthorectified image computed for the initial state of the model (not shown). (d) Map of U_y (displacements parallel to *y* axis) computed from image correlation between the orthorectified image of the model surface before injection and the orthorectified image of Figure 5a. (e) Map of divergence computed from U_x and U_y maps in Figures 5c and 5d. Positive divergence (red) means dilation, while negative divergence (blue) means contraction. The map highlights a complex fracture pattern, which was not visible on the orthorectified image of Figure 5a. (f) Map of shear strain computed from U_x and U_y maps of Figures 5c and 5d.

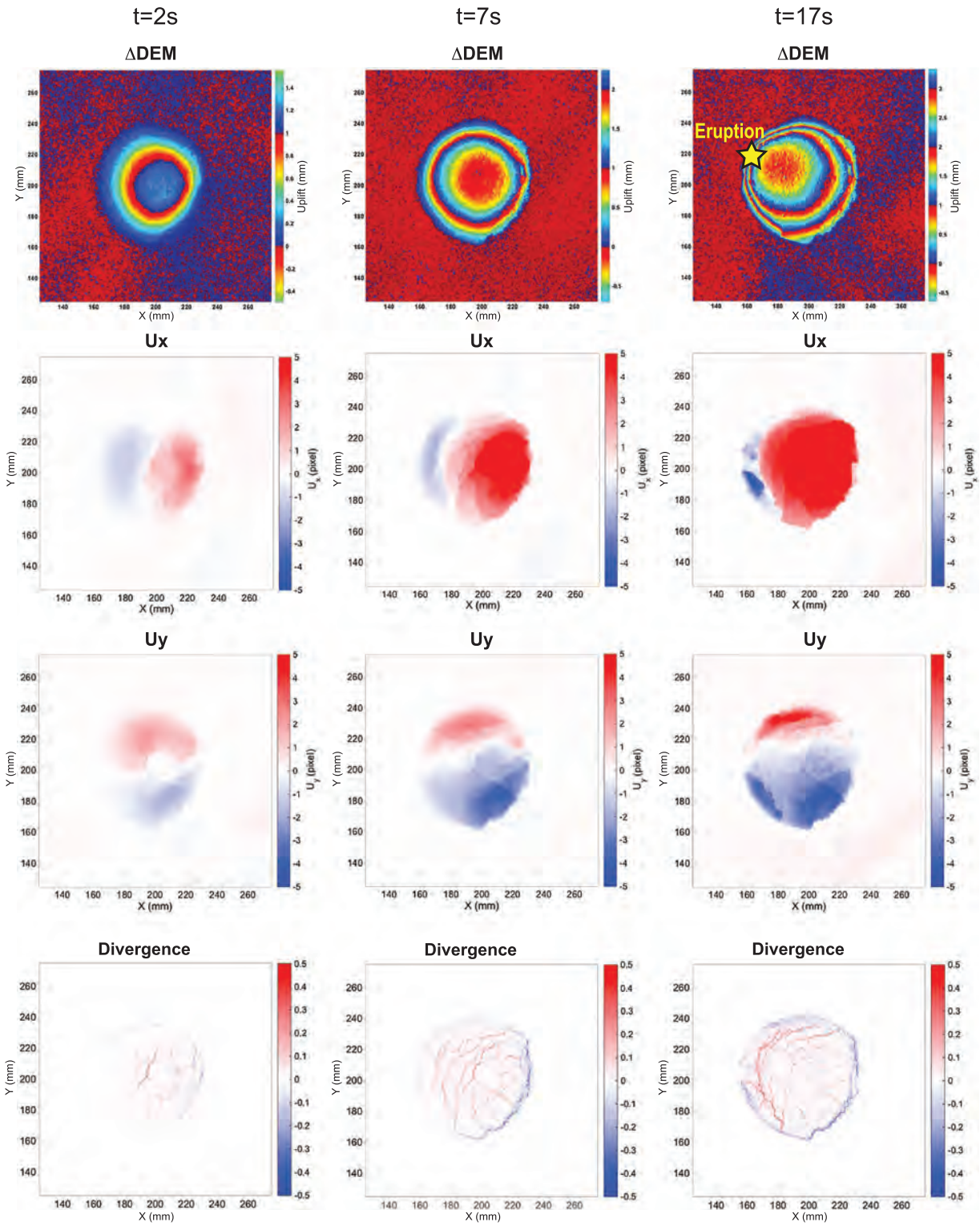

Figure 6. Plots of representative results of the surface evolution during an example magma intrusion experiment (left, middle, and right columns) at three distinct time steps. The plots display ΔDEM (topography change with respect to initial state), U_x (surface displacements parallel to the *x* axis), U_y (surface displacements parallel to the *y* axis), and divergence field calculated from U_x and U_y field. The yellow star locates oil eruption.

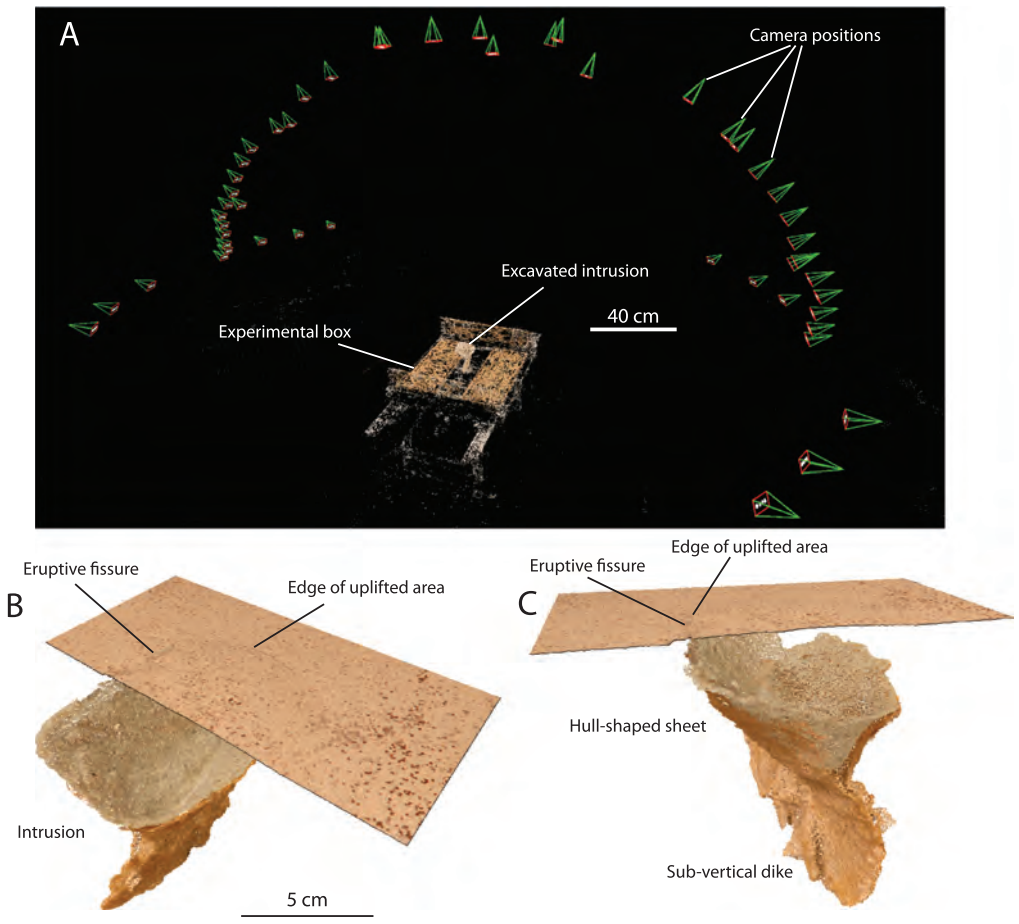

Figure 7. (a) Snapshot image of low-density point cloud illustrating the photographing setup for SfM modeling of a solidified excavated intrusion (point cloud produced with MicMac's AperiCloud command). (b and c) Two representative views of high-density point clouds of part of the model surface after the end of the experiment and the underlying solidified excavated intrusion. Notice the good correspondence between the edge of the uplifted area and the location of the eruptive fissure (recall Figure 2b).

The periodic monitoring of the experiments allows one to analyze the evolution of the model surfaces by highlighting incremental deformation (Figure 6). Early in the experiments (Figure 6, left column), the uplifted area has a symmetrical shape. The horizontal displacement patterns are also symmetrical, the "neutral" zones (i.e., the zone with zero displacements between the areas of opposite displacements) being lines at the center of the uplifted area. In addition, the divergence plot indicates dilation, i.e., open tensile fractures in a radial pattern. In the later stages (Figure 6, middle and right columns), however, a clear asymmetry develops: the point of maximum uplift and the neutral zone for the *x* displacements move to the left. The tensile fracture pattern (shown on the divergence plot) also gradually changes from a radial pattern to a dominantly circumferential pattern.

4.1.3. Model Surface Data Versus Internal Structure

A great advantage of SfM is the possibility to compute 3-D models of objects of complex shapes, such as buildings and archeological objects [*Pierrot-Deseilligny et al.*, 2015a]. We therefore established a procedure to calculate 3-D models of the solidified intrusions after excavating them; this is possible because the solidified oil is rigid enough to stay in place without collapsing (Figures 2c and 7). Because the intrusions are static objects, moving only one camera around the intrusion was necessary. However, the complex shapes of excavated intrusions require more photographs (here about 50; Figure 7a) to be taken than for the model surface.

We implemented the MicMac workflow described above, including the georeferencing using the corners of the box as GCPs. Consequently, the data of the model surface and of the underlying intrusion are defined in

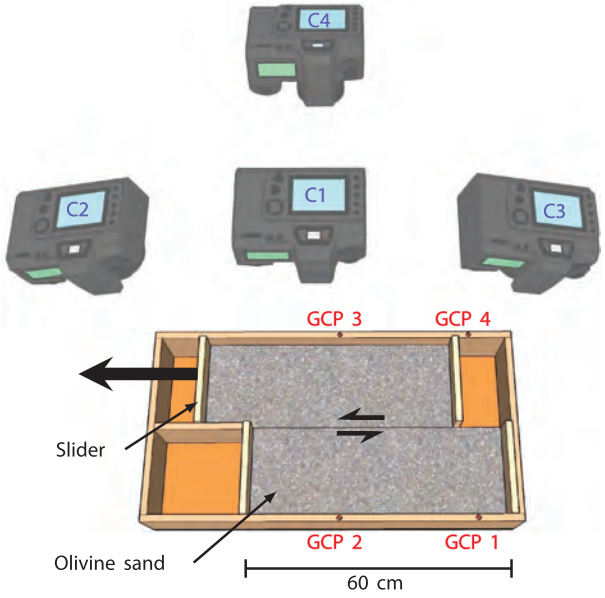

Figure 8. Sketch of the experimental apparatus used for geodetic measurements associated with strike-slip fault (see text for explanations). Four cameras view the sliding surface from above.

the same coordinate system, and their locations should match perfectly; thus, they can be superimposed (Figures 7b and 7c). Significantly, this procedure allows for direct and quantitative comparison between surface deformation pattern and the shape of the underlying intrusion. Notice, however, that intrusion observation is only postmortem, i.e., its propagation cannot be monitored in the subsurface. To date, this can only be done using XCT scanners.

4.2. Tectonic Deformation

4.2.1. Experimental Setup

Figure 8 displays the experimental setup used to monitor surface movements associated with a strike-slip fault under shear. We used olivine sand as model brittle crust. The advantage of olivine sand is the large distribution of grain colors, such that the surfaces of the models naturally exhibit a prominent random texture, which is required for the photogrammetric monitoring. Similarly to dry sand, olivine sand fails according to a Mohr-Coulomb friction law that exhibits a negligible cohesion [e.g., *El-Emam*, 2011].

The models were built and deformed in a rectangular box, 60 cm long and 40 cm wide (Figure 8), a modified and simplified version of that of, e.g., *Naylor et al*. [1986] and *Le Guerroué and Cobbold* [2006]. Half of the model was contained in a mobile slider that was pulled manually; the other half was fixed. The boundary between the mobile and the fixed parts of the box generated a velocity discontinuity at the base of the model and localized shear deformation within the sand pack (Figure 8). The amount of slip along the basal cut did not exceed 40 cm. The sand layer in our experiment was 8 cm thick; therefore, the lateral boundaries had little effect on deformation [see, e.g., *Le Guerroué and Cobbold*, 2006].

Models were constructed by pouring sand into the box and leveling the surface until horizontal. During deformation, four synchronized cameras took photographs of the model surface for each increment of deformation (Figure 8). The procedure for surface monitoring during the experiment was the following: between times t_i and t_{i+1} (Figure 9), 1 cm of shearing was manually applied to the model, and the corresponding DEMs (Figure 9, first row) and ΔDEMs between t_{i+1} and t_i were computed (Figure 9, second row). Nevertheless, horizontal displacements could not be computed by correlating the orthorectified images of this set of time steps only, because the MicMac function MM2DPosSism is designed to efficiently calculate displacements that are smaller than correlations window of small size (here 9 pixels, i.e., ~1 mm) [*Rosu et al*., 2015b]. Therefore, at each time t_i, we manually applied an infinitesimal shear increment (<1 mm) to compute the U_x and U_y maps (Figure 9, third and fourth rows). Note that at each increment of shearing (both centimeters and infinitesimal), we computed a DEM and an orthorectified image of the model surface.

4.2.2. Results

The time series of DEMs nicely illustrate the complex topography changes generated by shearing (Figure 9). At time t_1, several uplifted domains form (indicated by warmer colors); they are separated by localized structures that are oblique to the shearing direction. The overall width of the deformed zone is roughly the same as the model thickness (~8 cm). This uplift suggests local dilation along subsurface shear zones [*Le Guerroué and Cobbold*, 2006]. The displacement maps (U_x and U_y) exhibit prominent discontinuities, the locations of which coincide with the oblique structures visible on the DEM and the ΔDEM maps. The shear strain map calculated from the horizontal displacements shows that these oblique structures are zones of concentrated shear. At this early time step, however, the deformation is poorly localized, i.e., distributed over several fault segments.

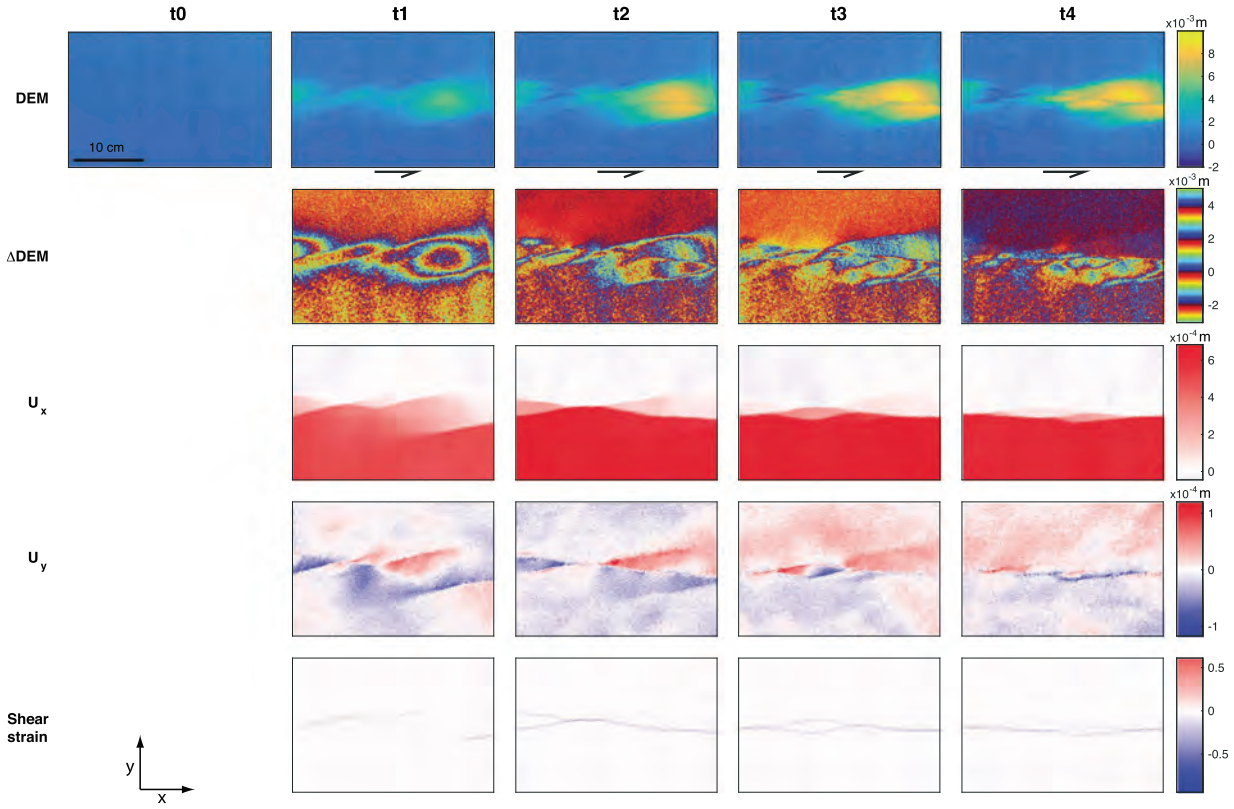

Figure 9. Plots of representative measurements of model surface evolution during an example strike-slip faulting experiment at four distinct time steps (columns). The plots display (first row) DEM, (second row) incremental ΔDEM (topography change between each times t_{i+1} and t_i), (third row) U_x (incremental surface displacements parallel to the x axis), (fourth row) U_y (incremental surface displacements parallel to the y axis), and (fifth row) shear strain field calculated from U_x and U_y field.

The data collected at time t_2 exhibit more complex patterns (Figure 9). For example, the DEM maps show that the largest initial uplifted domain (to the right of the map) is being dissected by a planar structure that is almost parallel to the shearing direction. The U_x and U_y maps show that this shear-parallel structure corresponds to a prominent displacement discontinuity, which in the shear strain map can be identified as a newly formed shear zone connected to existing oblique shear zones. Interestingly, the oblique shear zones that were bounding this dissected uplifted domain at time t_1 are not active any longer. Time t_2 thus illustrates the initiation of shear localization.

The data at times t_3 and t_4 show complex structural pattern development associated with shear localization (Figure 9). All initial oblique shear zones become inactive, and displacement is instead accommodated by a dominant shear-parallel shear zone. One can also observe localized uplift on the DEM map, as well as local subsidence along the left parts of the shear zone. These results highlight the detail of structural information obtainable by automatic DIC of orthorectified photos.

5. Discussion

5.1. Quality of the Results

The spatial resolutions of the DEMs, orthorectified images, and displacement maps are high with a pixel size of ~0.1 mm for a 40 × 40 cm model box; i.e., the resolution is 2.5×10^{-4} times the size of the experimental system. In fact, the resolution of the data is close to the resolution of the processed images. This implies that higher resolution of the data can be achieved by using higher-resolution cameras.

We established a procedure to quantify the precision of the DEM produced by the MicMac workflow presented in this paper. For this purpose, we performed 232 independent acquisitions of a static model surface

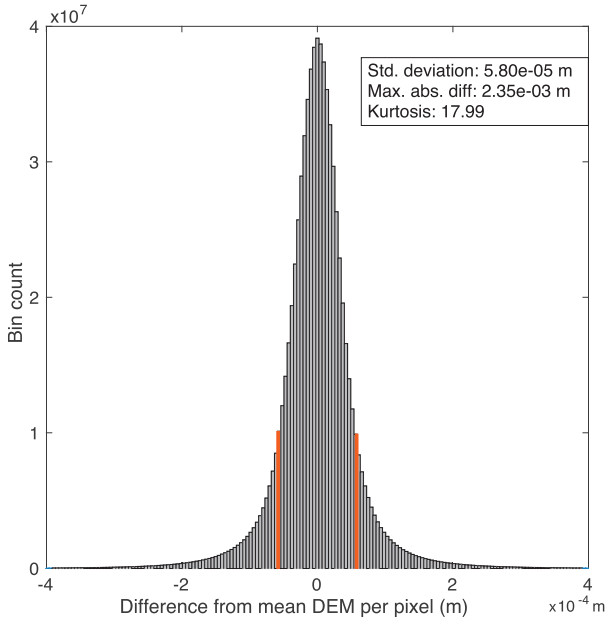

Figure 10. Histogram of the residual between pixels of (1) 232 DEMs of the same model surface and (2) the average DEM (see section 5.1 for detailed explanation). The residual distribution apparently follows a Gaussian distribution of standard deviation 5.8×10^{-5} m (indicated by red lines).

by randomly changing the positions of the four cameras. We then calculated a DEM for each set of camera positions, i.e., 232 DEMs, and calculated an average DEM. We then subtracted this average from each DEM and computed the residual distribution between each pixel of the 232 DEMs and the pixels of the average DEM (Figure 10). The residual distribution apparently exhibits a Gaussian distribution, the standard deviation of which quantifies the precision of the data, which is here 5.8×10^{-2} mm. Such precision allows imaging very small topographic features, such as surface cracks visible on the orthorectified image, DEM, and point cloud of Figure 3. Hence, the method presented in this paper can detect topography changes smaller than 0.1 mm.

We performed qualitative analyses and identified that the degree of precision of the DEM results is highly dependent on the model preparation procedure, in particular, the preparation of the random pattern on the model surface. For example, too few tie points on model surfaces due to, for example, locally insufficient density of coffee grains affects the image correlation and decreases the quality of the results. Therefore, a good model preparation procedure is as crucial to the results as a good photogrammetric workflow. In addition, in the magma intrusion experiment (see section 4), the erupting oil at the end of the experiment is transparent and reflective, which produces calculation errors (see DEM in Figure 3, where topographic features appear at the lava flow, whereas its surface is flat). Therefore, the method presented in this paper should be used on a nontransparent medium only.

We followed a similar procedure to quantify the precision of the horizontal displacements. For this purpose, we performed (1) four distinct acquisitions of the model surface before the beginning of a magma emplacement experiment and (2) three distinct acquisitions of the model surface after the end of the experiment. We systematically computed the associated total displacement fields by applying MM2DPosSism between each pair of orthorectified images taken before and after the experiment, and we averaged them. We then subtracted the average maps from each displacement map and computed the overall residual distributions for U_x and U_y (Figure 11). The residual distributions of the horizontal displacements exhibit standard deviations of 3.4×10^{-2} mm for U_x and 4.2×10^{-2} mm for U_y (i.e., the same order of precision), which is close to that of the DEM. Nevertheless, the distribution does not follow a simple Gaussian distribution but exhibits several peaks not centered on zero. Detailed analysis of our results shows that the individual residual distribution of each of the displacement maps is Gaussian, the maximum of which is not centered on zero. Given that each residual distribution is centered on distinct values, their combination thus produces a complex distribution exhibiting several peaks, as we obtain (Figure 11).

If the maximum of each residual distribution is not centered on zero, the average displacement on a given displacement map is not zero, i.e., the whole orthorectified image is shifted. This effect is visible on the displacement maps of Figures 5 and 6, where the model surfaces outside the uplifted areas exhibit subtle overall displacements while they did not move. We identified this effect as a result of the pixel size accuracy of the georeferencing procedure: if the resolution of the GCP's position is 1 pixel, the orthorectified image can be shifted accordingly, so it will produce an apparent horizontal shift of the model surface. However, this global shift is smaller than 1 pixel, i.e., $<$0.1 mm. It is possible to mitigate this effect through a more careful identification of the GCPs in the photographs.

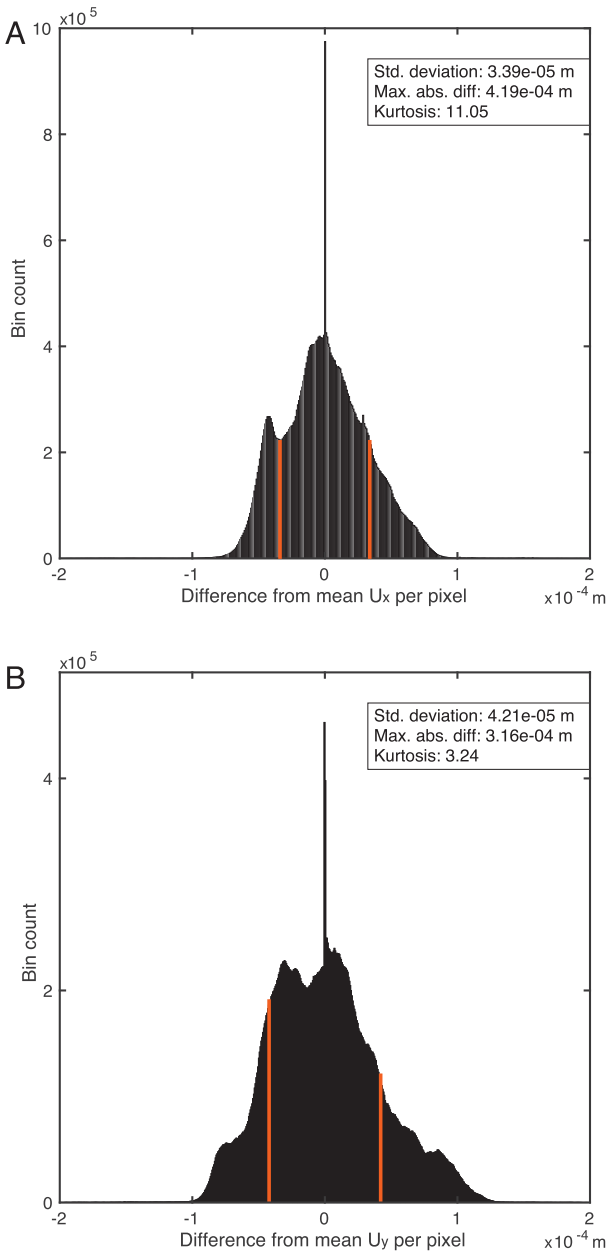

Figure 11. (a) Histogram of the residual between pixels of (1) 12 U_x maps of the same displacement field and (2) the average U_x map (see section 5.1 for detailed explanation). The residual distribution follows a complex distribution of standard deviation 3.4×10^{-5} m (indicated by red lines). (b) Histogram of the residual between pixels of (1) 12 U_y maps of the same displacement field and (2) the average U_y map (see section 5.1 for detailed explanation). The residual distribution follows a complex distribution of standard deviation 4.2×10^{-5} m (indicated by red lines).

In the magma emplacement experiments presented in this paper, the monitoring frequency was chosen arbitrarily at 1 Hz, which is suitable for the present experiments as the displacements are slow (~1 mm/min). The presented workflow, however, is valid at every acquisition frequency as long as the cameras (1) are synchronized and (2) produce contrasted, sharp images of pixel size smaller than monitored movements. Therefore, the photogrammetric workflow presented in this paper can theoretically be implemented for a wide range of laboratory studies involving processes of very different time scales, e.g., from slow tectonic processes to high-density current and pyroclastic flows or catastrophic volcano collapse.

5.2. Advantages Compared With Existing Methods

The great benefits of using MicMac in laboratory models of geological systems are that (1) it produces high-resolution and high-precision data; (2) it measures both topography and in-plane displacements fields; (3) it is possible to integrate surface deformation data with postmortem 3-D reconstruction of underlying structures (here a magmatic intrusion); and (4) it is relatively cheap as it employs an open-source software, the cameras are standard consumer grade DSLR cameras (preferably with fixed-zoom lenses), the computer systems required to run MicMac are standard, and the image processing is done after the experimental run (see section 3.2).

The use of MicMac is more advantageous than devices that measure topography only (e.g., lasers and structured light systems), as these do not compute the in-plane displacement maps; hence, the strain and divergence fields so rich in information could not be easily obtained. In addition, the present photogrammetric workflow is able to reconstruct complex solidified intrusion shapes (Figure 7), including subvertical ones. This is superior to the structured light moiré system described by *Galland* [2012], which is only able to reconstruct the upper surface of flat-lying intrusions.

The use of four standard DSLR cameras is slightly more expensive than the Microsoft® Kinect system used by *Tortini et al*. [2014], but the resolution and the precision of the results are more than an order of magnitude

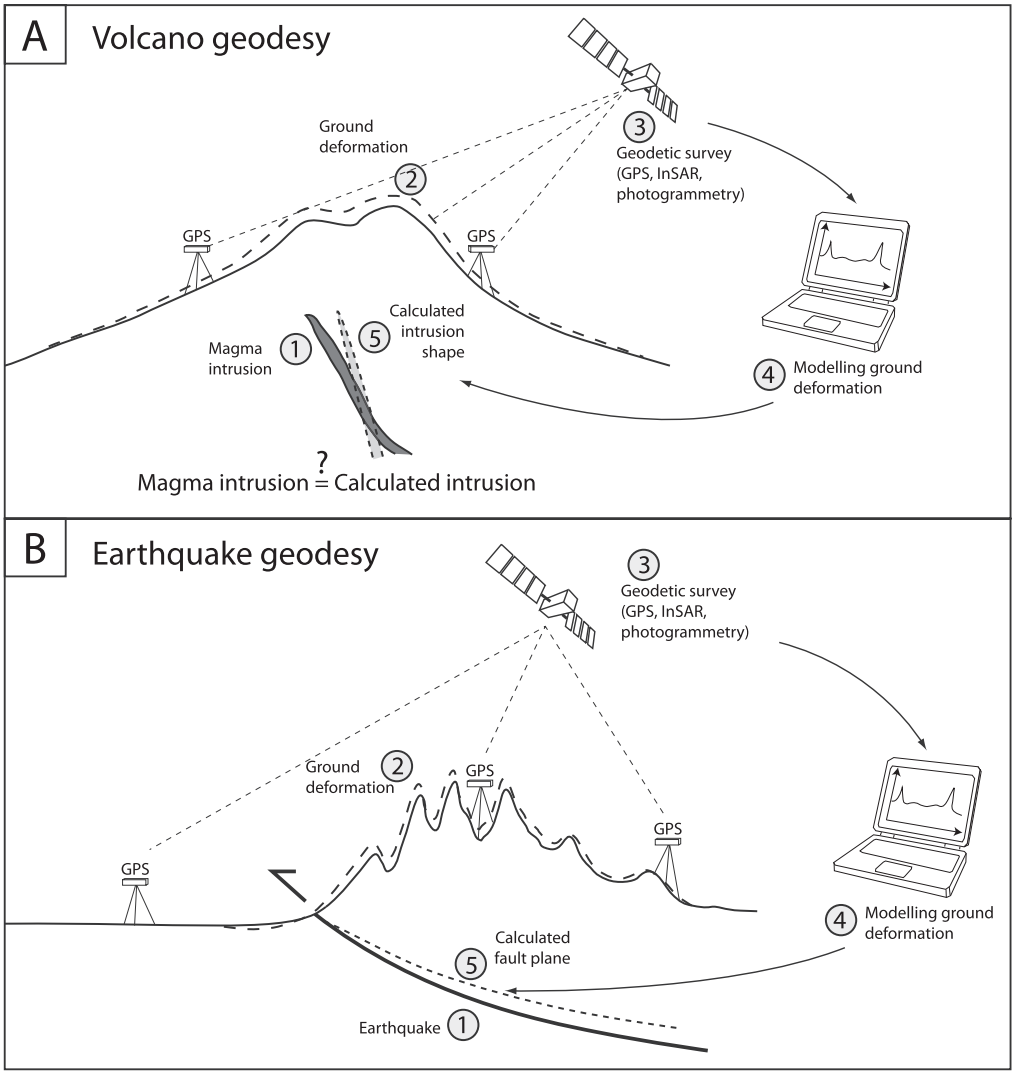

Figure 12. (a) Schematic diagram illustrating the principle of geodetic modeling applied to active volcanoes [*Galland*, 2012]. Numbering gives the succession of the stages of the analyses. (1) Magma intrudes within a volcano, feeding a magma reservoir or forming a sheet intrusion (dark gray intrusion). (2) Magma intrusion triggers ground deformation at the surface, leading to modified topography (dashed line). (3) Topography variation is measured by geodetic techniques (GPS, InSAR, photogrammetry, etc.). (4) Geodetic data are compared with modeling of ground deformation caused by various intrusion shapes. (5) The best fit between models and ground deformation data provides a calculated intrusion shape (light gray dashed intrusion) attributed to the measured ground deformation. (b) Schematic diagram illustrating the principle of geodetic modeling applied to earthquakes. Numbering gives the succession of the stages of the analyses. (1) An earthquake occurs associated with slip on fault plane (solid line). (2) Fault motion triggers ground deformation at the surface, leading to modified topography (dashed line). (3) Topography variation is measured by geodetic techniques. (4) Geodetic data are compared with modeling of ground deformation due to various fault plane shapes. (5) The best fit between models and ground deformation data provides a calculated fault shape and displacement field (dashed line) attributed to the measured ground deformation.

better with our SfM workflow. In addition, the Microsoft® Kinect system does not allow precise measurements of in-plane displacement fields.

The combination of DEM and in-plane displacement calculations permitted with MicMac is also an obvious advantage with respect to standard DIC methods, which only calculate displacements parallel to the observed surface. This is also possible with commercial stereo-DIC packages, though their costs can be prohibitive. In addition, the DIC analysis implemented in MicMac uses orthorectified images, and so the optical

distortion and the topographic distortion are corrected. Therefore, the DIC results produced by MicMac appear more robust that those of standard DIC packages.

5.3. Implications for Geodetic Measurements

During the few last decades, geodetic measurements such as interferometric synthetic aperture radar (InSAR) imaging and GPS measurements have become leading tools for monitoring Earth's surface movements related to active volcanoes and earthquakes (Figure 12) [e.g., *Cayol and Cornet*, 1998; *Froger et al*., 2007; *Shen et al*., 2009; *Fukushima et al*., 2010; *Sigmundsson et al*., 2010; *Vallage et al*., 2015]. These geodetic measurements are commonly analyzed and interpreted through geodetic modeling to calculate the shape and dynamics of the underlying (and unobservable) volcanic intrusion or fault responsible for displacements observed at the surface.

So far, geodetic modeling has been based only on analytical or numerical models. Although commonly used, these models have serious limitations:

1. They model simplistic intrusion and fault shapes, such as point source [*Mogi*, 1958; *Masterlark*, 2007], tensile [e.g., *Okada*, 1985; *Amelung et al*., 2000; *Wright et al*., 2006; *Chang et al*., 2007; *Sigmundsson et al*., 2010], or shear dislocation rectangle [*Okada*, 1985; *Shen et al*., 2009; *Gusman et al*., 2012; *Yue et al*., 2014]. These deformation sources are not representative of the complex shapes of magmatic intrusions or fault planes in nature [e.g., *Burchardt*, 2008; *Lohr et al*., 2008; *Burchardt et al*., 2012].
2. They model static intrusions/fault planes, such that they do not account for the complex magma propagation mechanisms [*Mathieu et al*., 2008; *Abdelmalak et al*., 2012] or fault mechanics [*Mair and Abe*, 2008, 2011; *Brodsky and Lay*, 2014];
3. It is impossible to quantify the uncertainties of the model results and so to test their robustness. The main reason is that active geological processes occur in the subsurface, so that the results of the modeling cannot be validated by direct observations.

In contrast to the commonly used analytic and numerical geodetic models, laboratory models can simulate the complex dynamics of magma emplacement and fault mechanics and the resulting surface deformation [e.g., *Le Guerroué and Cobbold*, 2006; *Galland et al*., 2009; *Abdelmalak et al*., 2012; *Galland*, 2012]. In addition, the internal structures in the laboratory models can be directly observed, and they exhibit complex, geologically relevant shapes [*Galland et al*., 2014]. Therefore, the implementation of MicMac for monitoring surface deformation in laboratory models has the potential to (1) account for relevant and complex intrusion and/or fault shapes in Earth geodetic models, (2) test the robustness of commonly used geodetic models by integrating laboratory surface and subsurface data, and (3) test the effects of dynamic processes (e.g., magma intrusion propagation and fault mechanics) on geodetic models. Crucially, the geodetic data obtained in the laboratory can be directly mapped to field geodesy.

6. Conclusions

This paper describes the implementation of the open-source photogrammetric software MicMac for quantitative monitoring of surface deformation in laboratory models of geological systems. Two example geological systems are presented. The main results of our study are the following.

1. The implementation of MicMac in the laboratory is easily affordable, as it requires only four synchronized standard DSLR cameras and the use of the open-source MicMac package combined with Matlab® to monitor and analyze model surfaces.
2. The MicMac workflow implemented in this paper produces high-resolution DEMs, orthorectified images, and high-density point clouds of the monitored model surface.
3. The resolution of the output data is the same as those of the images taken from the cameras (here <0.1 mm out of a 40×40 cm box for a camera resolution of 24 MP).
4. The precision of the DEM and horizontal displacements measured with our setup is ~0.05 mm.
5. The high resolution of the horizontal displacement fields allows quantitative and automatic mapping of open and shear fractures by calculating the divergence (dilation) and shear strain, respectively, of the horizontal displacement fields.
6. MicMac also offers the possibility to compute 3-D models of excavated structures (here a solidified model magma intrusion), which can be integrated with the corresponding surface data.

The main limitation of the method presented here is that it does not allow monitoring of subsurface displacements/structures like XCT scanners.

To summarize, MicMac is the first tool that combines the following advantages: (1) relatively low cost, (2) high-resolution and high-precision results, (3) measurements of topography and horizontal displacements, (4) ease of setup in the laboratory (no lengthy calibration procedure), and (5) possibility of integrating surface and subsurface data. This package thus appears to be a very promising tool for quantitative monitoring of surface deformation in laboratory models of geological systems. Given its numerous benefits, the use of the procedure described here has the potential to become a generalized tool in many laboratories.

Acknowledgments

This work was supported by a Center of Excellence grant from the Norwegian Research Council to PGP (grant 146031). Bertelsen's position is funded by the Faculty of Mathematics and Natural Sciences at the University of Oslo. Guldstrand's position is funded by the DIPS (Dynamics of igneous plumbing systems, grant 240467) project, distributed by the Norwegian Research Council. Girod was funded by the European Research Council under the European Union's Seventh Framework Programme (FP/2007–2013)/ERC grant agreement 320816. Gulsdtrand, Bjugger, and Burchardt acknowledge an exchange visiting grant (grant 4251) through the MeMoVolc Networking Programme, funded by the European Science Foundation. The data used in this paper are available directly from the authors. We acknowledge the very constructive reviews by K.A. Leever and S. Poppe.

References

Abdelmalak, M. M., R. Mourgues, O. Galland, and D. Bureau (2012), Fracture mode analysis and related surface deformation during dyke intrusion: Results from 2D experimental modelling, *Earth Planet. Sci. Lett.*, *359-360*, 93–105.

Acocella, V., F. Cifelli, and R. Funiciello (2001), The control of overburden thickness on resurgent domes: Insights from analogue models, *J. Volcanol. Geotherm. Res.*, *111*(1-4), 137–153.

Adam, J., J. L. Urai, B. Wieneke, O. Oncken, K. Pfeiffer, N. Kukowski, J. Lohrmann, S. Hoth, W. van der Zee, and J. Schmatz (2005), Shear localisation and strain distribution during tectonic faulting—New insights from granular-flow experiments and high-resolution optical image correlation techniques, *J. Struct. Geol.*, *27*(2), 283–301.

Adam, J., M. Klinkmüller, G. Schreurs, and B. Wieneke (2013), Quantitative 3D strain analysis in analogue experiments simulating tectonic deformation: Integration of X-ray computed tomography and digital volume correlation techniques, *J. Struct. Geol.*, *55*, 127–149.

Amelung, F., S. Jonsson, H. Zebker, and P. Segall (2000), Widespread uplift and "trapdoor" faulting on Galápagos volcanoes observed with radar interferometry, *Nature*, *407*(6807), 993–996.

Babault, J., S. Bonnet, A. Crave, and J. Van Den Driessche (2005), Influence of piedmont sedimentation on erosion dynamics of an uplifting landscape: An experimental approach, *Geology*, *33*(4), 301–304.

Babault, J., S. Bonnet, J. Van Den Driessche, and A. Crave (2007), High elevation of low-relief surfaces in mountain belts: Does it equate to post-orogenic surface uplift?, *Terra Nova*, *19*(4), 272–277.

Bay, H., T. Tuytelaars, and L. Van Gool (2006), SURF: Speeded Up Robust Features, in *Computer Vision—ECCV 2006*, edited by A. Leonardis, H. Bischof, and A. Pinz, pp. 404–417, Springer, Berlin Heidelberg.

Beyer, H. A. (1992a), Accurate calibration of CCD-cameras, paper presented at Computer Vision and Pattern Recognition, 1992, Proc. CVPR '92, 1992 IEEE Comp. Soc. Conf., 15-18 Jun 1992.

Beyer, H. A. (1992b), Geometric and radiometric analysis of a CCD-camera based photogrammetric close-range system PhD thesis, ETH Zürich, Swirtzerland, Institute for Geodesy and Photogrammetry, Dissertation 9701.

Brèque, C., J.-C. Dupré, and F. Brémand (2004), Calibration of a system of projection moiré for relief measuring: Biomechanical applications, *Opt. Lasers Eng.*, *41*(2), 241–260.

Bretar, F., M. Arab-Sedze, J. Champion, M. Pierrot-Deseilligny, E. Heggy, and S. Jacquemoud (2013), An advanced photogrammetric method to measure surface roughness: Application to volcanic terrains in the Piton de la Fournaise, Reunion Island, *Remote Sens. Environ.*, *135*, 1–11.

Brodsky, E. E., and T. Lay (2014), Recognizing foreshocks from the 1 April 2014 Chile earthquake, *Science*, *344*(6185), 700–702.

Burchardt, S. (2008), New insights into the mechanics of sill emplacement provided by field observations of the Njardvik Sill, Northeast Iceland, *J. Volcanol. Geotherm. Res.*, *173*(3-4), 280–288.

Burchardt, S., and T. R. Walter (2010), Propagation, linkage, and interaction of caldera ring-faults: Comparison between analogue experiments and caldera collapse at Miyakejima, Japan, in 2000, *Bull. Volcanol.*, *72*(3), 297–308.

Burchardt, S., D. C. Tanner, and M. Krumbholz (2012), The Slaufrudalur pluton, southeast Iceland—An example of shallow magma emplacement by coupled cauldron subsidence and magmatic stoping, *Geol. Soc. Am. Bull.*, *124*(1-2), 213–227.

Byrne, P. K., E. P. Holohan, M. Kervyn, B. van Wyk de Vries, and V. R. Troll (2015), Analogue modelling of volcano flank terrace formation on Mars, *Geol. Soc. London, Spec. Publ.*, *401*(1), 185–202.

Cayol, V., and F. H. Cornet (1998), Three-dimensional modeling of the 1983–1984 eruption at Piton de la Fournaise volcano, Reunion Island, *J. Geophys. Res.*, *103*(B8), 18,025–18,037, doi:10.1029/98JB00201.

Cecchi, E., B. van Wyk de Vries, J. M. Lavest, A. Harris, and M. Davies (2003), N-view reconstruction: A new method for morphological modelling and deformation measurement in volcanology, *J. Volcanol. Geotherm. Res.*, *123*(1-2), 181–201.

Chang, W.-L., R. B. Smith, C. Wicks, J. M. Farrell, and C. M. Puskas (2007), Accelerated uplift and magmatic intrusion of the Yellowstone caldera, 2004 to 2006, *Science*, *318*(5852), 952–956.

Delcamp, A., B. van Wyk de Vries, and M. R. James (2008), The influence of edifice slope and substrata on volcano spreading, *J. Volcanol. Geotherm. Res.*, *177*(4), 925–943.

Donnadieu, F., K. Kelfoun, B. van Wyk de Vries, E. Cecchi, and O. Merle (2003), Digital photogrammetry as a tool in analogue modelling: Applications to volcano instability, *J. Volcanol. Geotherm. Res.*, *123*(1-2), 161–180.

El-Emam, M. (2011), Experimental and numerical study of at-rest lateral Earth pressure of overconsolidated sand, *Adv. Civ. Eng.*, *2011*, 1–12, doi:10.1155/2011/524568.

Farzipour-Saein, A., F. Nilfouroushan, and H. Koyi (2013), The effect of basement step/topography on the geometry of the Zagros fold and thrust belt (SW Iran): An analog modeling approach, *Int. J. Earth Sci.*, *102*(8), 2117–2135.

Fort, X., J. P. Brun, and F. Chauvel (2004), Contraction induced by block rotation above salt (Angolan margin), *Mar. Pet. Geol.*, *21*(10), 1281–1294.

Froger, J. L., D. Remy, S. Bonvalot, and D. Legrand (2007), Two scales of inflation at Lastarria-Cordon del Azufre volcanic complex, central Andes, revealed from ASAR-ENVISAT interferometric data, *Earth Planet. Sci. Lett.*, *255*(1-2), 148–163.

Fukushima, Y., V. Cayol, P. Durand, and D. Massonnet (2010), Evolution of magma conduits during the 1998–2000 eruptions of Piton de la Fournaise volcano, Réunion Island, *J. Geophys. Res.*, *115*, B10204, doi:10.1029/2009JB007023.

Galerne, C. Y., O. Galland, E. R. Neumann, and S. Planke (2011), 3D relationships between sills and their feeders: Evidence from the Golden Valley Sill Complex (Karoo Basin) and experimental modelling, *J. Volcanol. Geotherm. Res.*, *202*(3-4), 189–199.

Galland, O. (2012), Experimental modelling of ground deformation associated with shallow magma intrusions, *Earth Planet. Sci. Lett.*, *317-318*, 145–156.
Galland, O., and J. Scheibert (2013), Analytical model of surface uplift above axisymmetric flat-lying magma intrusions: Implications for sill emplacement and geodesy, *J. Volcanol. Geotherm. Res.*, *253*, 114–130.
Galland, O., P. R. Cobbold, E. Hallot, J. de Bremond d'Ars, and G. Delavaud (2006), Use of vegetable oil and silica powder for scale modelling of magmatic intrusion in a deforming brittle crust, *Earth Planet. Sci. Lett.*, *243*, 786–804.
Galland, O., P. R. Cobbold, J. de Bremond d'Ars, and E. Hallot (2007), Rise and emplacement of magma during horizontal shortening of the brittle crust: Insights from experimental modeling, *J. Geophys. Res.*, *112*, B06402, doi:10.1029/2006JB004604.
Galland, O., S. Planke, E. R. Neumann, and A. Malthe-Sørenssen (2009), Experimental modelling of shallow magma emplacement: Application to saucer-shaped intrusions, *Earth Planet. Sci. Lett.*, *277*(3-4), 373–383.
Galland, O., S. Burchardt, E. Hallot, R. Mourgues, and C. Bulois (2014), Dynamics of dikes versus cone sheets in volcanic systems, *J. Geophys. Res. Solid Earth*, *119*, 6178–6192, doi:10.1002/2014JB011059.
Girod, L. (2012), The use of SfM technologies in geosciences: Micmac for geologists Ecole Nationnale des Sciences Geographiques - ENSG.
Graveleau, F., and S. Dominguez (2008), Analogue modelling of the interaction between tectonics, erosion and sedimentation in foreland thrust belts, *C. R. Geosci.*, *340*(5), 324–333.
Graveleau, F., J. Malavieille, and S. Dominguez (2012), Experimental modelling of orogenic wedges: A review, *Tectonophysics*, *538-540*, 1–66.
Grujic, D., T. R. Walter, and H. Gärtner (2002), Shape and structure of (analogue models of) refolded layers, *J. Struct. Geol.*, *24*(8), 1313–1326.
Gusman, A. R., Y. Tanioka, S. Sakai, and H. Tsushima (2012), Source model of the great 2011 Tohoku earthquake estimated from tsunami waveforms and crustal deformation data, *Earth Planet. Sci. Lett.*, *341-344*, 234–242.
Haug, Ø. T., M. Rosenau, K. A. Leever, and O. Oncken (2014), Modelling fragmentation in rock avalanches, in *Landslide Science for a Safer Geoenvironment*, edited by K. Sassa, P. Canuti, and Y. Yin, pp. 93–100, Springer.
Holland, M., J. L. Urai, and S. Martel (2006), The internal structure of fault zones in basaltic sequences, *Earth Planet. Sci. Lett.*, *248*(1-2), 301–315.
Hubbert, M. K. (1937), Theory of scale models as applied to the study of geologic structures, *Geol. Soc. Am. Bull.*, *48*, 1459–1520.
Kavanagh, J. L., D. Boutelier, and A. R. Cruden (2015), The mechanics of sill inception, propagation and growth: Experimental evidence for rapid reduction in magmatic overpressure, *Earth Planet. Sci. Lett.*, *421*, 117–128.
Koenderink, J. J., and A. J. van Doorn (1991), Affine structure from motion, *J. Opt. Soc. Am. A*, *8*(2), 377–385.
Lague, D., A. Crave, and P. Davy (2003), Laboratory experiments simulating the geomorphic response to tectonic uplift, *J. Geophys. Res.*, *108*(B1), 2008, doi:10.1029/2002JB001785.
Lawson, J. M., and J. R. Dawson (2014), A scanning PIV method for fine-scale turbulence measurements, *Exp. Fluids*, *55*(12), 1–19.
Le Guerroué, E., and P. R. Cobbold (2006), Influence of erosion and sedimentation on strike-slip fault systems: Insights from analogue models, *J. Struct. Geol.*, *28*(3), 421–430.
Leever, K. A., R. H. Gabrielsen, D. Sokoutis, and E. Willingshofer (2011), The effect of convergence angle on the kinematic evolution of strain partitioning in transpressional brittle wedges: Insight from analog modeling and high-resolution digital image analysis, *Tectonics*, *30*, TC2013, doi:10.1029/2010TC002823.
Leever, K. A., O. Galland, and V. Acocella (2014), The science behind laboratory-scale models of the Earth, *Eos Trans. AGU*, *95*(3), 30–30, doi:10.1002/2014EO030008.
Leprince, S., S. Barbot, F. Ayoub, and J. Avouac (2007), Automatic, precise, ortho-rectification and co-registration for satellite image correlation, application to seismotectonics, *IEEE Trans. Geosci. Remote Sens.*, *45*, 1529–1558.
Lickorish, W. H., M. Ford, J. Bürgisser, and P. R. Cobbold (2002), Arcuate thrust systems in sandbox experiments: A comparison to the external arcs of the Western Alps, *Geol. Soc. Am. Bull.*, *114*(9), 1089–1107.
Lohr, T., C. M. Krawczyk, O. Oncken, and D. C. Tanner (2008), Evolution of a fault surface from 3D attribute analysis and displacement measurements, *J. Struct. Geol.*, *30*(6), 690–700.
Lowe, D. G. (2004), Distinctive image features from scale-invariant keypoints, *Int. J. Comput. Vision*, *60*(2), 91–110.
Mair, K., and S. Abe (2008), 3D numerical simulations of fault gouge evolution during shear: Grain size reduction and strain localization, *Earth Planet. Sci. Lett.*, *274*(1-2), 72–81.
Mair, K., and S. Abe (2011), Breaking up: Comminution mechanisms in sheared simulated fault gouge, *Pure Appl. Geophys.*, *168*(12), 2277–2288.
Martinod, J., and P. Davy (1994), Periodic instabilities during compression of the lithosphere: 2. Analogue experiments, *J. Geophys. Res.*, *99*(B6), 12,057–12,069, doi:10.1029/93JB03599.
Masterlark, T. (2007), Magma intrusion and deformation predictions: Sensitivities to the Mogi assumptions, *J. Geophys. Res.*, *112*, B06419, doi:10.1029/2006JB004860.
Mathieu, L., B. van Wyk de Vries, E. P. Holohan, and V. R. Troll (2008), Dykes, cups, saucers and sills: Analogue experiments on magma intrusion into brittle rocks, *Earth Planet. Sci. Lett.*, *271*(1-4), 1–13.
Meydenbauer, A. (1867), Die photogrammetrie, *Wochenbl. Archit.-Ver. zu Berlin*, *1*(49), 472.
Mogi, K. (1958), Relations between the eruptions of various volcanoes and the deformations of the ground surface around them, *Bull. Earthquake Res. Inst. Univ. Tokyo*, *36*, 99–134.
Morel, J.-M., and G. Yu (2009), Asift: A new framework for fully affine invariant image comparison, *SIAM J. Imaging Sci.*, *2*(2), 438–469.
Naylor, M. A., G. Mandl, and C. H. K. Supesteijn (1986), Fault geometries in basement-induced wrench faulting under different initial stress states, *J. Struct. Geol.*, *8*(7), 737–752.
Okada, Y. (1985), Surface deformation due to shear and tensile faults in a half-space, *Bull. Seismol. Soc. Am.*, *75*(4), 1135–1154.
Pierrot-Deseilligny, M., M. Deveau, J. Belvaux, G. Choqueux, G. Maillet, and L. Girod (2015a), *MicMac, Apero, Pastis and Other Beverages in a Nutshell!*, edited LGA, IGN, Champs-sur-Marne, France.
Pierrot-Deseilligny, M., M. Deveau, J. Belvaux, G. Choqueux, G. Maillet, and L. Girod (2015b), Micmac webpage edited.
Pollard, D. D., and A. M. Johnson (1973), Mechanics of growth of some laccolithic intrusions in the Henry Mountains, Utah, II. Bending and failure of overburden layers and sill formation, *Tectonophysics*, *18*, 311–354.
Poppe, S., E. P. Holohan, E. Pauwels, V. Cnudde, and M. Kervyn (2015), Sinkholes, pit craters, and small calderas: Analog models of depletion-induced collapse analyzed by computed X-ray microtomography, *Geol. Soc. Am. Bull.*, *127*(1-2), 281–296.
Reiter, K., N. Kukowski, and L. Ratschbacher (2011), The interaction of two indenters in analogue experiments and implications for curved fold-and-thrust belts, *Earth Planet. Sci. Lett.*, *302*(1–2), 132–146.
Rosenau, M., R. Nerlich, S. Brune, and O. Oncken (2010), Experimental insights into the scaling and variability of local tsunamis triggered by giant subduction megathrust earthquakes, *J. Geophys. Res.*, *115*, B09314, doi:10.1029/2009JB007100.
Rosu, A.-M., M. Assenbaum, Y. De la Torre, and M. Pierrot-Deseilligny (2015a), Coastal digital surface model on low contrast images, *International Archives of the Photogrammetry, Remote Sensing and Spatial Information Sciences*, XL-3/W3, pp. 307–312.

Rosu, A.-M., M. Pierrot-Deseilligny, A. Delorme, R. Binet, and Y. Klinger (2015b), Measurement of ground displacement from optical satellite image correlation using the free open-source software MicMac, *ISPRS J. Photogramm. Remote Sens.*, *100*, 48–59.

Schreurs, G., and B. Colletta (1998), Analogue modelling of faulting in zones of continental transpression and transtension, *Geol. Soc. London, Spec. Publ.*, *135*(1), 59–79.

Shen, Z.-K., J. Sun, P. Zhang, Y. Wan, M. Wang, R. Burgmann, Y. Zeng, W. Gan, H. Liao, and Q. Wang (2009), Slip maxima at fault junctions and rupturing of barriers during the 2008 Wenchuan earthquake, *Nat. Geosci.*, *2*(10), 718–724.

Sigmundsson, F., et al. (2010), Intrusion triggering of the 2010 Eyjafjallajökull explosive eruption, *Nature*, *468*(7322), 426–430.

Snavely, N., S. M. Seitz, and R. Szeliski (2006), Photo tourism: Exploring photo collections in 3D, in *ACM SIGGRAPH 2006 Pap.*, pp. 835–846, ACM, Boston, Mass.

Snavely, N., S. M. Seitz, and R. Szeliski (2008), Modeling the world from Internet photo collections, *Int. J. Comput. Vision*, *80*(2), 189–210.

Sokoutis, D., and E. Willingshofer (2011), Decoupling during continental collision and intra-plate deformation, *Earth Planet. Sci. Lett.*, *305*(3–4), 435–444.

Sveen, J. K. (2004), An introduction to MatPIV v. 1.6. 1 Preprint series. Mechanics and Applied Mathematics http://urn. nb. no/URN: NBN: No-23418.

Tortini, R., F. L. Bonali, C. Corazzato, S. A. Carn, and A. Tibaldi (2014), An innovative application of the Kinect in Earth sciences: Quantifying deformation in analogue modelling of volcanoes, *Terra Nova*, *26*(4), 273–281.

Trippanera, D., V. Acocella, and J. Ruch (2014), Dike-induced contraction along oceanic and continental divergent plate boundaries, *Geophys. Res. Lett.*, *40*, 1–7, doi:10.1002/2014GL061570.

Vallage, A., Y. Klinger, R. Grandin, H. S. Bhat, and M. Pierrot-Deseilligny (2015), Inelastic surface deformation during the 2013 M_w 7.7 Balochistan, Pakistan, earthquake, *Geology*, *43*(12), 1079–1082.

Westoby, M. J., J. Brasington, N. F. Glasser, M. J. Hambrey, and J. M. Reynolds (2012), "Structure-from-Motion" photogrammetry: A low-cost, effective tool for geoscience applications, *Geomorphology*, *179*, 300–314.

White, D. J., W. A. Take, and M. D. Bolton (2003), Soil deformation measurement using particle image velocimetry (PIV) and photogrammetry, *Geotechnique*, *53*(7), 619–631.

Wright, T. J., C. Ebinger, J. Biggs, A. Ayele, G. Yirgu, D. Keir, and A. Stork (2006), Magma-maintained rift segmentation at continental rupture in the 2005 Afar dyking episode, *Nature*, *442*(7100), 291–294.

Yue, H., T. Lay, L. Rivera, C. An, C. Vigny, X. Tong, and J. C. Báez Soto (2014), Localized fault slip to the trench in the 2010 Maule, Chile M_w = 8.8 earthquake from joint inversion of high-rate GPS, teleseismic body waves, InSAR, campaign GPS, and tsunami observations, *J. Geophys. Res. Solid Earth*, *119*, 7786–7804.

Dynamics of Surface Deformation Induced by Dikes and Cone Sheets in a Cohesive Coulomb Brittle Crust

Guldstrand, F., S. Burchardt, E. Hallot, and O. Galland

Journal of Geophysical Research: Solid Earth, *122*(10), 8511-8524, (2017)

https://doi.org/10.1002/2017JB014346

II

AGU PUBLICATIONS

JGR

Journal of Geophysical Research: Solid Earth

RESEARCH ARTICLE
10.1002/2017JB014346

Key Points:
- Laboratory models of surface deformation associated with dike and cone sheet emplacement in a cohesive Coulomb crust
- Dike emplacement systematically triggers surface uplift, in contrast to established elastic models
- We identify distinct surface deformation patterns and evolutions associated with dike and cone sheet emplacement

Supporting Information:
- Supporting Information S1

Correspondence to:
F. Guldstrand,
f.b.b.guldstrand@geo.uio.no

Citation:
Guldstrand, F., Burchardt, S., Hallot, E., & Galland, O. (2017). Dynamics of surface deformation induced by dikes and cone sheets in a cohesive Coulomb brittle crust. *Journal of Geophysical Research: Solid Earth*, *122*, 8511–8524. https://doi.org/10.1002/2017JB014346

Received 18 APR 2017
Accepted 22 SEP 2017
Accepted article online 4 OCT 2017
Published online 21 OCT 2017

Dynamics of Surface Deformation Induced by Dikes and Cone Sheets in a Cohesive Coulomb Brittle Crust

F. Guldstrand[1], S. Burchardt[2], E. Hallot[3], and O. Galland[1]

[1]Physics of Geological Processes, Department of Geosciences, University of Oslo, Oslo, Norway, [2]Centre for Mineralogy, Petrology and Geochemistry, Department of Earth Sciences, Uppsala University, Uppsala, Sweden, [3]Geosciences Rennes, UMR 6118, OSUR, CNRS-Université de Rennes 1, Rennes, France

Abstract The analysis of surface deformation associated with intruding magma has become an established method to study subsurface processes and intrusion architecture. Active subsurface magmatism induces deformation that is commonly modeled using static elastic models. To what extent, Coulomb failure of the crust affects surface deformation remains, so far, largely unexplored. In this contribution we present quantitative laboratory results of surface deformation induced by the emplacement of simulated dikes and cone sheets in a cohesive Coulomb material. The analysis of the experimental surface deformation shows that these intrusion types produce distinct and characteristic surface deformation signatures, which reflect the evolution of the intrusion at depth. Generally, dikes show a two-phase evolution while cone sheets develop gradually. In comparison, cone sheets induce larger uplifted areas and volumes than dikes relative to the depth of the injection source. Dike formation is, in turn, is likely accommodated, to a larger degree than cone sheets, by lateral opening of the host consistent with our current understanding of dike emplacement mechanics. Notably, only surface uplifts develop above the experimental dikes, consistent with a *viscous indenter* propagation mechanism, that is, a dike pushing ahead. The measured surface deformation patterns associated with dikes starkly contrast with established static, elastic models that predict local subsidence above the tip of a dike. This suggests that Coulomb failure of crustal rocks may considerably affect surface deformation induced by propagating igneous intrusions. This is especially relevant when a relatively high viscosity magma intrudes a weak host, such as unconsolidated sedimentary and volcaniclastic rocks.

1. Introduction

The analysis of surface deformation induced by ascending magma has developed into an established method to study the dynamics and geometry of subsurface magmatic activity (Amelung et al., 2000; Chadwick et al., 2011; Sigmundsson et al., 2015). This method postulates that the surface deformation reflects the combination of the shape of the intrusion, magma pressure distribution, subsurface propagation, and magma flow. Monitored surface deformation patterns are commonly fitted with geodetic models, in which the host rock deforms purely elastically (Dzurisin, 2006; Mogi, 1958; Okada, 1985).

However, the Earth's brittle crust is a cohesive, Coulomb material, implying that it does not only deform elastically. Recent field observations (Gudmundsson et al., 2008; Spacapan et al., 2017; Trippanera, Acocella, & Ruch, 2014) and modeling results (Abdelmalak et al., 2012; Haug et al., 2017; Pollard, 1973; Scheibert, Galland, & Hafver, 2017) show that brittle shear deformation may be significant in accommodating the emplacement of intrusions and the propagation of their tips. In addition, focal plane mechanisms constrained from dike-induced microseismicity dominantly involve shear failure of the host rock (Ágústsdóttir et al., 2016; White et al., 2011). These studies suggest that brittle shear deformation, which is generally not accounted for in geodetic models, may be nonnegligible during dike emplacement. Currently, it is not known to which extent intrusion-induced brittle deformation affects surface deformation patterns.

In this study, we explore the surface deformation patterns induced by sheet intrusions in a cohesive, Coulomb brittle host through quantitative laboratory models. The experimental procedure uses a cohesive fine-grained silica flour as model crust, and a molten, low-viscosity vegetable oil as model magma. This procedure builds on the setup and materials developed in Galland et al. (2006), the proof-of-concept of surface deformation shown in Galland (2012), and a parametric study of dykes versus cone sheet emplacement by

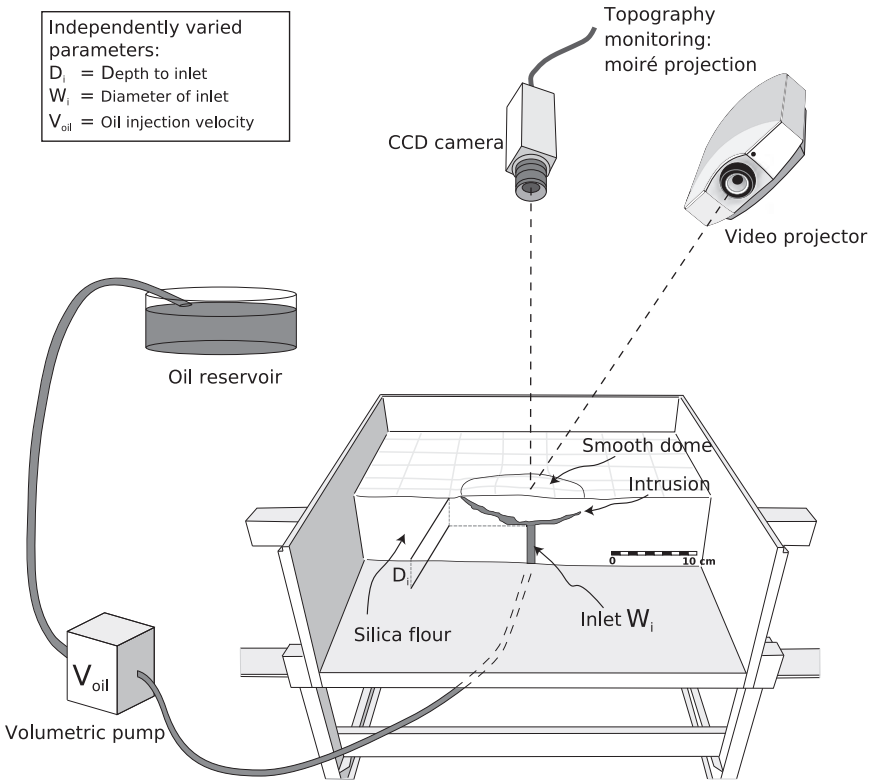

Figure 1. Schematic illustration of the experimental setup (modified from Galland, 2012; Galland et al., 2006). Oil is injected through a circular inlet using a volumetric pump into a 40 cm wide square box containing silica flour. The surface deformation induced by the resulting intrusion is periodically monitored using a moiré monitoring system. To control the shapes of the intrusions, the depth, D_i, and diameter, W_i, of the inlet, and the injection velocity of the oil, V_{oil}, were systematically varied (Galland et al., 2014).

Galland et al. (2014). This study presents a analysis of the large surface deformation data sets acquired during the experiments described in Galland et al. (2014).

During these experiments, the intrusion of the oil into the flour induced surface deformation that we monitored through a moiré projection method (Figure 1) (Bréque et al., 2004). We systematically analyzed the surface deformation associated with the two intrusions types, dikes, and cone sheets (Figure 2), from most of the experiments from Galland et al. (2014). Here we quantified how these two intrusion types induce distinguishable patterns of surface deformation.

2. Experimental Setup and Method

The experimental series used in this study are from those of the experiments of Galland et al. (2014) for which surface deformation data were available. In the experiments, (1) the inlet diameter (2, 5, and 10 mm), W_i; (2) the injection velocity (0.017 to 0.21 m s^{-1}), and (3) the injection depth (2 to 10 cm), D_i, were varied independently (Figure 1). The inlet was a cylindrical tube with circular section, the internal diameter of which affected the initial conditions of the models along with parameters (2) and (3) and so the geometry of the produced intrusions. Galland et al. (2014) showed that depending on the combination of the values of these three parameters, dikes, cone sheets, or "hybrid" intrusions that exhibit both dike and cone sheet characteristics are spontaneously produced (Figures 2 and 3). In the present study, we focus on the analysis of the surface deformation patterns associated with the development of the dikes and cone sheets.

We used the generic experimental protocol designed by Galland et al. (2006, 2009, 2014) and Galland (2012), in which the model materials are fine-grained silica flour and molten vegetable oil, to simulate brittle rocks and magma, respectively. The flour consists of fine (~15 μm), angular grains of crystalline silica flour under

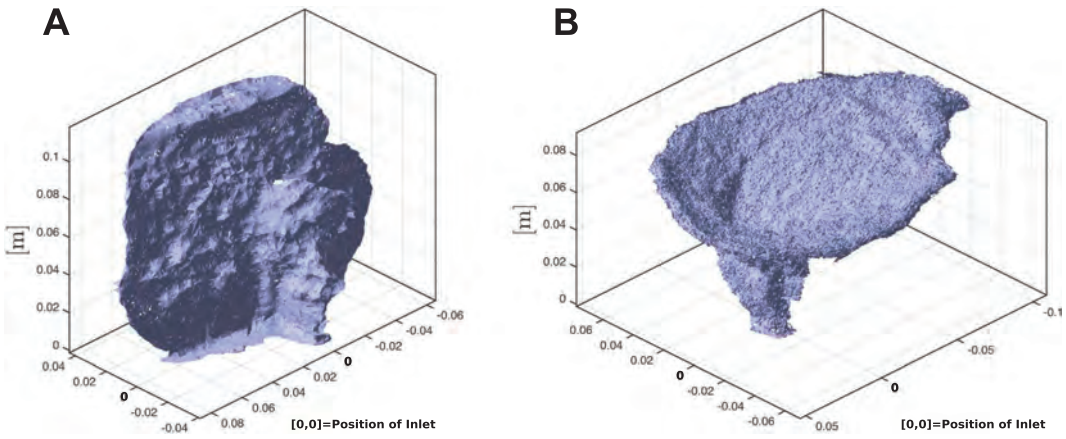

Figure 2. Meshed point clouds created through the use of Structure-from-Motion software MicMac (Galland et al., 2016) for two experimental intrusions produced using our laboratory setup, (a) dike and (b) cone sheet; 0 marks the position of the inlet.

the product name M400, manufactured in Belgium by Sibelco. It has a cohesive strength of 369 ± 44 Pa, a friction coefficient of 0.81 ± 0.06 (corresponding to an angle of internal friction of ~39°), and a tensile strength of 100 Pa (Galland, 2012; Galland et al., 2009).

The model magma consists of Végétaline, a vegetable oil produced in France by Unilever. Végétaline oil is solid at room temperature and melts at ~31°C (Galland et al., 2006). Molten, it is a Newtonian fluid with a weak temperature-dependent viscosity (Galland et al., 2006). Using these materials, a generic experiment consists in injecting oil into the flour to generate an intrusion. At the injection temperature of ~50°C, the oil has a viscosity of 0.02 Pa s and a density of 890 kg m^{-3}. Silica is chemically incompatible with the oil, such that oil percolation within the flour is limited during injection and oil intrusion is dominantly accommodated by

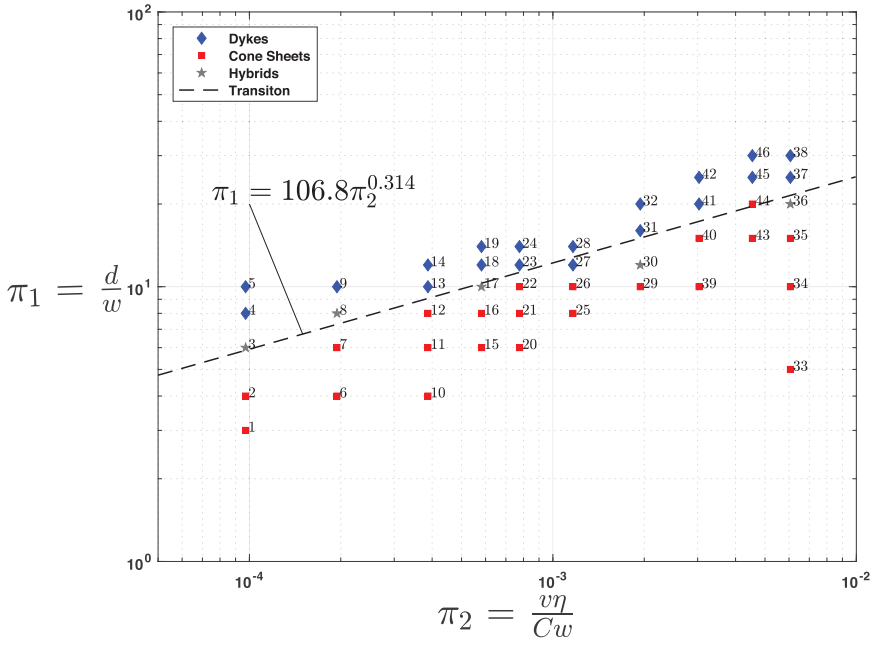

Figure 3. The experiments of Galland et al. (2014) for which surface deformation monitoring was applied. The dimensionless logarithmic plot distinguishes dikes (blue diamonds), cone sheets (red squares), and hybrid intrusions (grey stars). Π_1 is a geometric ratio of depth to width of the inlet. Π_2 is a dynamic ratio including the intruding oil velocity and viscosity divided by the cohesion of flour and width of inlet.

deformation of the flour (Galland et al., 2006). The effects of the cooling of the oil against the flour can be neglected due to the short intrusion durations (less than or up to about 1 min), being much shorter than the rate of cooling.

The suitability of the materials and the scaling of the models are discussed in detail by Galland et al. (2006), Galland et al. (2014), and Galland (2012, see also references therein). In brief, 1 cm in our models represents 100–1000 m in nature; the resulting stress ratio implies that the model crust should be 13×10^3 to 250×10^3 times weaker than its geological prototype (Abdelmalak et al., 2016). The model magma scales assuming that the ratios of viscous stresses in the magma to the cohesion of the host are identical in model and in nature (Galland et al., 2014). Magma velocities have been measured in nature to be on the order of $1–10^{-2}$ m s^{-1}. Our pumping apparatus allow for oil velocities of $10^{-3}–10^{-1}$ m s^{-1}. As magma viscosities cover a wide range ($10–10^7$ Pa s), the corresponding relevant model viscosities must range from 4×10^{-9} to 75 Pa s, which our model magma fulfills. In this scaling, the oil dominantly represents intermediate to felsic magma.

To prepare an experiment, a known mass of silica flour was first poured into a square, 40 cm wide, acrylic glass box with a bottom aluminum plate, to which an inlet was attached. It was then compacted using a high-frequency shaker (Houston Vibrator, model GT-25) to reach a controlled bulk density of 1050 kg m^{-3}. During compaction, a metal plate and a bubble level were placed onto the flour to ensure a flat and horizontal initial upper surface for each model, as well as homogeneous, repeatable experimental initial conditions. Before compaction, a plug was inserted into the inlet to prevent silica flour from clogging the inlet during compaction. The plug was then removed before injecting the oil.

During the experiments, a volumetric pump injected the oil at constant flow rate through the inlet, and a pressure sensor continuously recorded the oil pressure variations at a defined distance below the inlet. As the oil intruded, it triggered subtle surface deformation only in the central region of the box, up to ~15 cm from its lateral walls, enough to assume that boundary effects can be neglected during the experiments. The deformation was periodically monitored using a moiré projection system (Bréque et al., 2004; Galland, 2012). This method produces a time series of digital elevation models (DEMs) of the evolving model surface. It offers a spatial horizontal resolution of <1 mm and a raw elevation precision of ~0.2 mm. Subsequent smoothing of the DEMs improved the vertical accuracy to ~0.1 mm. The duration of a complete scan of the surface of a model was ~1 s, which is assumed to indicate the maximum error on the time at which each DEM was obtained. We have chosen to set the time of each DEM at the beginning of each scan. For the present work, the successive DEMs were captured at temporal steps of 1.5 s. As the durations of most of the experiments lasted up to approximately a minute, the resolution and accuracy of the method are adequate to record temporal evolutions but fail for the few very short experiments that lasted only a few seconds. We used the pressure measurements to limit cumulative errors on timescales. In the generic protocol, the moment at which the oil erupts at the model surface defines both the end of the experiment and of the DEM measurement. The accuracy on the durations of the experiments is <1 s. After an experiment, the oil solidifies for about 45 min, after which the resulting intrusion can be excavated to study its final shape (Figure 2). For some experiments minor oil flow downward along the circular inlet could be observed upon excavation.

3. Surface Deformation Results

Galland et al. (2014) performed 43 experiments for which surface deformation data were captured before, during, and after the oil injection, and among which 18 produced dikes and 19 produced cone sheets. The time series of DEMs show that surface deformation in all the experiments exhibits a common qualitative behavior. At an early stage of the injection, the surface lifts up, forming a gentle (elevation <1 mm), symmetrical dome with a quasi-central zone of maximum uplift (Figure 4a). Then, as injection proceeds, the dome develops a substantial asymmetry mostly marked by a point of maximum uplift that migrates toward the periphery of the uplifted zone (Figures 4b and 4c).

Nevertheless, significant differences can also be extracted from the DEMs, consistently with Galland (2012) , who qualitatively showed that surface deformation patterns evolve as a function of the underlying intrusion geometry. In the following, we systematically compare the surface deformation patterns induced by the formation of experimental dikes to those associated with the cone sheets. To do so, we analyzed, for each

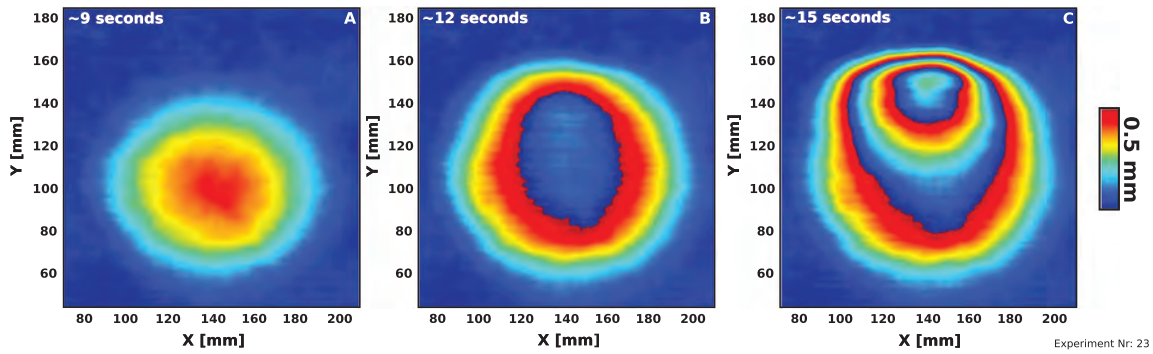

Figure 4. Maps of surface deformation captured for a representative dike experiment at an (a) initial, (b) intermediate, and (c) late stage during oil injection. The uplift has been wrapped in fringes where one fringe corresponds to 0.5 mm of uplift. Formation of a gentle symmetrical dome (Figure 4a) and an asymmetry that initiates amplifies with time (Figures 4b and 4c). The maps show a cropped area limited to the affected uplifted area. The dike was produced using an inlet width of 0.5 cm, a D_i = 6 cm, and an injection velocity of ~80 mL/min.

experiment, the temporal evolution of (1) the maximum uplift (h_m), (2) the uplifted area (A), and (3) the uplifted volume (V_{up}; Figure 5).

Figure 6 displays the evolution of h_m, A, and V_{up} for a representative cone sheet and dike experiment. During cone sheet experiments, h_m generally shows an almost steady, nearly linear increase through time. Conversely, during dike experiments, h_m generally exhibits a two-stage evolution, with an initial phase of moderate uplift, followed by a second stage of rapid uplift prior to eruption. The areal extent of the domed surface, A, exhibits a similar development through both the dike and cone sheet experiments: initially, A increases rapidly and then tends to asymptotically approach a stable value. Similarly, the uplifted volumes V_{up} for both the dike and cone sheet experiments increase linearly during the experiments. These results are consistent with those of Galland (2012).

A difficulty in analyzing raw data is that the experiments are not directly comparable (cf. Figure 6). For instance, the duration of the experiments varied from a few seconds to almost 1 min. Therefore, in order to make direct comparisons, we introduce a dimensionless time $\tau = t/t_e$, where t is the time at a given time step of an experiment and t_e is the duration, that is, the time to the eruption of the same experiment, such that τ may vary from 0 to 1, from the beginning to the end of an experiment. The values of maximum uplift

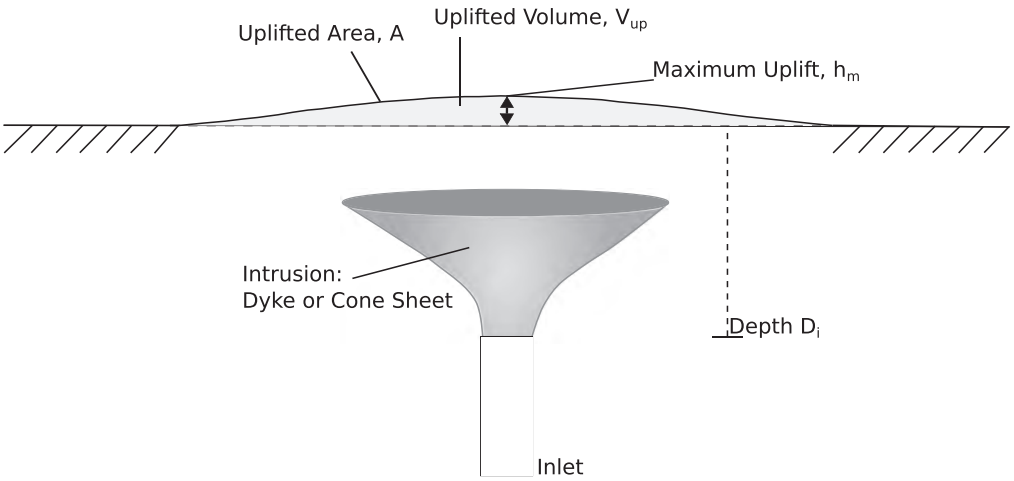

Figure 5. Illustration of the physical parameters used to quantify the surface deformation induced by an intrusion at each time step of an experiment (i.e., each 1.5 s from the beginning of the oil injection). The maximum uplift, h_m, corresponds to the maximum elevation. The uplifted area, A, is quantified as the 2-D projection defined by the largest continuous patch of points uplifted above a threshold value of 0.1 mm from the DEM of the initial horizontal surface. The uplifted volume, V_{up}, integrates the elevations over the uplifted area.

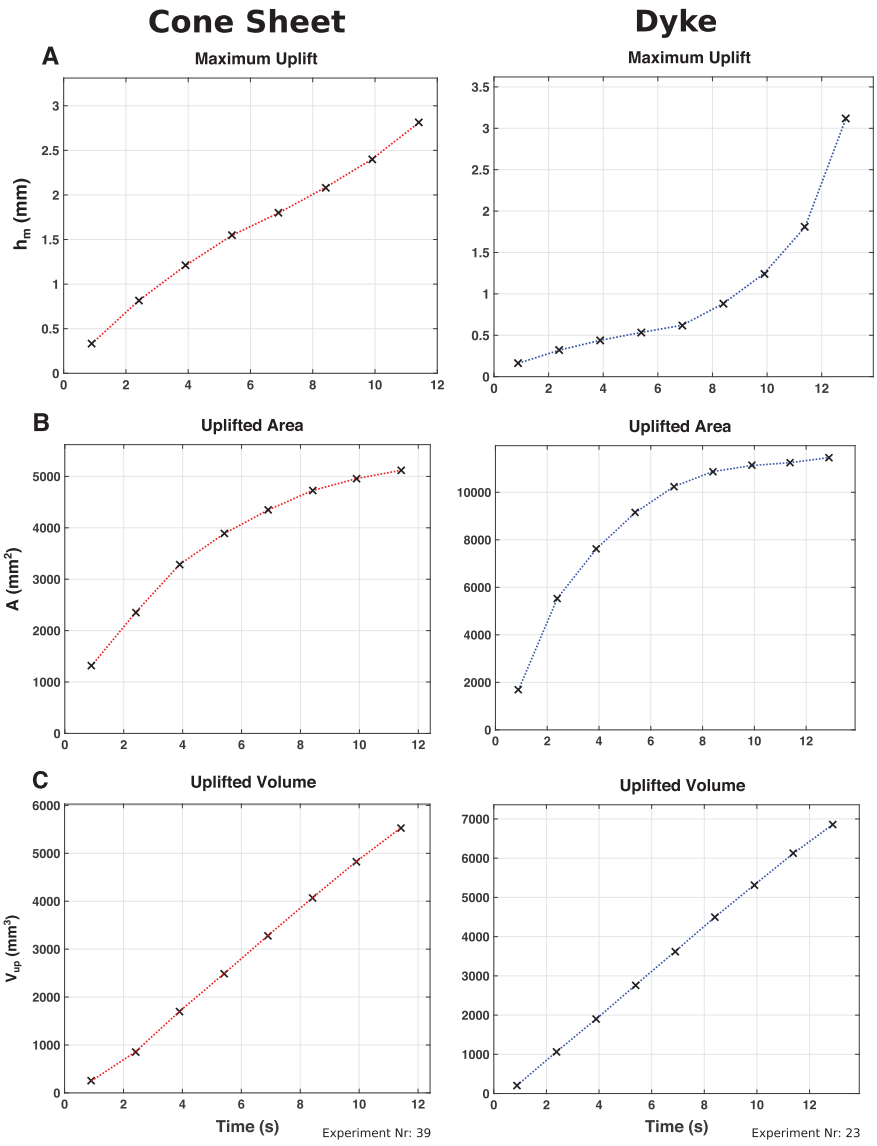

Figure 6. Raw data outputs from the ΔDEMs for (left) a representative cone sheet and (right) a dike experiment. As a function of time the graphs display the development of the (a) maximum uplift, (b) uplifted area, and (c) uplifted volume. The dike was produced using an inlet width of 0.5 cm, a D_i = 6 cm, and an injection velocity of ca 80 mL/min. The cone sheet was produced using an inlet width of 0.2 cm, a D_i = 2 cm, and an injection velocity of ~20 mL/min.

h_m also vary significantly from one experiment to another. Therefore, we also scale the evolution of h_m for each experiment by the final maximum uplift h_f, such that h_m/h_f may vary from 0 (no uplift) to 1 (final uplift).

The relative uplift h_m/h_f as a function of τ for all the experiments shows that dikes and cone sheets display two systematically distinct behaviors (Figure 7). The h_m/h_f for most of the cone sheets shows a relatively rapid initial increase, a subsequent gentle deceleration, followed by an almost linear increase of h_m/h_f from $\tau \sim 0.2$ until the eruption. Dike experiments instead show that h_m/h_f exhibits an initial moderate to low increase that suddenly accelerates from τ of about 0.5–0.8. The exception is one dike experiment that peaks immediately before eruption. However, unlike the other dike models, large open fractures developed at the surface of this experiment before the oil erupted.

Relevant scaling is also useful to analyze the temporal evolution of the uplifted area, *A*. According to the theoretical models of Mogi (1958) and Sun (1969), among others, the radius of an uplifted area that is associated

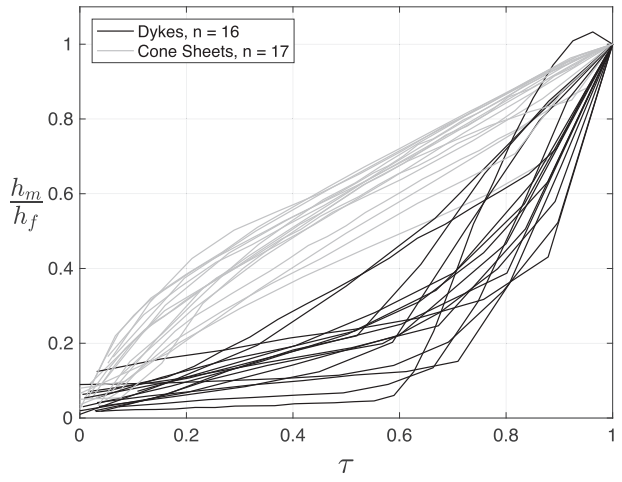

Figure 7. Plot of the normalized maximum uplifts versus dimensionless time for 18 of the cone sheet (gray) and 17 of the dike (black) experiments. The shortest experiments, for which less than five differential digital elevation models (ΔDEMs) are available, are not shown. Two end-member behavioral regimes can be distinguished. After an initial rapid increase that slows down, most of the maximum uplift above cone sheets develops gradually and quasi-linearly. In contrast, the maximum uplift above dikes exhibits a more pronounced two-phase evolution with an initial slow increase that suddenly accelerates from about the half, or more, of the experiment duration.

with the inflation of a deep magma source is proportional to the depth of the source. Therefore, we scaled A by D_i^2 (Figure 8). The evolution of A/D_i^2 for the dike and cone sheet experiments exhibits similar shapes (see also Figure 6). However, the obtained values of A/D_i^2 are usually larger for cone sheets than for dikes, illustrating that the scaled uplifted area is generally larger above cone sheets than above dikes.

A different approach is used to scale the uplifted volume. Since the oil is injected at a constant flow rate, the volume of injected oil through time V_{inj} can be calculated. Therefore, we defined the ratio $\Delta V/V_{inj} = (V_{up} - V_{inj})/V_{inj}$, which is the difference in uplifted volume versus injected volume scaled by the injected volume. This ratio quantifies to what extent that the deformation due to the volume of injected oil is accommodated by an uplift of the model surface. The $\Delta V/V_{inj} = 0$ implies that the flour only deforms by uplift of its surface as a result of the oil intrusion, whereas $\Delta V/V_{inj} = -1$ indicate no uplift, that is, that the oil intrusion is only accommodated by deformation of the flour at depth. Our results show that the obtained values of $\Delta V/V_{inj}$ are generally larger for the cone sheets (from ~0 to ~ −0.6, −0.3 on average) than for the dikes (from ~ −0.2 to ~ −1, −0.7 on average; Figure 9). This difference indicates that the intrusion of cone sheets dominantly induces surface uplift as a response to the oil intrusion, whereas dikes more likely induce internal deformation of the flour with moderate surface uplift relative to the quantity of injected oil. Nevertheless, several values of $\Delta V/V_{inj}$ overlap for dikes and cone sheets.

During oil intrusion in all the experiments, surface deformation progressively develops an asymmetry (Figures 4 and 10). When a dike forms, the uplifted area is initially symmetrical, and the uplift is of relatively low amplitude. Subsequently, an asymmetric uplift initiates from one side of the uplifted area, and most of the uplift focuses at a bulge that moves to the margin of the uplifted areas (Figure 10b). In the cone sheet experiments, the initial uplifted area is also symmetrical. However, in contrast with the dikes, asymmetry develops gradually (Figure 10c).

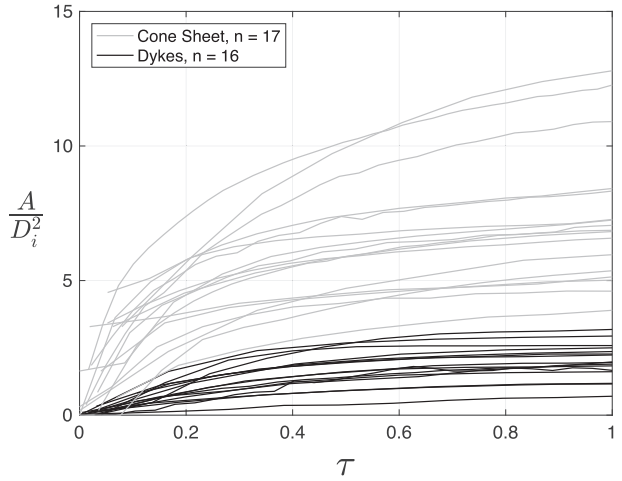

Figure 8. Plots of the uplifted area scaled by the square of the oil source depths versus normalized time for the cone sheet (gray) and dike (black) experiments (the shortest dike experiment lasting for less than five time steps is not shown). The cone sheets generally result in a larger scaled uplifted area than dikes.

To quantify the asymmetrical development of the surface deformation patterns associated with dikes and cone sheets, we defined the center of the uplifted area and calculated the distances between the center and each pixel of the uplifted area at each time step. This allows for plotting the global distribution of the uplift as a function of the distance to the center of the uplifted area for all time steps of the experiments (Figure 11). For both the dike and cone sheet experiments, the data exhibit very little dispersion at the first time steps, illustrating that the uplifted areas are symmetrical. For the next time steps the data show more dispersion, indicating that the uplifted areas become asymmetrical. For the ultimate time steps, the asymmetries are distinctive for dike and cone sheet experiments. The distribution of the data for the dike experiments shows a local development of most of the uplift, compared to a more distributed overall uplift characterizing the cone sheets.

At each time step of each experiment, we computed the averaged distribution of the uplift (Figure 11), representing the distribution for a virtual ideally symmetrical uplifted area. Then we calculated the standard deviation, σ, from the virtual symmetrical profile over the entire distribution for each time step. Small σ values indicate a low dispersion of the uplifts and a rather symmetrical uplifted area

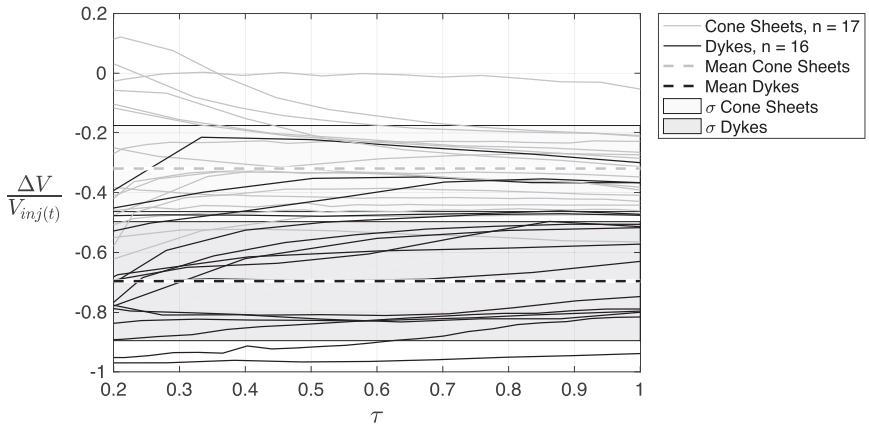

Figure 9. Ratio of uplifted volume minus the injected oil volume normalized by the injected volume versus the dimensionless time for cone sheet (gray) and dike (black) experiments. The shortest experiments are not shown. The dashed lines indicate the respective means and the shaded areas the respective standard deviation, σ. Some of the dikes induce very weak surface deformation relative to the volume of injected. In contrast, for some of the cone sheets, the uplifted volume roughly corresponds to the injected volume. Initial time steps are omitted because of amplified noise due to scaling.

(Figure 11, top row), whereas large σ values indicate high dispersion with a substantial asymmetry of the uplifted area (Figure 11, bottom row).

To compare the experiments, we scale the σ values at each time step by the value σ_f obtained for the final time step of each experiment. Figure 12 displays the temporal evolutions of σ/σ_f for most of the experiments.

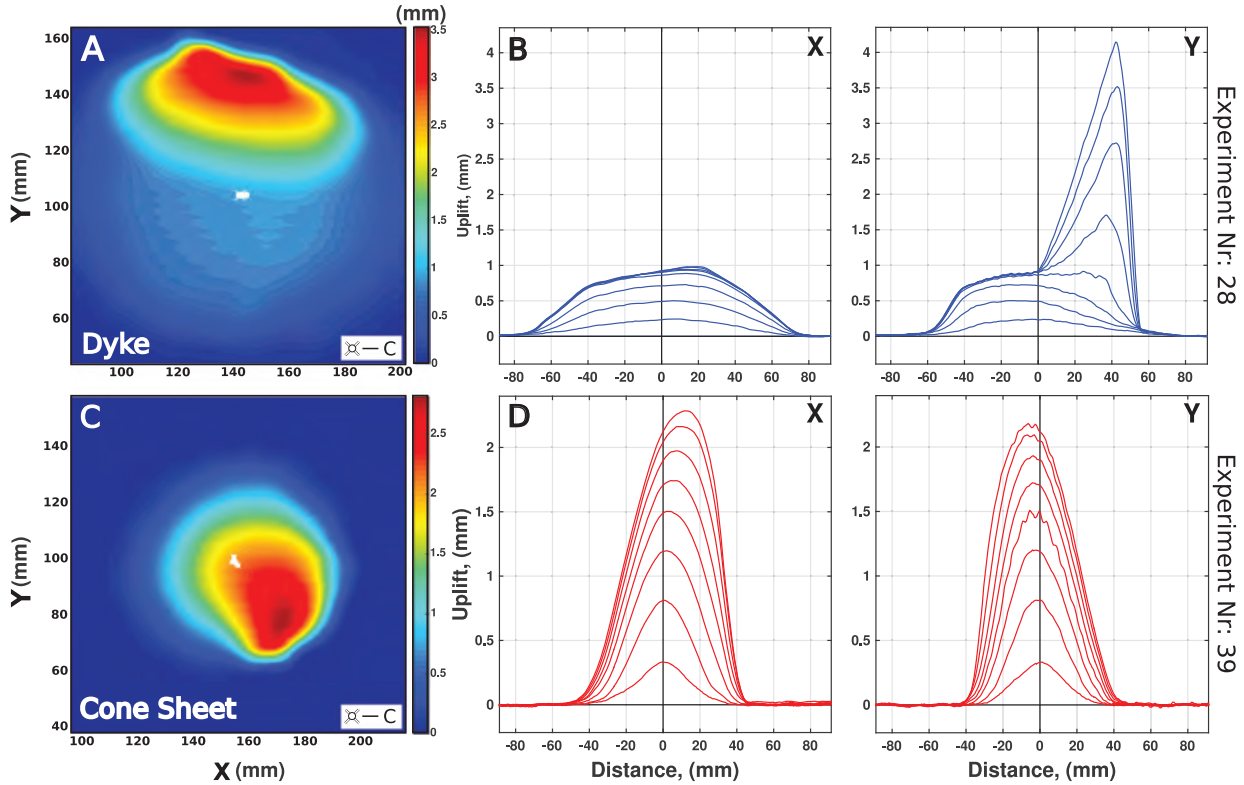

Figure 10. (a and c) Maps of the final surface elevations observed for a representative dike and a cone sheet experiment. The white crosses locate the mean centers (C) of the uplifted area at each time step during the experiments. (b and d) Successive profiles along the (left) *x* and (right) *y* reference directions and passing through the centers C at each time step for the corresponding experiments: dike (Figure 10b) and cone sheet (Figure 10d). Maps and profiles show a cropped area limited to the affected uplifted area. The dike was produced using an inlet width of 0.5 cm, a $D_i = 7$ cm, and an injection velocity of ~120 mL/min. The cone sheet was produced using an inlet width of 0.2 cm, a $D_i = 2$ cm, and an injection velocity of ~20 mL/min.

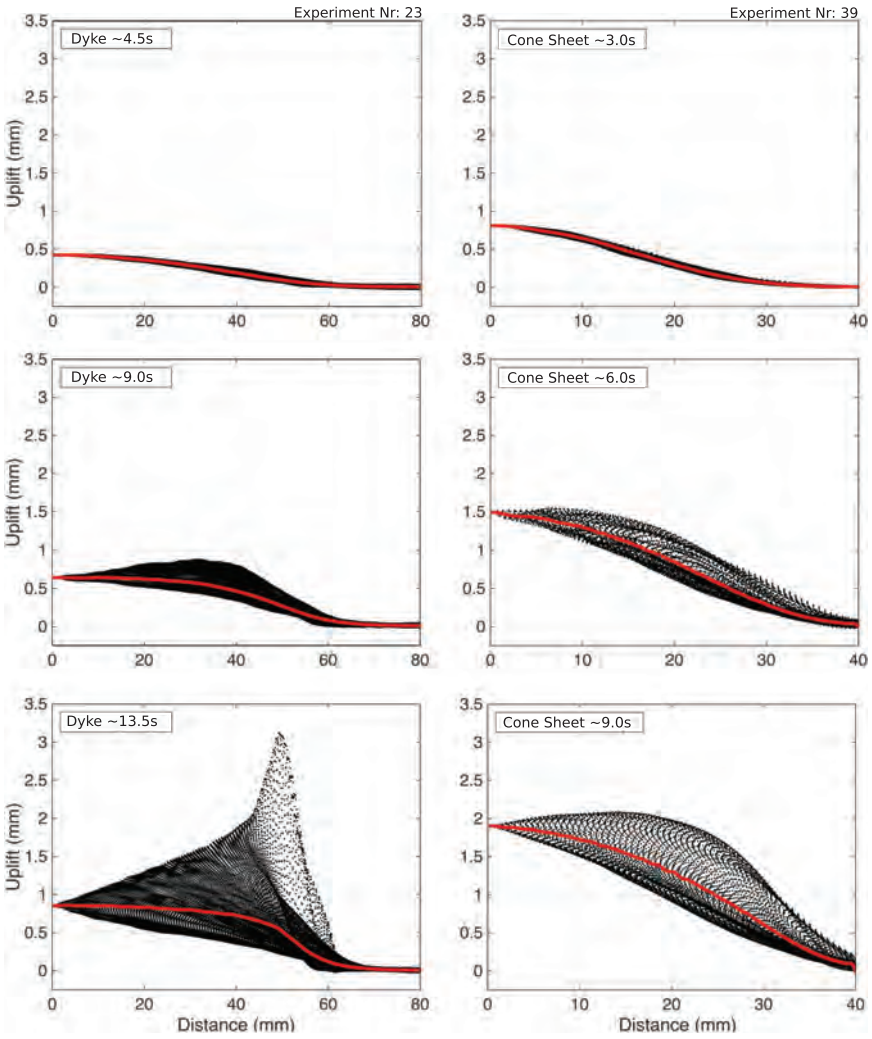

Figure 11. Plots of the observed uplift as a function of the distance to the center of the uplifted area for (left column) a dike and (right column) a cone sheet experiment, at early, intermediate, and late time steps. The red line corresponds to the mean distribution of the uplifts, representative of an ideal symmetrical dome, from which a residual standard deviation is calculated to quantify the degree of asymmetry at each time step for each experiment. The dike was produced using an inlet width of 0.5 cm, a D_i = 6 cm, and an injection velocity of ~80 mL/min. The cone sheet was produced using an inlet width of 0.2 cm, a D_i = 2 cm, and an injection velocity of ~20 mL/min.

Cone sheet and dike experiments again exhibit distinct behaviors. For most cone sheets, a nearly linear increase of σ/σ_f occurs from $\tau > 0.2$ (Figure 12). In all cases, the asymmetry of the uplifted area develops gradually from the early stages of the intrusions. In contrast, for most of the dikes σ/σ_f remains very low until τ reaches about 0.5 to 0.7, values from which σ/σ_f rapidly increases. For dikes, the uplifted area remains relatively symmetrical until at least half of the experiment duration, followed by the development of a significant asymmetry prior to the eruption.

4. Interpretation and Discussion

4.1. Interpretation

The distinct gradual or two-phase development of h_m/h_f (Figure 7) and σ/σ_f (Figure 12) for cone sheets and dikes, respectively, correlates with the final shapes of the underlying intrusions described by Galland et al. (2014). The surface deformation associated with cone sheets exhibits a gradual, almost

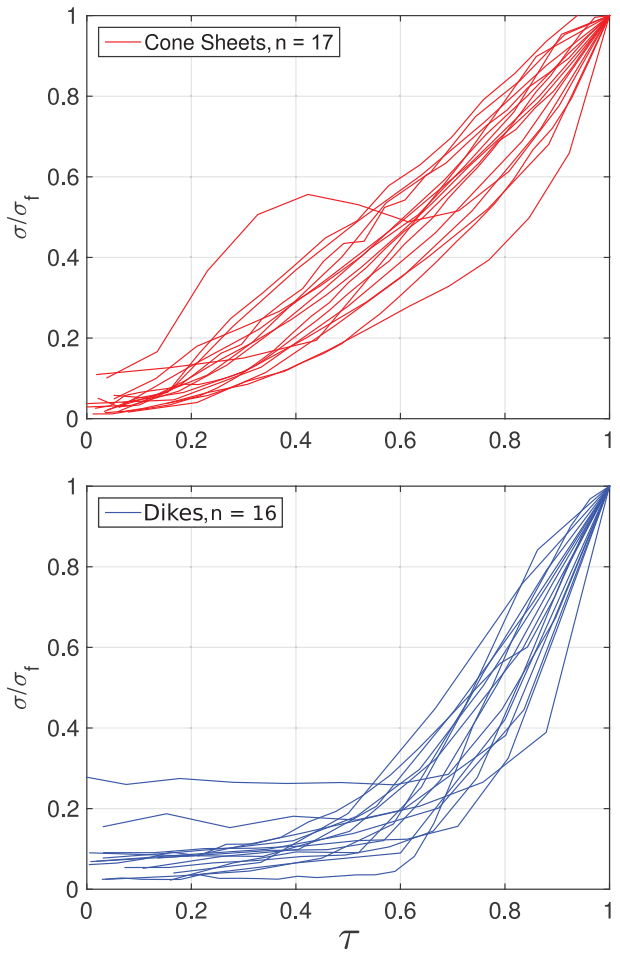

Figure 12. Standard deviation of the observed uplift normalized to the final standard deviation of the uplift versus dimensionless time, for (top) 17 cone sheet (red) and (bottom) 16 dike (blue) experiments. Only experiments with more than four time steps have been plotted. Two dominating trends emerge; cone sheets gradually develop while dikes display a two-stage evolution.

continuous evolution, whereas that of dikes is clearly two-phase, with a first symmetrical, low-amplitude uplift followed by a second phase of asymmetrical, rapid localized uplift. In addition, the excavated dikes often displayed either an inclined sheet or a hull-shaped termination just below the model surface, and above the underlying subvertical main dike (Galland et al., 2014). Such dike shapes are interpreted as resulting from two successive intrusion regimes, as illustrated by the emplacement of an initial, deep subvertical dike, the tip of which bifurcates or splits at a critical depth to form either the inclined sheet or hull-shaped intrusion. It is thus inferred that the two-stage evolution of the dike surface deformation may correlate with such a two-stage evolution. Such a hypothesis is in good agreement with the two-dimensional experiments of Mathieu et al. (2008) and Abdelmalak et al. (2012), who showed that the shallow splitting of a propagating dike tip induces both uplift acceleration and asymmetry. Similar behaviors have also been observed in fluid pipes (aka sand injectites; Mourgues et al., 2012) and conduits of fluids propagating from depth within the oceanic crust to the seafloor (Gay et al., 2012). Similar two-stage behavior associated with a shallow dike-to-sill transition has been inferred in the Afar rift (Magee et al., 2017; Pagli et al., 2012). Conversely, the gradual and sublinear evolution of surface deformation associated with cone sheet emplacement is likely the result of the continuous emplacement during a single regime of sheet intrusion growing gradually from the inlet.

The overall patterns of evolution of the uplifted area and volume are similar for both intrusion types (Figures 8 and 9). However, relative to the inlet depth, D_i, cone sheets generate larger uplifted areas than dikes. Similarly, the ratio $\Delta V/V_{inj}$ reaches much larger values for cone sheets than for dikes, indicating that the deformation due to cone sheet emplacement is mostly accommodated by uplift, in contrast to that due to most of the dikes. We thus infer from these results that cone sheets dominantly push their overburden upward, which is consistent with the current understanding of the formation of cone sheets (Burchardt et al., 2013; Klausen, 2004; Kuenen, 1937; Mathieu et al., 2008). This is in agreement with Galland et al. (2014), who showed that cone sheets preferentially form when the magmatic source exhibits a low depth-to-size ratio, that is, when it is shallow compared to its size. For dikes, our results suggest that the propagation is less influenced by the presence of a free surface, except in the second regime at shallow depth where the dike tip bifurcates or splits to form hull-shaped intrusions or inclined sheets. This is also consistent with the current understanding of the dike emplacement mechanics, in which deformation is thought to be dominantly accommodated by lateral pushing of the vertical walls, with a minor component of upward pushing (Abdelmalak et al., 2012; Kavanagh, Boutelier, & Cruden, 2015). This is also in agreement with Galland et al. (2014), who showed that dikes preferentially form when the magmatic source is deep compared to its size, and exhibits a high depth-to-size ratio (Figure 3). Deciphering between contrasting mechanisms could be possible through extracting horizontal surface displacements (e.g., Galland et al., 2016). However, the moiré projection monitoring system does not allow for quantification of the vertical and horizontal displacements separately.

Notably, the evolution of the overall asymmetry of uplift σ/σ_f (Figure 12) exhibits similar patterns to those shown by the evolution of h_m/h_f (Figure 7). This similarity suggests that the overall asymmetry of the surface uplift pattern is dominantly controlled by the behavior of the maximum uplift. It implies that tracking only the evolution of maximum uplifts is a good first-order indicator of the overall asymmetrical development of surface uplift patterns.

4.2. Discussion

The silica flour used in our experiments is a cohesive Coulomb material, which allows for both mode I and mode II fracturing, similar to natural rocks (Abdelmalak et al., 2016; Jaeger, Cook, & Zimmerman, 2009; Pollard, 1973). The cohesion, tensile strength, and friction coefficient of the silica flour can be measured easily and compared to those of natural rocks (Abdelmalak et al., 2016; Galland et al., 2006). Additionally, cohesive flours have the ability to stand nonnegligible elastic stresses along stable vertical walls (see Abdelmalak et al., 2016 and Figure S1 in the supporting information). In allowing for elasto-plastic deformation of the host, the experiments using flour show a major difference compared with laboratory models using elastic gelatine (e.g., Kavanagh, Menand, & Sparks, 2006; Rivalta & Dahm, 2006; Taisne & Jaupart, 2009; Takada, 1990, 1994; Tibaldi, Bonali, & Corazzato, 2014), most theoretical and numerical models (e.g., Galland & Scheibert, 2013; Maccaferri, Bonafede, & Rivalta, 2010; Pollard, 1987), and many geodetic models used to analyze surface deformation measured at active volcanoes, which assume purely elastic host (e.g., Mogi, 1958; Okada, 1985). However, the elastic properties of our silica flour are poorly constrained, which is also true for flours, in general. It is therefore challenging to decipher the elastic versus inelastic deformation due to intrusion in our models. In addition, compared to natural cases of intrusions, other features that our models do not account for include (1) host-rock heterogeneities, (2) topography (i.e., the model surface was flat), and (3) far field (i.e., tectonic) stresses.

Our results show that intrusion-induced deformation in our experimental cohesive Coulomb models is significantly affected by inelastic deformation, that is, shear failure. In contrast, established models of sheet intrusion propagation and geodetic models account for purely elastic deformation of the host rock. However, natural rocks are neither purely elastic nor purely Coulomb solids but are rather elasto-plastic materials (Gudmundsson, 2011; Jaeger et al., 2009), and one would expect that both deformation mechanisms are at work during magma propagation and emplacement. Even if the literature suggests (cf. Rubin, 1995) that inelastic deformation occurs during magma emplacement, a recurrent argument states that it is constrained to such a small volume near the dike tip that it can be assumed to have a negligible effect on propagation (Rubin, 1993). Nevertheless, recent field (Gudmundsson et al., 2008; Spacapan et al., 2017) and geophysical (Ágústsdóttir et al., 2016; White et al., 2011) observations of tip deformation demonstrate that shear failure significantly contributes to the propagation of sills and dikes, respectively. A relevant question is thus whether the local shear deformation at the intrusion tip significantly affects the overall deformation of the host rock.

In all the models of this study, the surface deformation accommodating magma emplacement occurred through surface uplifts regardless of the intrusion shape, including subvertical dikes. This is a major difference with elastic models of dike opening (e.g., Okada, 1985; Pollard & Holzhausen, 1979), which predict a local trough, that is, surface subsidence, above the dike tip. We interpret the different surface deformation patterns in terms of contrasting subsurface host deformation modes; in our models the silica flour is expected to fail through the formation of shear fractures induced by the flow of the viscous vegetable oil (Abdelmalak et al., 2012; Donnadieu & Merle, 1998; Mathieu et al., 2008). This mechanism, the so-called *viscous indenter*, implies that the magma creates its own space by pushing the host rock ahead of the intrusion tip, resulting in surface uplift. Natural examples supporting this mode of propagation involve intruding magma of probable andesitic composition, that is, magma with relatively high viscosities (Spacapan et al., 2017). In this specific example, the intrusions appear to have propagated by pushing the host rocks ahead and the dike tips exhibit blunt or rectangular shapes. This is in stark contrast with the sharp, narrow tips expected for tensile elastic fractures (Figure 13). The blunting of an intrusion tip likely occurs when the host rock exhibits an elasto-plastic rheology, as demonstrated by Vachon and Hieronymus (2016). These observations thus validate the geological relevance of a propagation mechanism where a dike pushes its host rock ahead causing it to fail in shear, such as the *viscous indenter* mechanism, and so the use of cohesive silica flour in our experiments.

Our dike experiments initially display smooth dome-shaped surface uplift. Similar surface deformation has been recorded at Piton de la Fournaise volcano, Réunion Island (e.g., Cayol & Cornet, 1998; Froger et al., 2004; Toutain et al., 1992) and Galapagos (e.g., Amelung et al., 2000; Bagnardi, Amelung, & Poland, 2013). Mogi (1958) or inflating sill (e.g., Horizontal Okada) models are commonly used to fit such data. Our experimental results thus provide an alternative mechanism of surface uplift associated with the emplacement of a vertical dike through a Coulomb brittle crust.

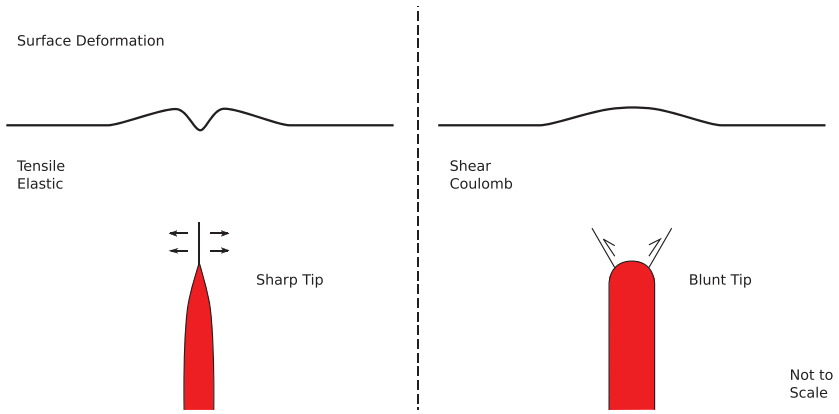

Figure 13. Profiles of conceptual surface deformation predicted by (left) a tensile elastic fracture compared to the surface deformation above (right) a subvertical sheet intrusion propagating due to shear failure in a Coulomb material.

The surface deformation associated with dike emplacement in rift zones often display two bulges and a trough parallel to an underlying dike (Figure 13). Such deformation has been monitored at Krafla, Iceland (e.g., Hollingsworth et al., 2012); Afar (e.g., Grandin et al., 2010; Wright et al., 2012); and at the Harrat Lunayyir basaltic field, Saudi Arabia (Pallister et al., 2010). Because such surface deformation is compatible with the elastic deformation expected from the Okada source model, the Okada (1985) model is commonly used to model surface deformation patterns associated with dike emplacement in rifts. However, the Okada source model's far-field stress boundary conditions do not account for regional tectonic extension, which is clearly at work in active rift zones. This discrepancy between boundary conditions in active rifts and in the Okada model questions whether the observed subsidence during rifting episodes is triggered by the emplacement of the dike or by regional extensional tectonics.

Finally, our models and their proposed interpretations are mostly relevant for volcanic systems where (1) the magma viscosity is relatively high, that is, andesitic to rhyolitic compositions, and/or (2) the host rock is composed of relatively weak, poorly consolidated rocks, such as tephra or tuff, which are common in differentiated volcanic systems, and/or tuffites or poorly consolidated sedimentary rocks, which are common host rocks to volcanic plumbing systems emplaced in sedimentary basins (e.g., Spacapan et al., 2017). Thus, our model and modeled uplifts may not apply to all geological settings.

5. Conclusion

This paper describes the systematic analysis of surface deformation patterns induced by the emplacement of dikes and cone sheets into a cohesive, Coulomb brittle crust. The data come from 43 experiments of the experimental series presented by Galland et al. (2014), who performed a systematic parameter study identifying the conditions at which dikes and cone sheets preferentially form, in simulating the intrusion of relatively viscous magma into a relatively weak host at shallow depth. The main conclusions from our study are the following:

1. Both the emplacement of dikes and cone sheets induce surface uplift.
2. Uplift associated with cone sheet emplacement is higher than that associated with dike emplacement. Cone sheets, which generally initiate at shallower depth, dominantly push their host upward while the deeper dikes emplace through lateral opening of their host.
3. The evolution of surface deformation patterns associated with dike and cone sheet emplacement exhibits systematic, distinct signatures.
4. Cone sheet emplacement induces a gradual, quasi-linear uplift; the initial uplift shows a symmetrical bell-shaped pattern, which gradually develops an asymmetry until eruption.
5. Conversely, dike emplacement induces two-stage surface uplift; the initial uplift is low, and the uplift pattern remains symmetrical; at shallower depth (about halfway through the experiment duration), uplift suddenly increases and grows rapidly, developing a strongly asymmetrical uplift pattern.

6. All the experimental dikes induced uplift, and no subsidence of the surface above the dikes was observed, in contrast with the predictions of common elastic models.
7. The Coulomb behavior of the Earth's brittle crust may significantly affect the surface deformation patterns of shallow intrusions.
8. The temporal evolution of the maximum uplift can be used as a proxy for the overall development of surface deformation.

Our laboratory results suggest that it may be necessary to account for the Coulomb brittle behavior of the Earth's crust to satisfactorily interpret geodetic measurements associated with shallow magma intrusions.

Acknowledgments
Guldstrand's position is funded by the DIPS project (grant 240467) from the Norwegian Research Council. Burchardt acknowledges financial support from V. R. Troll, Uppsala University, the Swedish Research Council for a research visit to PGP. Hallot acknowledges his welcome to PGP for several weeks, thanks to a half-year sabbatical, teaching-free CRCT from Université de Rennes 1. The data analysis was performed in the framework of an exchange visiting grant (grant 4251) through the MeMoVolc Networking Programme, funded by the European Science Foundation. The data are available here: https://doi.org/10.5281/zenodo.898692. We acknowledge the constructive reviews of Claudia Corrazato, Mike Poland, an anonymous reviewer, and the Associate Editor of JGR: Solid Earth, which greatly improved the manuscript. Guldstrand would like to acknowledge Fanny Bjugger for assistance in laboratory work and in discussions. Guldstrand would also like to acknowledge the Volcano Plumbing Systems group at PGP, University of Oslo, for fruitful, enthusiastic, and stimulating discussions.

References

Abdelmalak, M., Bulois, C., Mourgues, R., Galland, O., Legland, J.-B., & Gruber, C. (2016). Description of new dry granular materials of variable cohesion and friction coefficient: Implications for laboratory modeling of the brittle crust. *Tectonophysics*, *684*, 39–51. https://doi.org/10.1016/j.tecto.2016.03.003

Abdelmalak, M., Mourgues, R., Galland, O., & Bureau, D. (2012). Fracture mode analysis and related surface deformation during dyke intrusion: Results from 2D experimental modelling. *Earth and Planetary Science Letters*, *359*, 93–105.

Ágústsdóttir, T., Woods, J., Greenfield, T., Green, R. G., White, R. S., Winder, T., … Soosalu, H. (2016). Strike-slip faulting during the 2014 Bárðarbunga-Holuhraun dike intrusion, central Iceland. *Geophysical Research Letters*, *43*, 1495–1503. https://doi.org/10.1002/2015GL067423

Amelung, F., Jónsson, S., Zebker, H., & Segall, P. (2000). Widespread uplift and 'trapdoor' faulting on Galapagos volcanoes observed with radar interferometry. *Nature*, *407*(6807), 993–996.

Bagnardi, M., Amelung, F., & Poland, M. P. (2013). A new model for the growth of basaltic shields based on deformation of Fernandina volcano, Galápagos Islands. *Earth and Planetary Science Letters*, *377*, 358–366.

Bréque, C., Dupre, J.-C., & Bremand, F. (2004). Calibration of a system of projection moiré for relief measuring: Biomechanical applications. *Optics and Lasers in Engineering*, *41*(2), 241–260.

Burchardt, S., Troll, V. R., Mathieu, L., Emeleus, H. C., & Donaldson, C. H. (2013). Ardnamurchan 3D cone-sheet architecture explained by a single elongate magma chamber. *Scientific Reports*, *3*, 2891.

Cayol, V., & Cornet, F. H. (1998). Three-dimensional modeling of the 1983–1984 eruption at Piton de la Fournaise Volcano, Réunion Island. *Journal of Geophysical Research*, *103*(B8), 18,025–18,037.

Chadwick, W. W., Jónsson, S., Geist, D. J., Poland, M., Johnson, D. J., Batt, S., … Ruiz, A. (2011). The May 2005 eruption of Fernandina volcano, Galápagos: The first circumferential dike intrusion observed by GPS and InSAR. *Bulletin of Volcanology*, *73*(6), 679–697.

Donnadieu, F., & Merle, O. (1998). Experiments on the indentation process during cryptodome intrusions: New insights into Mount St. Helens deformation. *Geology*, *26*(1), 79–82.

Dzurisin, D. (2006). *Volcano Deformation: New Geodetic Monitoring Techniques*. Chichester, UK: Springer Science & Business Media.

Froger, J. L., Fukushima, Y., Briole, P., Staudacher, T., Souriot, T., & Villeneuve, N. (2004). The deformation field of the August 2003 eruption at Piton de la Fournaise, Reunion Island, mapped by ASAR interferometry. *Geophysical Research Letters*, *31*, L14601. https://doi.org/10.1029/2004GL020479

Galland, O. (2012). Experimental modelling of ground deformation associated with shallow magma intrusions. *Earth and Planetary Science Letters*, *317*, 145–156.

Galland, O., & Scheibert, J. (2013). Analytical model of surface uplift above axisymmetric flat-lying magma intrusions: Implications for sill emplacement and geodesy. *Journal of Volcanology and Geothermal Research*, *253*, 114–130.

Galland, O., Bertelsen, H. S., Guldstrand, F., Girod, L., Johannessen, R. F., Bjugger, F., … Mair, K. (2016). Application of open-source photogrammetric software MicMac for monitoring surface deformation in laboratory models. *Journal of Geophysical Research: Solid Earth*, *121*, 2852–2872. https://doi.org/10.1002/2015JB012564

Galland, O., Burchardt, S., Hallot, E., Mourgues, R., & Bulois, C. (2014). Dynamics of dikes versus cone sheets in volcanic systems. *Journal of Geophysical Research: Solid Earth*, *119*, 6178–6192. https://doi.org/10.1002/2014JB011059

Galland, O., Cobbold, P. R., Hallot, E., de Bremond d'Ars, J., & Delavaud, G. (2006). Use of vegetable oil and silica powder for scale modelling of magmatic intrusion in a deforming brittle crust. *Earth and Planetary Science Letters*, *243*(3), 786–804.

Galland, O., Planke, S., Neumann, E.-R., & Malthe-Sørenssen, A. (2009). Experimental modelling of shallow magma emplacement: Application to saucer-shaped intrusions. *Earth and Planetary Science Letters*, *277*(3), 373–383.

Gay, A., Mourgues, R., Berndt, C., Bureau, D., Planke, S., Laurent, D., … Loggia, D. (2012). Anatomy of a fluid pipe in the Norway Basin: Initiation, propagation and 3D shape. *Marine Geology*, *332*, 75–88.

Grandin, R., Socquet, A., Jacques, E., Mazzoni, N., de Chabalier, J. B., & King, G. (2010). Sequence of rifting in Afar, Manda-Hararo rift, Ethiopia, 2005–2009: Time-space evolution and interactions between dikes from interferometric synthetic aperture radar and static stress change modeling. *Journal of Geophysical Research*, *115*, B10413. https://doi.org/10.1029/2009JB000815

Gudmundsson, A. (2011). *Rock Fractures in Geological Processes*. Cambridge, UK: Cambridge University Press.

Gudmundsson, A., Friese, N., Galindo, I., & Philipp, S. L. (2008). Dike-induced reverse faulting in a graben. *Geology*, *36*(2), 123–126.

Haug, Ø. T., Galland, O., Souloumiac, P., Souche, A., Guldstrand, F., & Schmiedel, T. (2017). Inelastic damage as a mechanical precursor for the emplacement of saucer-shaped intrusions. *Geology*. https://doi.org/10.1130/G39361.1

Hollingsworth, J., Leprince, S., Ayoub, F., & Avouac, J. P. (2012). Deformation during the 1975–1984 Krafla rifting crisis, NE Iceland, measured from historical optical imagery. *Journal of Geophysical Research*, *117*, B11407. https://doi.org/10.1029/2012JB009140

Jaeger, J. C., Cook, N. G., & Zimmerman, R. (2009). *Fundamentals of Rock Mechanics*. Malden, MA: John Wiley & Sons.

Kavanagh, J., Boutelier, D., & Cruden, A. (2015). The mechanics of sill inception, propagation and growth: Experimental evidence for rapid reduction in magmatic overpressure. *Earth and Planetary Science Letters*, *421*, 117–128.

Kavanagh, J. L., Menand, T., & Sparks, R. S. J. (2006). An experimental investigation of sill formation and propagation in layered elastic media. *Earth and Planetary Science Letters*, *245*(3), 799–813.

Klausen, M. (2004). Geometry and mode of emplacement of the Thverartindur cone sheet swarm, SE Iceland. *Journal of Volcanology and Geothermal Research*, *138*(3), 185–204.

Kuenen, P. H. (1937). Intrusion of cone-sheets. *Geological Magazine*, *74*, 177–183.
Maccaferri, F., Bonafede, M., & Rivalta, E. (2010). A numerical model of dyke propagation in layered elastic media. *Geophysical Journal International*, *180*(3), 1107–1123.
Magee, C., Bastow, I. D., de Vries, B. V. W., Jackson, C. A.-L., Hetherington, R., Hagos, M., & Hoggett, M. (2017). Structure and dynamics of surface uplift induced by incremental sill emplacement. *Geology*, *45*(5), 431–434.
Mathieu, L., de Vries, B. V. W., Holohan, E. P., & Troll, V. R. (2008). Dykes, cups, saucers and sills: Analogue experiments on magma intrusion into brittle rocks. *Earth and Planetary Science Letters*, *271*(1), 1–13.
Mogi, K. (1958). Relations between the eruptions of various volcanoes and the deformations of the ground surfaces around them. *Bulletin of the Earthquake Research Institute*, *36*, 99–134.
Mourgues, R., Bureau, D., Bodet, L., Gay, A., & Gressier, J. (2012). Formation of conical fractures in sedimentary basins: Experiments involving pore fluids and implications for sandstone intrusion mechanisms. *Earth and Planetary Science Letters*, *313*, 67–78.
Okada, Y. (1985). Surface deformation due to shear and tensile faults in a half-space. *Bulletin of the Seismological Society of America*, *75*(4), 1135–1154.
Pagli, C., Wright, T. J., Ebinger, C. J., Yun, S.-H., Cann, J. R., Barnie, T., & Ayele, A. (2012). Shallow axial magma chamber at the slow-spreading Erta Ale Ridge. *Nature Geoscience*, *5*(4), 284.
Pallister, J. S., McCausland, W. A., Jónsson, S., Lu, Z., Zahran, H. M., El Hadidy, S., … White, R. A. (2010). Broad accommodation of rift-related extension recorded by dyke intrusion in Saudi Arabia. *Nature Geoscience*, *3*(10), 705–712.
Pollard, D. D. (1973). Derivation and evaluation of a mechanical model for sheet intrusions. *Tectonophysics*, *19*(3), 233–269.
Pollard, D. D. (1987). Elementary fracture mechanics applied to the structural interpretation of dykes, In H. C. Halls & W. F. Fahrig (Eds.), *Mafic Dyke Swarms, Geological Association of Canada Special Paper* (Vol. 34, pp. 5–24).
Pollard, D. D., & Holzhausen, G. (1979). On the mechanical interaction between a fluid-filled fracture and the Earth's surface. *Tectonophysics*, *53*(1–2), 27–57.
Rivalta, E., & Dahm, T. (2006). Acceleration of buoyancy-driven fractures and magmatic dikes beneath the free surface. *Geophysical Journal International*, *166*(3), 1424–1439.
Rubin, A. M. (1993). Tensile fracture of rock at high confining pressure: Implications for dike propagation. *Journal of Geophysical Research*, *98*(B9), 15,919–15,935.
Rubin, A. M. (1995). Propagation of magma-filled cracks. *Annual Review of Earth and Planetary Sciences*, *23*, 287–336.
Scheibert, J., Galland, O., & Hafver, A. (2017). Inelastic deformation during sill and laccolith emplacement: Insights from an analytic elasto-plastic model. *Journal of Geophysical Research: Solid Earth*, *122*, 923–945. https://doi.org/10.1002/2016JB013754
Sigmundsson, F., Hooper, A., Hreinsdóttir, S., Vogfjörd, K. S., Ófeigsson, B. G., Heimisson, E. R., … Gudmundsson, G. B. (2015). Segmented lateral dyke growth in a rifting event at Bar [eth] arbunga volcanic system, Iceland. *Nature*, *517*(7533), 191–195.
Spacapan, J. B., Galland, O., Leanza, H. A., & Planke, S. (2017). Igneous sill and finger emplacement mechanism in shale-dominated formations: A field study at Cuesta del Chihuido, Neuquén Basin, Argentina. *Journal of the Geological Society*, *174*(3), 422–433. https://doi.org/10.1144/jgs2016-056
Sun, R. J. (1969). Theoretical size of hydraulically induced horizontal fractures and corresponding surface uplift in an idealized medium. *Journal of Geophysical Research*, *74*(25), 5995–6011.
Taisne, B., & Jaupart, C. (2009). Dike propagation through layered rocks. *Journal of Geophysical Research*, *114*, B09203. https://doi.org/10.1029/2008JB006228
Takada, A. (1990). Experimental study on propagation of liquid-filled crack in gelatin: Shape and velocity in hydrostatic stress condition. *Journal of Geophysical Research*, *95*(B6), 8471–8481.
Takada, A. (1994). Development of a subvolcanic structure by the interaction of liquid-filled cracks. *Journal of Volcanology and Geothermal Research*, *61*(3), 207–224.
Tibaldi, A., Bonali, F., & Corazzato, C. (2014). The diverging volcanic rift system. *Tectonophysics*, *611*, 94–113.
Toutain, J. P., Bachelery, P., Blum, P. A., Cheminee, J. L., Delorme, H., Fontaine, L., … Taochy, P. (1992). Real time monitoring of vertical ground deformations during eruptions at Piton de la Fournaise. *Geophysical Research Letters*, *19*(6), 553–556.
Trippanera, D., Acocella, V., & Ruch, J. (2014). Dike-induced contraction along oceanic and continental divergent plate boundaries. *Geophysical Research Letters*, *41*, 7098–7104. https://doi.org/10.1002/2014GL061570
Vachon, R., & Hieronymus, C. F. (2016). Effect of host-rock rheology on dyke shape, thickness, and magma overpressure. *Geophysical Journal International*, ggw448, 1414–1429.
White, R. S., Drew, J., Martens, H. R., Key, J., Soosalu, H., & Jakobsdóttir, S. S. (2011). Dynamics of dyke intrusion in the mid-crust of Iceland. *Earth and Planetary Science Letters*, *304*(3), 300–312.
Wright, T. J., Sigmundsson, F., Pagli, C., Belachew, M., Hamling, I. J., Brandsdóttir, B., … Ebinger, C. (2012). Geophysical constraints on the dynamics of spreading centres from rifting episodes on land. *Nature Geoscience*, *5*(4), 242–250.

Experimental Constraints on Forecasting the Location of Volcanic Eruptions from Pre-eruptive Surface Deformation

Guldstrand, F., O. Galland, E. Hallot, and S. Burchardt

Frontiers in Earth Science, *6*(7), (2018)

https://doi.org/10.3389/feart.2018.00007

III

frontiers in Earth Science

ORIGINAL RESEARCH
published: 20 February 2018
doi: 10.3389/feart.2018.00007

Experimental Constraints on Forecasting the Location of Volcanic Eruptions from Pre-eruptive Surface Deformation

Frank Guldstrand[1], Olivier Galland[1], Erwan Hallot[2] and Steffi Burchardt[3,4]*

[1] Physics of Geological Processes (PGP), The NJORD Centre, Department of Geosciences, University of Oslo, Oslo, Norway, [2] Univ Rennes, CNRS, Géosciences Rennes - UMR 6118, Rennes, France, [3] Department of Earth Sciences, Uppsala University, Uppsala, Sweden, [4] Centre for Natural Hazards and Disaster Science, Department of Earth Sciences, Uppsala University, Uppsala, Sweden

Volcanic eruptions pose a threat to lives and property when volcano flanks and surroundings are densely populated. The local impact of an eruption depends firstly on its location, whether it occurs near a volcano summit, or down on the flanks. Then forecasting, with a defined accuracy, the location of a potential, imminent eruption would significantly improve the assessment and mitigation of volcanic hazards. Currently, the conventional volcano monitoring methods based on the analysis of surface deformation assesses whether a volcano may erupt but are not implemented to locate imminent eruptions in real time. Here we show how surface deformation induced by ascending eruptive feeders can be used to forecast the eruption location through a simple geometrical analysis. Our analysis builds on the results of 33 scaled laboratory experiments simulating the emplacement of viscous magma intrusions in a brittle, cohesive Coulomb crust under lithostatic stress conditions. The intrusion-induced surface deformation was systematically monitored at high spatial and temporal resolution. In all the experiments, surface deformation preceding the eruptions resulted in systematic uplift, regardless of the intrusion shape. The analysis of the surface deformation patterns leads to the definition of a vector between the center of the uplifted area and the point of maximum uplift, which systematically acted as a precursor to the eruption's location. The temporal evolution of this vector indicated the direction in which the subsequent eruption would occur and ultimately the location itself, irrespective of the feeder shapes. Our findings represent a new approach on how surface deformation on active volcanoes that are not in active rifts could be analysed and used prior to an eruption with a real potential to improve hazard mitigation.

Keywords: surface deformation, laboratory modeling, cone sheets, dykes, eruption forecasting

KEY POINTS

- We quantitatively analyse pre-eruptive intrusion-induced surface deformation from 33 scaled laboratory experiments resulting in eruptions.
- A robust proxy extracted from surface deformation geometry enables systematic predictions of the locations of a subsurface intrusion and imminent eruption.
- Forecasting an eruption location is possible without geodetic modeling but requires volcano monitoring at high spatiotemporal resolution.

OPEN ACCESS

Edited by:
Nicolas Fournier, GNS Science, New Zealand

Reviewed by:
Alessandro Bonforte, Istituto Nazionale di Geofisica e Vulcanologia, Italy
Luca Caricchi, Université de Genève, Switzerland

****Correspondence:***
Frank Guldstrand
f.b.b.guldstrand@geo.uio.no

Specialty section:
This article was submitted to Volcanology, a section of the journal Frontiers in Earth Science

Received: *09 October 2017*
Accepted: *22 January 2018*
Published: *20 February 2018*

Citation:
Guldstrand F, Galland O, Hallot E and Burchardt S (2018) Experimental Constraints on Forecasting the Location of Volcanic Eruptions from Pre-eruptive Surface Deformation . Front. Earth Sci. 6:7. doi: 10.3389/feart.2018.00007

INTRODUCTION

Preceding any potential volcanic eruption, the propagation of magma at shallow depth induces deformation of the Earth's surface (Dzurisin, 2007). During the last decade, geodetic measurements of ground deformation due to such magmatic intrusions have become a standard tool in monitoring active volcanic systems (Amelung et al., 2000; Wright et al., 2006; Sigmundsson et al., 2010, 2015). These tools commonly include tiltmeters (Toutain et al., 1992), Global Navigation Satellite Systems (GNSS; Bonforte and Guglielmino, 2015; Lee et al., 2015), Interferometry Synthetic Aperture Radar (InSAR; Massonnet et al., 1995; Lanari et al., 1998; Fukushima et al., 2005), and photogrammetry (Cayol and Cornet, 1998; Hollingsworth et al., 2013; Hibert et al., 2015).

Surface deformation is one of the several routinely monitored observables from active volcanic regions that are used to assess the volcano's behavior and eruption probability. However, pre-eruptive geodetic data from active volcanoes that were acquired at high frequency suggest that they contain some precursory signals useful to track the pre-eruptive propagation of volcanic feeders (e.g., Toutain et al., 1992; Cannavò et al., 2015). Thus, they may have the potential to be used to forecast the location of subsurface magma in real time. Nevertheless, systematic and robust surface deformation precursors for volcanic eruption locations have not been identified yet.

Here we present results from 33 scaled laboratory models of shallow intrusions that ultimately fed eruptions (**Figure 1**). During each experiment we periodically monitored the surface deformation caused by the subsurface propagation of the feeder. A simple geometrical analysis of the surface deformation data reveals that the eruption locations were systematically forecastable without performing any geodetic modeling. We also observe that distinct shapes of the eruptive feeders, here dykes and cone sheets, exhibit distinct, characteristic surface deformation signatures. We conclude that geodetic surface deformation data, if acquired at high enough spatial and temporal resolutions, do have the potential to be used to follow magma pathways at shallow depth and to forecast the locations of imminent volcanic eruptions without any modeling.

METHOD

Experimental Protocol

All the experiments were performed in the experimental apparatus of, and using the experimental protocol described by Galland et al. (2009), Galland (2012), Galland et al. (2014), and Guldstrand et al. (2017). Galland et al. (2006) describe in detail the mechanical properties of the model materials and the scaling of the models. Below, we briefly summarize the experimental materials and protocol.

The model materials are fine-grained silica flour and molten vegetable oil, to simulate brittle rocks and magma, respectively. The flour consists of fine ($\sim$15 μm), angular grains of crystalline silica flour. It has a cohesive strength of 369 $\pm$ 44 Pa, a friction coefficient of 0.81 $\pm$ 0.06 (corresponding to an angle of internal friction of $\sim$39°) and a tensile strength of 100 Pa (Galland et al., 2006, 2009). As 1 cm in the models represents 100–1,000 m in nature, the resulting stress ratio indicates that the model crust should be 13×10^3-250×10^3 times weaker than its geological prototype (Abdelmalak et al., 2016). The silica flour fulfills this criterion. It reproduces the brittle Coulomb behavior of the Earth's crust (Abdelmalak et al., 2016). Additionally, the flour is cohesive and has the ability to stand non-negligible elastic stresses along stable vertical walls (Abdelmalak et al., 2016). However, the elastic properties of silica flour remain poorly constrained, as is the case for granular materials in general. It is therefore challenging to address how the elastic stresses in our models scale with those in geological systems (Galland et al., 2017).

The model magma consists of a vegetable oil that is solid at room temperature and melts at $\sim$31°C (Galland et al., 2006). Molten, it is a Newtonian fluid with a weak temperature-dependent viscosity (Galland et al., 2006). Using these materials, a generic experiment consists in injecting hot oil into the flour at room temperature to generate an intrusion. At the injection temperature of $\sim$50°C, the oil exhibits a viscosity of 2×10^{-2} Pa s and a density of 890 kg m^{-3}. Oil percolation within the flour during injection is inhibited as silica is chemically incompatible with the oil and an oil intrusion is dominantly accommodated by deformation of the flour (Galland et al., 2006). During an experiment, the effects of cooling of the oil against the flour can be neglected, as intrusion durations are shorter than conductive cooling timescales. Our model scales through assuming that the ratio of viscous stresses in the oil/magma to the cohesion of the flour/host rock are identical in the model and nature (Galland et al., 2014). In nature, magma velocities can be of the order of 1–10^{-2} m s^{-1} (Toutain et al., 1992). The experimental device allows for oil velocities of 10^{-3}-10^{-1} m s^{-1}. As magma viscosities cover a wide range (10–10^7 Pa s), relevant model viscosities fall in the range 4×10^{-9}-75 Pa s, which the oil fulfills. To simplify, the oil at 50°C dominantly represents a rather viscous magma of intermediate to felsic composition.

For a generic experiment, the experimental setup consists of a 40 cm wide square box with a circular inlet pipe at its center, into which a known mass of silica flour is poured. Then a high-frequency vibrator shakes the box to compact the flour until a bulk density of 1,050 kg m^{-3} is reached. A flat metal plate is placed onto the model surface during compaction to ensure repeatable experiment preparation and an initial flat and horizontal surface of the models; the metal plate is removed after compaction. A volumetric pump injects the molten oil at constant flow rate through the circular inlet. With such a setup, it is possible to vary, among other parameters, the injection depth, the diameter of the inlet, and the flow rate. Depending on these parameter settings, the models systematically produce various geometries of intrusions, such as vertical sheet intrusions (dykes) and cone sheets (**Figure 2**; Galland et al., 2014). The vertical sheet intrusions initiated at the inlet and propagated to the surface. They often split to form a hull-shaped termination or turned into inclined sheets before reaching the surface (Galland et al., 2014).

Surface Data

The surface deformation data used in the present study were acquired during 33 out of the 51 experiments from Galland et al.

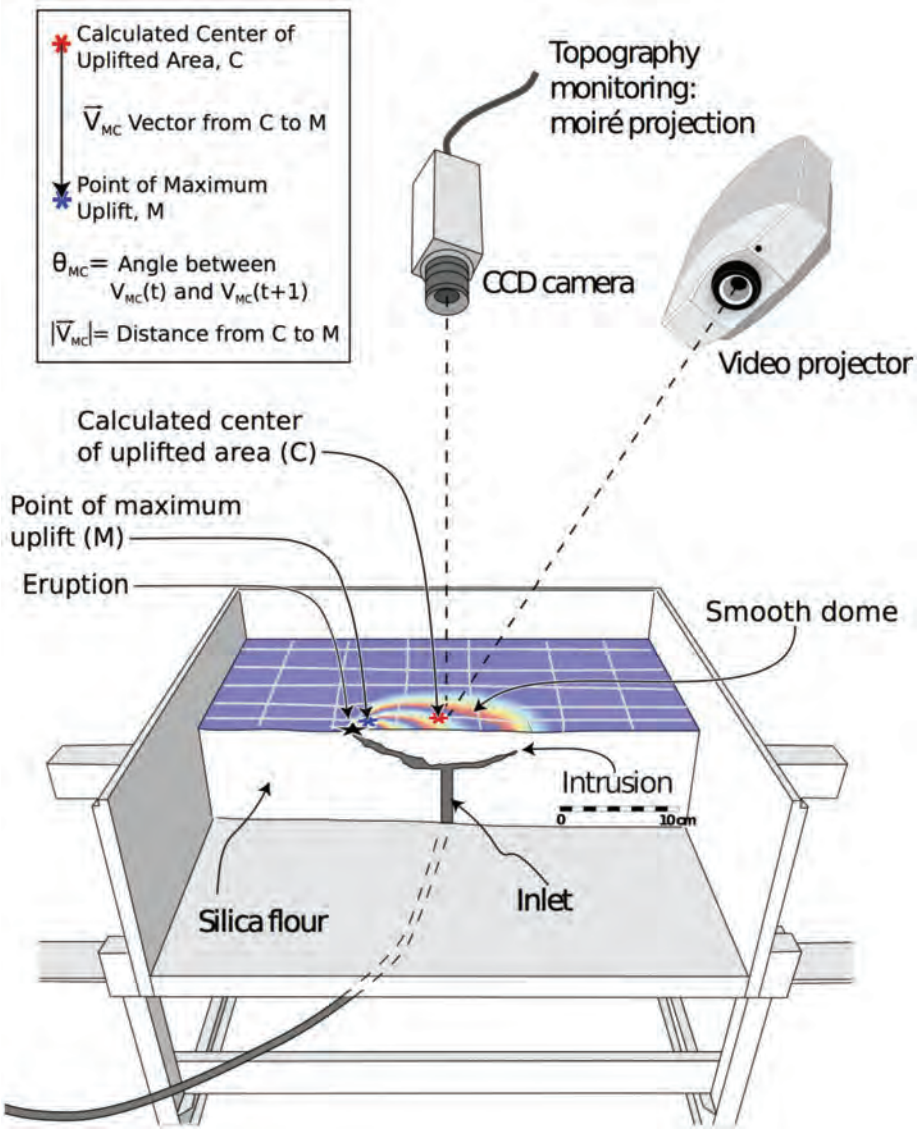

FIGURE 1 | Experimental device used to simulate shallow intrusions of oil into silica flour (adapted from (Galland, 2012) with permission, Galland et al., 2006, 2014), which induced uplift of the surface of the models that were periodically monitored (1.5 s time steps) using a moiré projection system (Bréque et al., 2004; Galland, 2012), and fed eruptions (black star). At each time step of a given experiment, simple geometrical parameters (see legend box) were calculated from the surface uplift map. This study shows that their evolution with time represents a precursor for the location of the next eruption.

(2014). Note that although surface deformation was monitored during all their experiments, Galland et al. (2014) focused on the dynamics of the intrusion processes at depth and on the resulting intrusion shapes, only. The resulting surface deformation dataset has subsequently been analyzed by Guldstrand et al. (2017), who focused on mechanical interpretations associated with the intrusion mechanisms at depth. The present analysis of the dataset is different and discusses the implications for volcanic hazards assessment. The 33 experiments considered here correspond to those for which enough surface deformation data were available during the entire duration of the experiments. They are representative of the full ranges of the parameters explored by Galland et al. (2014).

During the experiments, surface data were monitored using a moiré projection apparatus. The moiré monitoring (Bréque et al., 2004; Galland, 2012) was performed through projecting sets of illuminated straight fringes onto the model surface. The fringes remain straight on a flat surface but deform when projected on a surface with topography, producing curved fringe patterns. A video camera perpendicular to the surface captured the evolving fringe patterns on the model surface periodically (by successive scans starting at time step intervals of 1.5 s), which were subsequently analyzed to compute time series of digital elevation models (DEMs; Bréque et al., 2004). The duration of a scan for the acquisition of an individual DEM was ∼1 s and we chose to set the time of each DEM at the beginning of each scan.

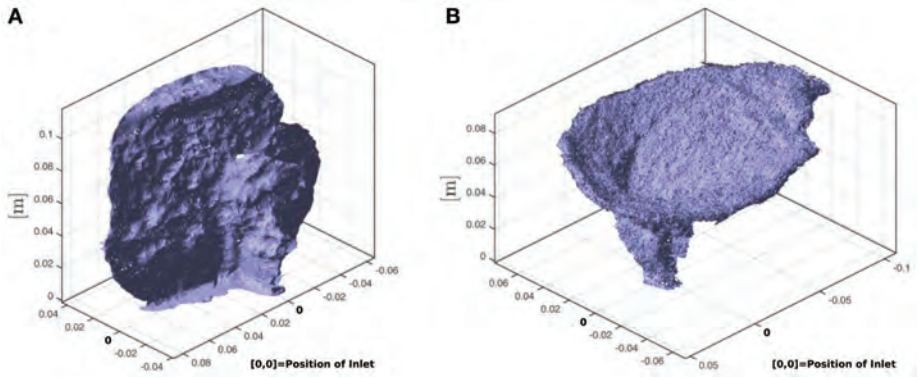

FIGURE 2 | Typical intrusions produced using our experimental setup, **(A)** vertical sheet intrusion classified as dyke and **(B)** cone sheet (reprinted with permission from Guldstrand et al., 2017).

Focussing on surface deformation induced by the intrusions, we have analyzed differential digital elevation models (ΔDEMs) obtained from the difference between the DEMs at given time steps and the DEM of the initial model surface. To limit noise effects, ΔDEM data were smoothed. The lateral resolution of the ΔDEMs is <1 mm, and the vertical precision of the smoothed ΔDEMs is ∼0.1 mm (Guldstrand et al., 2017). As only uplifts were observed for both dyke and cone sheet experiments, for each ΔDEM we have defined the group of pixels corresponding to the uplifted area using an uplift threshold criterion of 0.1 mm. We have then calculated the location of the mean center (C) of the uplifted area by averaging the positions of each pixel in the uplifted area, giving the same weight to each pixel (**Figure 1**). The locations of the centers of the uplifted areas were then known for each time step of each experiment in a consistent way. The uplifted areas never extended further than about 15 cm from the box walls, so that sidewall effects are assumed to be negligible. This is confirmed by the random location of the eruption sites in our experimental series.

The experiments lasted between a few seconds up to about 1 min, from the time at which the injection started up to the time at which the oil erupted. The second and the last scans of moiré projections started at about the same times, within errors of 1.5 s, as the injection started and the eruption occurred, respectively. To compare experiments of varying durations, we have normalized the time t at a given time step by the experiment duration, t_e. Therefore, for each experiment, the dimensionless time, t/t_e, which varied from 0 to 1, approximately represents the relative duration of the intrusion up to the eruption.

RESULTS

The 33 experiments that produced suitable surface deformation data lasted from ∼6 to ∼53 s. They produced 16 dykes and 17 cone sheets depending on the values of depth and diameter of the injection inlet, as well as the injection velocity of the oil (Galland et al., 2014; Guldstrand et al., 2017).

All the experiments, i.e., both those producing dykes and cone sheets, displayed an initial symmetrical bell-shaped uplift of the surface followed by the development of an uplift asymmetry that grew until the oil erupted in the immediate vicinity of the point of maximum uplift (**Figure 3**; Guldstrand et al., 2017). The dykes systematically triggered uplift, regardless of their final shapes, i.e., vertical sheets with or without, split or inclined terminations. To quantify the uplift asymmetry, we have calculated the positions of (1) the center of the uplifted area and (2) the point of maximum uplift at each time step (points C and M, respectively, **Figure 1**). We defined a vector, $\overrightarrow{V}_{MC}$, connecting these points.

During the early stages of uplift, in all the experiments, points C and M closely clustered, as illustrated by the short vectors $\overrightarrow{V}_{MC}$ (**Figures 4C,D**), the orientation of which strongly varied with time. The points of maximum uplift (M) then migrated away from the center (C), as shown by the lengthening of $\overrightarrow{V}_{MC}$ (**Figures 4C,D**). Concomitantly, the orientation of $\overrightarrow{V}_{MC}$ focused and stabilized in azimuth with time. Importantly, in all the experiments, $\overrightarrow{V}_{MC}$ ultimately pointed toward the subsequent eruption location (**Figures 4C,D**). The eruptions systematically initiated at the intersection between the ultimate $\overrightarrow{V}_{MC}$ direction and the marginal border-zone of the uplifted area.

We also calculated (1) the evolution of $|\overrightarrow{V}_{MC}|$ scaled by the injection depth (d) and (2) the rotation angle (θ_{MC}) of the vectors $\overrightarrow{V}_{MC}$ between two successive time steps (**Figures 5**, **6**). For each experiment, the evolution of $\left|\overrightarrow{V}_{MC}\right|/d$ quantifies how point M moved away from C, and θ_{MC} indicates the stability of the direction of V_{MC}. We arbitrarily consider that θ_{MC} was stable once it remained <20°.

There are systematic differences in the evolution of $\left|\overrightarrow{V}_{MC}\right|/d$ and θ_{MC} for dykes and cone sheets (**Figures 5**, **6**). During dyke experiments, on average, $\left|\overrightarrow{V}_{MC}\right|/d$ remained small until $t/t_e \sim 0.4$, from which $\left|\overrightarrow{V}_{MC}\right|/d$ increased rapidly before stabilizing again at $t/t_e \sim 0.8$ (**Figure 5A**), displaying an overall stepwise or two-phase evolution. In detail for each individual experiment, the rapid $\left|\overrightarrow{V}_{MC}\right|/d$ increase started at different times ($t/t_e \sim 0.2$ to 0.8; **Figure 5A**) and was often relatively short in

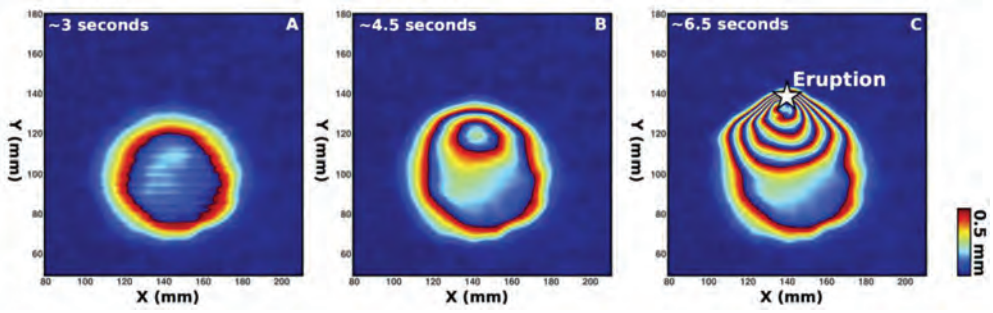

FIGURE 3 | Differential digital elevation models (ΔDEMs) at early **(A)**, intermediate **(B)** and ultimate **(C)** time steps measured during a representative dyke experiment. ΔDEM is displayed as fringes, each fringe series corresponding to an uplift of 0.5 mm.

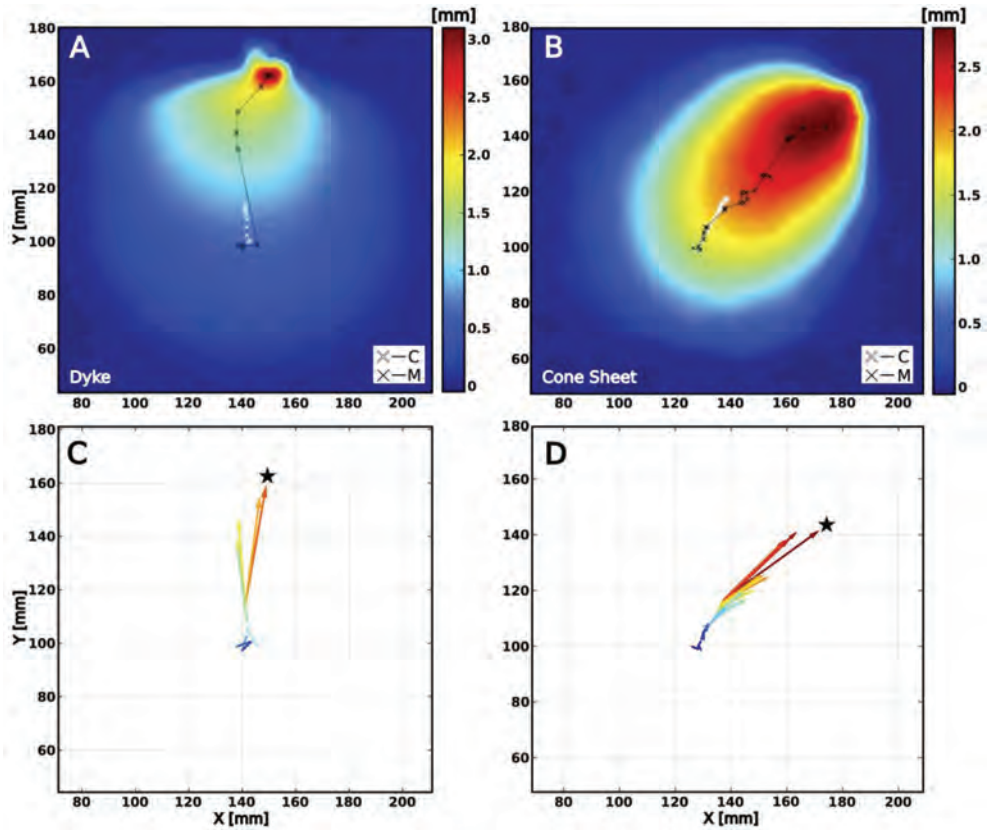

FIGURE 4 | (A,B) ΔDEM before eruption for a representative dyke **(A)** and cone sheet **(B)** experiment (uplift in mm). White and black crosses show the successive locations of the centers (C) of the uplifted area, and of the maximum uplifts (M), respectively. **(C,D)** Plots of the successive vectors $\overrightarrow{V}_{MC}$ computed from the respective maps, **(A,B)**, from the early (dark blue) to the final stages (dark red). A black star locates the eruption points. Final points of maximum uplifts almost locate the eruptions.

time. In contrast, for cone sheets, $\left|\overrightarrow{V}_{MC}\right|/d$ exhibited a gradual, progressive, quasi-linear increase (**Figure 5B**). In addition, for most of the dykes, θ_{MC} was highly variable for more than half of the experiment durations (up to $t/t_e \sim 0.6$; **Figure 6A**) before decreasing and stabilizing, whereas for cone sheets, θ_{MC} generally stabilized earlier ($t/t_e \sim 0.3$; **Figure 6B**).

INTERPRETATION AND DISCUSSION

During the 33 experiments, the vector $\overrightarrow{V}_{MC}$ systematically pointed toward the location of the subsequent eruption once approximately stabilized in azimuth (± 20°; **Figures 4**, **6**). As $\overrightarrow{V}_{MC}$ is a parameter that was directly extracted from surface deformation data using only minimal calculations, real-time

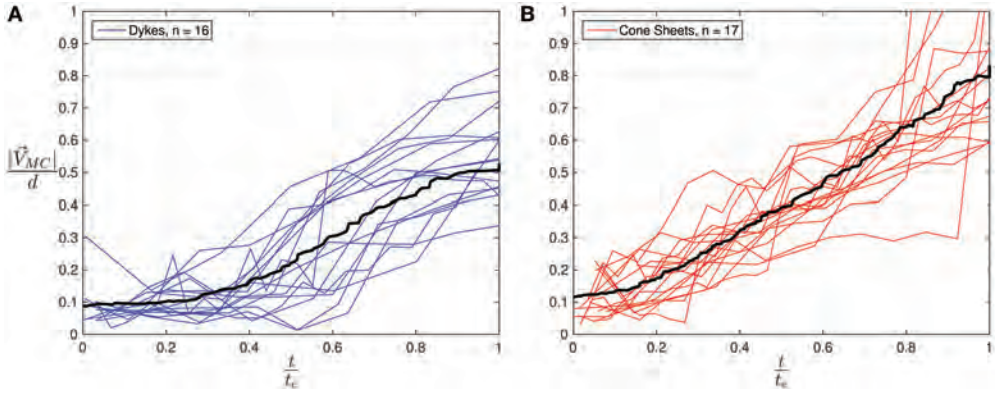

FIGURE 5 | Plots of $|\vec{V}_{MC}|$ scaled by the injection depth (*d*) against dimensionless time, t/t_e for dyke **(A)** and cone sheet **(B)** experiments. Black lines mark the respective moving averages.

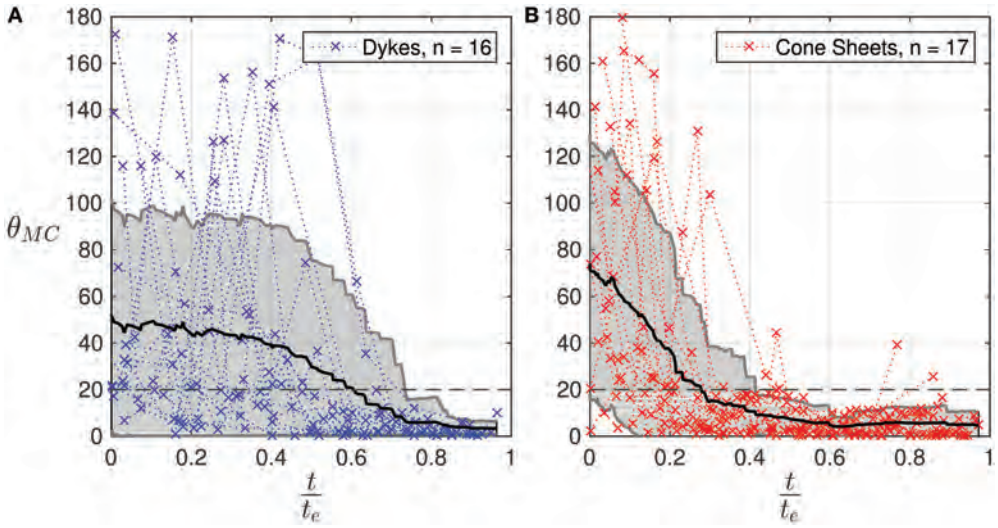

FIGURE 6 | Plots of the rotation angles θ_{MC} between two successive vectors V_{MC} as a function of dimensionless time, t/t_e, for the dyke **(A)** and cone sheet **(B)** experiments. Each graph displays the corresponding θ_{MC} moving mean (black line) and standard deviation (gray area). For cone sheets, the orientation of the vector generally stabilizes (θ_{MC} decreases below 20°, gray dashed line) earlier ($t/t_e \sim 0.3$) than for dykes ($t/t_e \sim 0.6$).

measurements of $\vec{V}_{MC}$ are potentially achievable in natural systems. Therefore, the evolution of $\vec{V}_{MC}$ represents a robust geometrical precursor that could be useful in forecasting where a real eruption should occur, with substantial implications for hazard mitigation in active volcanic areas.

Consistent with our observations, previous two-dimensional (Abdelmalak et al., 2012) and three-dimensional (Galland, 2012) experiments, as well as theoretical models of surface uplift due to sheet intrusions (Pollard and Holzhausen, 1979; Okada, 1985), have also shown that the points of maximum uplift roughly locate the shallowest parts of intrusive feeders, such as dyke tips, at depth. Hence, the migration of a point of maximum uplift at the Earth's surface in volcanic areas likely represents a relevant geometric proxy to locate where magma is the shallowest and is ascending underground.

The distinct surface deformation signatures associated with the experimental dykes and cone sheets likely reflect contrasting emplacement dynamics (cf. Guldstrand et al., 2017). The progressive increase of $\left|\vec{V}_{MC}\right|/d$ from the earliest stages of subsurface propagation reflects the gradual asymmetrical propagation of a cone sheet (**Figure 5B**). Conversely, the stepwise or two-phase increase of $\left|\vec{V}_{MC}\right|/d$ is interpreted to indicate a two-stage evolution with (1) an initial vertical ascent of a dyke at depth, followed by (2) the interaction with the free surface and possible splitting of the dyke tip or oblique propagation toward the surface from a shallower depth (Mathieu et al., 2008; Abdelmalak et al., 2012; Galland et al., 2014). The stabilization of the orientation of $\vec{V}_{MC}$ (**Figure 6B**) may coincide with this second phase. In addition, the contrasting signatures of

the experimental dykes and cone sheets suggest that real-time analysis of the deformation of natural surfaces can be useful to infer the geometry of a propagating intrusion prior to an eruption.

Our model uses an initial flat surface and does not include the effect of an initial topography or slope, often relevant for volcanic systems. Additionally, our model crust material is homogeneous and does not account for any heterogeneity that may also influence surface deformation signatures due to intrusions. Whether or not our method applies for shallow intrusions that develop elsewhere than under flat volcanic fields or calderas and in stratified and/or fractured crusts has not been tested. However, we expect that any magma-induced surface deformation will reflect the underlying developing asymmetry of the intrusion, in which case the method proposed here should still be applicable from a non-flat initial surface and a heterogeneous crust.

The surface deformation above our experimental dykes differs from that associated with dykes emplaced in rifts (e.g., Wright et al., 2006; Biggs et al., 2009; Sigmundsson et al., 2015) and the expected deformation predicted by static elastic analytical models of dykes (e.g., Okada, 1985). The latter display two prominent lobes of uplift separated by a trough aligned above the dyke apex. In contrast, our experimental dykes only triggered surface uplift, regardless of whether the intrusions propagated vertically up to the surface or deviated into inclined sheets. Guldstrand et al. (2017) attributed the difference with the static elastic models to the use of a weakly elastic, cohesive Mohr-Coulomb flour, in which the experimental dykes likely propagated as viscous indenters instead of resulting in pure elastic tensile fractures. In addition, the experiments account for magma flow and intrusion propagation, whereas elastic models are static. They are thus likely relevant for volcanic systems where the shallow crust is weak (e.g., Thun et al., 2016) and/or in which the intruding magma is relatively viscous (Galland et al., 2014; Guldstrand et al., 2017). Guldstrand et al. (2017) also attributed the difference with surface deformation measured in rifts to the absence of far-field tectonic extension in the experiments, thus making them relevant for volcanic systems that are not located in rifts.

Uplifting in the form of doming is commonly measured in active volcanic areas and models of inflating/pressurized spherical sources or horizontal sheet-intrusions generally fits such uplifts (e.g., Pedersen and Sigmundsson, 2006; Walter and Motagh, 2014). From our results, an alternative interpretation may consist in propagating vertical sheet intrusions through a Mohr-Coulomb crust (Guldstrand et al., 2017). Moreover, as our experiments produced inclined sheets on top of some vertical dykes, and cone sheets, our analysis may also be relevant for interpreting surface deformation in volcanic areas prone to forming inclined sheets and cone sheets (e.g., Bagnardi et al., 2013).

As mentioned above, the relevance of using points of maximum uplift has been proposed earlier. Such points have been recorded among geodetic data measured on active volcanoes, e.g., at Piton de la Fournaise, Réunion Island (Toutain et al., 1992). The data and interpretation of Toutain et al. (1992) satisfactorily compare to those from our experiments. Indeed, the correlation between the zone of maximum uplift and the eruption location, as well as the two-stage behavior of the surface deformation due to an intrusive feeder that was interpreted as a dyke, exhibit encouraging similarities with our experimental results. Another famous example was the prominent asymmetrical bulging preceding the 1980 eruption of Mount Saint Helens (Dzurisin, 2007, and references therein). The bulging flank of the volcano happened to be the location of the 1980 explosion, and laboratory experiments demonstrated that the asymmetry of the bulging reflected the asymmetrical shallow growth of the underlying cryptodome (Donnadieu and Merle, 1998; Merle and Donnadieu, 2000). These examples suggest that the precursors identified in the laboratory may also be applied to active volcanoes. Consequently, monitoring surface deformation on active volcanoes with both high temporal and spatial resolution has the potential to constrain, in real-time, simple geometrical parameters, such as $|\overrightarrow{V}_{MC}|$ and θ_{MC}, to forecast the location of both shallow intrusions and imminent eruptions. To make such forecasts possible requires implementing high frequency monitoring methods, such as GNSS and/or tiltmeter, and fast data processing. However, the lack in spatial resolution does not ensure accurate identification of the locations of uplift center and maximum, which conversely can easily be identified using InSAR data.

Notably, our results show that the location of most of the experimental eruptions could have been accurately predicted to occur within an angular sector of about 20° from approximately half of the experiment duration (**Figure 6**). Transposed to nature, where enough time is required to take suitable societal measures before an eruption occurs, such a forecast could be achieved up to several weeks to days before the eruptions. Indeed, the very first signs of pre-eruptive deformation on volcanoes have been documented to occur approximately up to 3 months prior to the eruptions (Froger et al., 2004; Peltier et al., 2006; Poland et al., 2008; Chadwick et al., 2012; Langmann et al., 2012). As some intrusions may also propagate underground over shorter timescales (dykes may propagate as fast as several tens of cm/s; Toutain et al., 1992), the predictions would be accurate enough within just a few hours before a potential eruption, which may be inadequate for hazard mitigation. Nonetheless, in adequate situations, our results indicate that the accuracy in predicting the location of an imminent eruption increases as time proceeds and that the first predictions could be given earlier when the feeder is a cone sheet. Moreover, our analysis allows for excluding a large part of the deforming area depending on the early direction $\overrightarrow{V}_{MC}$. Efforts can then be made to focus analysis on the area highlighted by $\overrightarrow{V}_{MC}$.

Our modeling approach and results highlight the dynamic nature of surface deformation associated with shallow magma emplacement. Resolving surface deformation both at high spatial and temporal resolutions is relevant to follow the evolution of simple geometric parameters, such as the point of maximum uplift, which constitute proxies for the location of on-going magma ascent. In addition, as long as changes in the evolution of parameters, such as the focus in azimuth of the points of maximum uplift, develop a significant time prior to an eruption,

they have the potential to be used as precursors, indicative of the approximate location of an imminent volcanic eruption. Extracted only from the direct observation of surface data, these precursors are purely geometrical and are not derived from any mechanical criteria or hypothesis. Yet they are relevant for various magma feeder geometries. Our analysis illustrates that time-consuming computational surface data modeling, as commonly used to analyse geodetic data, may not be necessary for the purpose of forecasting eruption locations.

CONCLUSION

In this study, we analyse the surface deformation monitored during 33 scaled laboratory experiments simulating magma emplacement in a brittle crust under lithostatic stress conditions, i.e., not subjected to regional or local extensional tectonic stresses. Depending on the parameter sets, the experiments simulated the emplacement of dykes or cone sheets (Galland et al., 2014); the associated surface deformation systematically exhibit surface uplift. Our main results are the following:

- We define a vector $\overrightarrow{V}_{MC}$ joining the center of the uplifted area to the point of maximum uplift.
- During the experiments, the final vectors $\overrightarrow{V}_{MC}$ systematically point toward the locations of the forthcoming eruptions, regardless of whether the feeder is a dyke or a cone sheet. This result shows that the vector $\overrightarrow{V}_{MC}$ is a robust geometric precursor for forecasting imminent volcanic eruptions.
- The surface deformation patterns and associated vectors are drastically different for dykes and cone sheets; for cone sheet intrusions the surface vectors elongate gradually and stabilize in direction within angular sectors of about 20° as early as less than half of the intrusion duration; in contrast, when dykes intrude, the surface vectors exhibit a two-stage evolution with sudden elongation and direction stabilization at about half of the intrusion duration. This result shows that the time evolution of the vector $\overrightarrow{V}_{MC}$ is a good proxy for identifying the nature of the sub-surface volcanic feeder.
- The real-time tracking and identification surface vector evolution could be used on active volcanic systems as robust proxies for determining the shape and location of the sub-surface propagating feeders and locating the area of imminent volcanic eruptions.
- Our study shows that forecasting eruption locations using surface deformation data may be achievable without using geodetic modeling, assuming that the surface data are captured at both high spatial and temporal resolution.

AUTHOR CONTRIBUTIONS

FG produced the data analysis, figures and wrote most of the text. OG contributed with the concept and scaling of the laboratory model, experiments, discussions and interpretations. EH performed experiments and contributed with discussion and analysis. SB performed experiments and provided comments and discussion.

ACKNOWLEDGMENTS

Guldstrand's doctoral position is funded by the Norwegian Research Council (DIPS project, grant no. 240467). Part of the work was performed in the MeMoVolc Networking Programme from the European Science Foundation (exchange grant no. 4251). F. Bjugger and A. Souche are acknowledged for assistance and discussions with the Volcano Plumbing Systems group at PGP. Burchardt acknowledges financial support Uppsala University and the Swedish Research Council for a research visit to PGP. Hallot acknowledges his welcome to PGP thanks to a half-year sabbatical from Université de Rennes 1. The authors acknowledge the constructive reviews of two reviewers, the associate editor, Nicolas Fournier and chief editor, Valerio Acocella, whose comments improved the manuscript.

REFERENCES

Abdelmalak, M., Bulois, C., Mourgues, R., Galland, O., Legland, J.-B., and Gruber, C. (2016). Description of new dry granular materials of variable cohesion and friction coefficient: implications for laboratory modeling of the brittle crust. *Tectonophysics* 684, 39–51. doi: 10.1016/j.tecto.2016.03.003

Abdelmalak, M., Mourgues, R., Galland, O., and Bureau, D. (2012). Fracture mode analysis and related surface deformation during dyke intrusion: results from 2D experimental modelling. *Earth Planet. Sci. Lett.* 359, 93–105. doi: 10.1016/j.epsl.2012.10.008

Amelung, F., Jónsson, S., Zebker, H., and Segall, P. (2000). Widespread uplift and "trapdoor" faulting on Galapagos volcanoes observed with radar interferometry. *Nature* 407, 993–996. doi: 10.1038/35039604

Bagnardi, M., Amelung, F., and Poland, M. P. (2013). A new model for the growth of basaltic shields based on deformation of Fernandina volcano, Galápagos Islands. *Earth Planet. Sci. Lett.* 377, 358–366. doi: 10.1016/j.epsl.2013.07.016

Biggs, J., Amelung, F., Gourmelen, N., Dixon, T. H., and Kim, S.-W. (2009). InSAR observations of 2007 Tanzania rifting episode reveal mixed fault and dyke extension in an immature continental rift. *Geophys. J. Int.* 179, 549–558. doi: 10.1111/j.1365-246X.2009.04262.x

Bonforte, A., and Guglielmino, F. (2015). Very shallow dyke intrusion and potential slope failure imaged by ground deformation: the 28 December 2014 eruption on Mount Etna. *Geophys. Res. Lett.* 42, 2727–2733. doi: 10.1002/2015GL063462

Bréque, C., Dupre, J.-C., and Bremand, F. (2004). Calibration of a system of projection moiré for relief measuring: biomechanical applications. *Opt. Lasers Eng.* 41, 241–260. doi: 10.1016/S0143-8166(02)00198-7

Cannavò, F., Camacho, A. G., González, P. J., Mattia, M., Puglisi, G., and Fernández, J. (2015). Real time tracking of magmatic intrusions by means of ground deformation modeling during volcanic crises. *Sci. Rep.* 5:10970. doi: 10.1038/srep10970

Cayol, V., and Cornet, F. H. (1998). Three-dimensional modeling of the 1983–1984 eruption at Piton de la Fournaise Volcano, Réunion Island. *J. Geophys. Res.* 103, 18025–18037. doi: 10.1029/98JB00201

Chadwick, W. W. Jr., Nooner, S. L., Butterfield, D. A., and Lilley, M. D. (2012). Seafloor deformation and forecasts of the April 2011 eruption at Axial Seamount. *Nat. Geosci.* 5, 474–477. doi: 10.1038/ngeo1464

Donnadieu, F., and Merle, O. (1998). Experiments on the indentation process during cryptodome intrusions: new insights

into Mount St. Helens deformation. *Geology* 26, 79–82. doi: 10.1130/0091-7613(1998)026<0079:EOTIPD>2.3.CO;2

Dzurisin, D. (2007). *Volcano Deformation: Geodetic Monitoring Techniques*. Chichester: Springer.

Froger, J.-L., Fukushima, Y., Briole, P., Staudacher, T., Souriot, T., and Villeneuve, N. (2004). The deformation field of the August 2003 eruption at Piton de la Fournaise, Reunion Island, mapped by ASAR interferometry. *Geophys. Res. Lett.* 31:L14601. doi: 10.1029/2004GL020479

Fukushima, Y., Cayol, V., and Durand, P. (2005). Finding realistic dike models from interferometric synthetic aperture radar data: the February 2000 eruption at Piton de la Fournaise. *J. Geophys. Res.* 110:B03206. doi: 10.1029/2004JB003268

Galland, O. (2012). Experimental modelling of ground deformation associated with shallow magma intrusions. *Earth Planet. Sci. Lett.* 317, 145–156. doi: 10.1016/j.epsl.2011.10.017

Galland, O., Burchardt, S., Hallot, E., Mourgues, R., and Bulois, C. (2014). Dynamics of dikes versus cone sheets in volcanic systems. *J. Geophys. Res.* 119, 6178–6192. doi: 10.1002/2014JB011059

Galland, O., Cobbold, P. R., Hallot, E., de Bremond d'Ars, J., and Delavaud, G. (2006). Use of vegetable oil and silica powder for scale modelling of magmatic intrusion in a deforming brittle crust. *Earth Planet. Sci. Lett.* 243, 786–804. doi: 10.1016/j.epsl.2006.01.014

Galland, O., Holohan, E., van Wyk de Vries, B., and Burchardt S. (2017). "Laboratory modelling of volcano plumbing systems: a review," in *Advances in Volcanology*, ed K. Nemeth (Berlin; Heidelberg: Springer), 1–68. doi: 10.1007/11157_2015_9

Galland, O., Planke, S., Neumann, E.-R., and Malthe-Sørenssen, A. (2009). Experimental modelling of shallow magma emplacement: application to saucer-shaped intrusions. *Earth Planet. Sci. Lett.* 277, 373–383. doi: 10.1016/j.epsl.2008.11.003

Guldstrand, F., Burchardt, S., Hallot, E., and Galland, O. (2017). Dynamics of surface deformation induced by dikes and cone sheets in a cohesive Coulomb Brittle Crust. *J. Geophys. Res.* 122, 8511–8524. doi: 10.1002/2017JB014346

Hibert, C., Mangeney, A., Polacci, M., Muro, A. D., Vergniolle, S., Ferrazzini, V., et al. (2015). Toward continuous quantification of lava extrusion rate: Results from the multidisciplinary analysis of the 2 January 2010 eruption of Piton de la Fournaise volcano, La Réunion. *J. Geophys. Res.* 120, 3026–3047. doi: 10.1002/2014JB011769

Hollingsworth, J., Leprince, S., Ayoub, F., and Avouac, J. P. (2013). New constraints on dike injection and fault slip during the 1975–1984 Krafla rift crisis, NE Iceland. *J. Geophys. Res.* 118, 3707–3727. doi: 10.1002/jgrb.50223

Lanari, R., Lundgren, P., and Sansosti, E. (1998). Dynamic deformation of Etna volcano observed by satellite radar interferometry. *Geophys. Res. Lett.* 25, 1541–1544. doi: 10.1029/98GL00642

Langmann, B., Folch, A., Hensch, M., and Matthias, V. (2012). Volcanic ash over Europe during the eruption of Eyjafjallajökull on Iceland, April–May 2010. *Atmos. Environ.* 48, 1–8. doi: 10.1016/j.atmosenv.2011.03.054

Lee, S. W., Yun, S. H., Kim, D. H., Lee, D., Lee, Y. J., and Schutz, B. E. (2015). Real-time volcano monitoring using GNSS single-frequency receivers. *J. Geophys. Res.* 120, 8551–8569. doi: 10.1002/2014JB011648

Massonnet, D., Briole, P., and Arnaud, A. (1995). Deflation of Mount Etna monitored by spaceborne radar interferometry. *Nature* 375, 567–570. doi: 10.1038/375567a0

Mathieu, L., de Vries, B. v. W., Holohan, E. P., and Troll, V. R. (2008). Dykes, cups, saucers and sills: analogue experiments on magma intrusion into brittle rocks. *Earth Planet. Sci. Lett.* 271, 1–13. doi: 10.1016/j.epsl.2008.02.020

Merle, O., and Donnadieu, F. (2000). Indentation of volcanic edifices by the ascending magma. *Geol. Soc. Lond. Spec. Publ.* 174, 43–53. doi: 10.1144/GSL.SP.1999.174.01.03

Okada, Y. (1985). Surface deformation due to shear and tensile faults in a half-space. *Bull. Seismol. Soc. Am.* 75, 1135–1154.

Pedersen, R., and Sigmundsson, F. (2006). Temporal development of the 1999 intrusive episode in the Eyjafjallajökull volcano, Iceland, derived from InSAR images. *Bull. Volcanol.* 68, 377–393. doi: 10.1007/s00445-005-0020-y

Peltier, A., Staudacher, T., Catherine, P., Ricard, L.-P., Kowalski, P., and Bachèlery, P. (2006). Subtle precursors of volcanic eruptions at Piton de la Fournaise detected by extensometers. *Geophys. Res. Lett.* 33:L06315. doi: 10.1029/2005GL025495

Poland, M., Miklius, A., Orr, T., Sutton, J., Thornber, C., and Wilson, D. (2008). New episodes of volcanism at Kilauea Volcano, Hawaii. *Eos, Trans. Am. Geophys. Union* 89, 37–38. doi: 10.1029/2008EO050001

Pollard, D. D., and Holzhausen, G. (1979). On the mechanical interaction between a fluid-filled fracture and the earth's surface. *Tectonophysics* 53, 27–57. doi: 10.1016/0040-1951(79)90353-6

Sigmundsson, F., Hooper, A., Hreinsdóttir, S., Vogfjörd, K. S., Ófeigsson, B. G., Heimisson, E. R., et al. (2015). Segmented lateral dyke growth in a rifting event at Bar [eth] arbunga volcanic system, Iceland. *Nature* 517, 191–195. doi: 10.1038/nature14111

Sigmundsson, F., Hreinsdóttir, S., Hooper, A., Arnadóttir, T., Pedersen, R., Roberts, M. J., et al. (2010). Intrusion triggering of the 2010 Eyjafjallajokull explosive eruption. *Nature* 468, 426–430. doi: 10.1038/nature09558

Thun, J., Lokmer, I., Bean, C. J., Eibl, E. P., Bergsson, B. H., and Braiden, A. (2016). Micrometre-scale deformation observations reveal fundamental controls on geological rifting. *Sci. Rep.* 6:36676. doi: 10.1038/srep36676

Toutain, J. P., Bachelery, P., Blum, P. A., Cheminee, J. L., Delorme, H., Fontaine, L., et al. (1992). Real time monitoring of vertical ground deformations during eruptions at Piton de la Fournaise. *Geophys. Res. Lett.* 19, 553–556. doi: 10.1029/91GL00438

Walter, T. R., and Motagh, M. (2014). Deflation and inflation of a large magma body beneath Uturuncu volcano, Bolivia? Insights from InSAR data, surface lineaments and stress modelling. *Geophys. J. Int.* 198, 462–473. doi: 10.1093/gji/ggu080

Wright, T. J., Ebinger, C., Biggs, J., Ayele, A., Yirgu, G., Keir, D., et al. (2006). Magma-maintained rift segmentation at continental rupture in the 2005 Afar dyking episode. *Nature* 442, 291–294. doi: 10.1038/nature04978

Conflict of Interest Statement: The authors declare that the research was conducted in the absence of any commercial or financial relationships that could be construed as a potential conflict of interest.